

Standard Radiation Environment Monitor

- Simulation and Inner Belt Flux Anisotropy Investigation

Martin Siegl

Luleå University of Technology

Master Thesis, Continuation Courses
Space Science and Technology
Department of Space Science, Kiruna

Abstract

The Standard Radiation Environment Monitor (SREM) is a standardised particle detector for mapping highly-energetic protons and electrons of the radiation field. It is employed on several ESA spacecraft (Integral, Rosetta, PROBA-1, Giove-B, Herschel, Planck) to provide radiation level information and to issue dose warnings to other instruments.

A geometric model of the SREM instrument is simulated using GRAS/Geant4 to determine its directional response function. The instrument response to both protons and electrons is obtained for a wide range of discrete energy levels and directions of particle incidence. Analysis of the simulation output shows the directional characteristics of the SREM response and the resulting sensitivity to the pitch angle distribution of the flux. The directional, spherical and integrated response functions of the SREM are presented and discussed.

The SREM on PROBA-1 (Project for On-Board Autonomy) gathers data of geomagnetically trapped protons, particularly in the South Atlantic Anomaly (SAA). The proton flux in the PROBA-1 orbit is investigated using the omnidirectional AP-8 model. Combining the SREM response function with the proton flux yields predictions of the SREM countrates which are then compared to data measured by PROBA-1.

The influence of flux anisotropies on the SREM countrates is demonstrated and proves the necessity of including a model for the distribution of particle pitch angles; the Badhwar-Konradi model of pitch angle distribution is implemented and combined with the omnidirectional AP-8 model to yield an anisotropic unidirectional flux model.

As a consequence, significant improvements to the AP-8 model are realised. The importance of considering flux anisotropies is shown both for short-term SREM countrate features and long-term integrated counts. Data analysis and comparison to simulated data is performed with respect to different values of McIlwain's L-coordinates and varying particle pitch angles. To simulate countrates, the attitude of the SREM on PROBA-1 relative to the magnetic field vector is determined using the magnetometer on-board PROBA-1.

Radiation due to geomagnetically trapped protons contributes substantially to the overall radiation levels on the International Space Station (ISS). Based on the importance of the pitch angle distribution, the relevance of proton anisotropy for ISS dose levels is motivated.

Acknowledgements

The research documented in this thesis report was carried out during a stage (trainee period) at the European Space Research and Technology Centre (ESTEC) of the European Space Agency in Noordwijk, the Netherlands. The stage was made possible by a special agreement between the Directorate of Human Spaceflight and the Erasmus Mundus Joint European Master in Space Science and Technology (SpaceMaster). I am grateful for having been offered the opportunity to work on my thesis in an interesting and stimulating environment like ESTEC. Many people contributed to organising and supervising my stay and to making it the valuable experience it has been.

I would like to express my gratitude to the Directorate of Human Spaceflight for offering me the stage placement. Together with the Space Environments and Effects Section (Directorate of Technical and Quality Management), the Directorate of Human Spaceflight gave me the chance to carry out a thesis in my field of interest of human spaceflight and radiation physics.

I am particularly indebted to Eamonn Daly, head of the Space Environments and Effects Section, for the support he offered me, for providing me with an exciting thesis problem and for supervising my work. Being part of his section for my trainee period has been an enriching experience that I am most thankful for.

Johnny Ejemalm was my supervisor and examiner at the Department of Space Science (IRV) in Kiruna, Sweden. Not only would I like to thank him for guiding me with my thesis, but also for stimulating my interest in the field with his lectures on ‘Spacecraft Environment Interactions’.

In the same way, I would like to thank Christophe Peymirat as the responsible for the Master ‘Techniques Spatiales et Instrumentation’ for his commitment to SpaceMaster and his role as an examiner of my thesis work at Université Paul Sabatier Toulouse III, France.

In the Coordination Office at the Directorate of Human Spaceflight, I would like to express my utmost gratitude to Piero Messina and Olga Zhdanovich for making my trainee period possible. Thanks also to Margaret Hendriks at the Human Resources Department at ESTEC for her assistance.

My very personal thank you goes to Victoria Barabash and Sven Molin, who have been guides and mentors to me all along my studies in the SpaceMaster programme. Victoria

introduced me to SpaceMaster, encouraged my application and was always ready to support me with her most helpful advice, suggestions and guidance. She was also among the people organising my stay at ESTEC. Sven, the visionary of SpaceMaster, is to thank for an outstanding international Master programme that let me experience two years of enriching space excitement and education.

Finally, this work would not have at all been possible without my direct supervisor and office mate in the Space Environments and Effects Section, Hugh Evans. He guided me throughout my trainee period and was an indispensable source of expertise and knowledge to me. Open to all my questions and providing advice all along my project, he helped me avoid pitfalls and led me to produce valuable results. Hugh introduced me to various facets of computational physics and corresponding software tools (ranging from IDL to almost VMS) and motivated me along the steep learning curve of some of them. I am thankful for his support, for the chance to work together with him and to learn from him.

My other colleagues Giovanni Santin, Alessandra Menicucci, Simon Clucas and Petteri Nieminen always had answers to my questions just as the whole Space Environments and Effects Section (Gerhard Drolshagen, John Sorensen, Alexi Glover, David Rodgers, Alain Hilgers and Jean-Paul Huot) made my stay the pleasant experience it has been.

Contents

1	Introduction	10
1.1	The Standard Radiation Environment Monitor (SREM)	11
1.2	SREM Channels	11
1.3	The PROBA-1 Satellite	12
1.3.1	SREM Location and PROBA-1 Coordinate System	13
1.4	Thesis Outline	14
2	The Radiation Belts	16
2.1	Trapped Radiation	16
2.1.1	Inner Van Allen Belt	17
2.1.2	Outer Van Allen Belt	18
2.2	South Atlantic Anomaly (SAA)	18
2.3	McIlwain's (B,L) - Coordinates	18
3	SREM Simulations	20
3.1	Simulation Goals	20
3.2	Geant4, GRAS and the Monte-Carlo Method	21
3.3	Interaction of Protons with Matter (Bethe's Formula)	21
3.4	Silicon PIN-Diode	23
3.5	SREM Geometry	24
3.6	Obtaining a Response Function	26
3.6.1	Instrument Geometry and Detector Mass. Channel Thresholds .	26
3.6.2	Source Definition	28
3.6.3	Source Definition in GRAS	29
3.6.4	Quantitative Treatment and Normalisation	30
3.6.5	Calculating the Response	32
3.6.6	Simulation Error and Statistics	33
3.6.7	Practical Considerations	34
4	Directional SREM Response to Protons and Electrons	36
4.1	Directional Response $R(\theta, \phi, E)$ to Protons	36
4.1.1	Total Channels $TC1$, $TC2$ and $TC3$	37
4.1.2	Channels $S12$ - $S15$	40

4.1.3	Coincidence Channels $C1 - C4$	43
4.1.4	Other Channels ($S25, S32, S33, S34$)	46
4.2	Integrated Response to Protons	48
4.3	Directional Response $R(\theta, \phi, E)$ to Electrons	51
5	Flux Models	52
5.1	AP-8 Omnidirectional Flux	52
5.2	Flux Anisotropies	53
5.2.1	East-West Effect	53
5.2.2	Pitch Angle Distribution	54
5.3	Badhwar-Konradi Pitch Angle Distribution	56
5.3.1	Determining α_L and β	58
5.4	Magnetic Field Models	58
5.4.1	Choice of (B,L)-Coordinates	59
5.5	Practical Considerations and Summary	59
6	Countrate Predictions	60
6.1	General Procedure	60
6.1.1	Choice of Location and Location Coordinates	61
6.1.2	AP-8 Model Evaluation	61
6.1.3	Magnetic Field Evaluation	62
6.1.4	SREM Attitude	62
6.1.5	Directional Flux $F(\theta, \phi, E)$	62
6.1.5.1	SREM Pitch Angle and PROBA-1 Magnetometer	62
6.1.6	Directional Response Function $R(\theta, \phi, E)$	63
6.1.7	Evaluation of Integral and Countrate Calculation	64
6.2	Example Calculation	64
6.3	Implementation	64
6.3.1	IDL Scripts	65
7	Simulation Results	66
7.1	April 19th, 2004: Short Term Observation	66
7.2	Long-Term Integrated Countrates	70
7.2.1	Background Suppression	71
7.2.2	Long-Term Pitch Angle and Flux Distribution	72
7.2.3	Magnetic L-Value Profile	73
8	Human Spaceflight	75
8.1	Overview	75
8.2	Pitch Angle Anisotropies in the ISS Orbit	76

Contents

9 Conclusion	79
9.1 Summary	79
9.2 Conclusions	79
A Badhwar-Konradi Scale Factor	81
A.1 Normalisation	81
B Modifications to Geometric Model	82
B.1 Removing Electronics and Parts of the Structure	82
B.2 Adjusting Cover Plates	82
B.3 Adding Aluminium Shielding	83
B.4 Adjusting the Origin	83
C Details of Source Setup and Normalisation	85
C.1 Directional Derivatives	85
C.2 Flux Normalisation of a Circular Planar Source	86
D IDL Scripts	87
D.1 IDL Script Headers	87
D.2 Data Structures	92
E List of Plotted Figures	
Accessing Response Functions	93
F Paper Accepted for RADECS2009	94

List of Figures

1.1	Picture of SREM flight model (courtesy of ESA)	11
1.2	The PROBA-1 satellite and its orbit on March 31st, 2009	12
1.3	A schematic diagram indicating the orientation of the SREM on PROBA-1	13
1.4	An outline of the work presented in this report	15
2.1	Basic motion of charged particles in the Earth's magnetic field	17
2.2	Integral proton flux ($E > 10\text{MeV}$) in the orbit of PROBA-1 on March 31st, 2009	19
3.1	The total stopping power of aluminium and silicon for protons, as a function of proton energy	22
3.2	The GDML model of the complete SREM instrument	24
3.3	The simulated GDML model of the SREM instrument	25
3.4	SREM detector setup and spherical coordinate system	27
3.5	Dividing a 4π solid angle into 648 elements in steps of $10^\circ \times 10^\circ$	28
3.6	Circular planar source moved around the SREM	29
3.7	Example response plot as used throughout the document	33
4.1	Directional response $R(E, \theta, \phi)$ of channels $TC1$, $TC2$ and $TC3$	37
4.2	Comparison of 4π -averaged response functions of channels $TC1$, $TC2$ and $TC3$ obtained in this work (red, with errorbars) with previous data (black)	38
4.3	Directional response $R(E, \theta, \phi)$ of channels $S12$, $S13$, $S14$ and $S15$	40
4.4	Comparison of 4π -averaged response functions of channels $S12$, $S13$, $S14$ and $S15$ obtained in this work (red, with errorbars) with previous data (black)	41
4.5	Directional response $R(E, \theta, \phi)$ of channels $C1$, $C2$, $C3$ and $C4$	43
4.6	Comparison of 4π -averaged response functions of channels $C1$ - $C4$ obtained in this work (red, with errorbars) with previous data (black)	44
4.7	Directional response $R(E, \theta, \phi)$ of channels $S25$, $S32$, $S33$ and $S34$	46
4.8	Comparison of 4π -averaged response functions of channels $S25$, $S32$, $S33$ and $S34$ for coincidence channels obtained in this work (red, with errorbars) with previous data (black)	47
4.9	Energy-integrated SREM response of channels $C1$ - $C4$	48

List of Figures

4.10	Energy-integrated SREM response of channels $TC1, S13, S14, S15, S25$ and $TC2$.	49
4.11	Directional response $R(E, \theta, \phi)$ of channels $TC3, S32, S33, S34$ to electrons	51
5.1	Proton fluxes in the orbit of PROBA-1 as predicted by the AP-8 MIN and AP-8 MAX models	53
5.2	Illustration of the East-West effect	54
5.3	Normalised distribution of pitch angles for $L = 1.25$ Earth radii and various values of B	55
5.4	The anisotropic scale factor as given by the Badhwar-Konradi model	57
6.1	Block diagram showing the process of obtaining SREM countrate predictions	63
7.1	Pitch-angle dependence of SREM countrates	67
7.2	The anisotropic scale factor as given by the Badhwar-Konradi model for pitch angles of $\approx 84^\circ$ and $\approx 23^\circ$	67
7.3	Angular countrate of channels $TC1, C1$ and $C3$ at pitch angles of $\approx 84^\circ$ and $\approx 23^\circ$	68
7.4	Simulated countrates of SREM channels $S34, TC1, TC2$ under a varying pitch angle	69
7.5	Simulated countrates of SREM channels $C3, C1, C2$ under a varying pitch angle	70
7.6	Histograms of SREM countrates used for determining background levels	71
7.7	Long-term mean of the countrate (channel $C2$) as a function of the SREM pitch angle	72
7.8	Countrate of channel $C2$ compared to AP-8 MAX and AP-8 MAX with a Badhwar-Konradi anisotropic scale factor	73
7.9	Countrate of channel $TC2$ compared to AP-8 MAX and AP-8 MAX with a Badhwar-Konradi anisotropic scale factor	74
8.1	A typical trajectory of the ISS for one day with colour-coded integral proton flux	76
8.2	Flux anisotropy for protons with energy $E > 20\text{ MeV}$ during a one-day ISS orbit	77
8.3	A geometric model of the ISS	78
D.1	Flow chart of the countrate calculation procedure implemented in IDL.	87

List of Tables

3.1	SREM channel thresholds	27
3.2	Example of calculating the directional response function	32
3.3	Example of calculating the error of the directional response function	34
5.1	Coefficients for α_L and β	58
7.1	SREM background levels, in $\frac{\#}{s}$	72
E.1	Selected commands (procedure calls) for reproducing plots	93

List of Abbreviations

CDF	Common Data Format
CRAND	Cosmic Ray Albedo Neutron Decay
ESA	European Space Agency
ESTEC	European Space Research and Technology Centre
GCR	Galactic Cosmic Ray
GDML	Geometric Description Markup Language
GEANT	GEometry ANd Tracking
GEI	Geocentric Equatorial Inertial (coordinate system)
GPS	General Particle Source
GRAS	Geant4 Radiation Analysis for Space
IDL	Interactive Data Language
ISS	International Space Station
LEO	Low Earth Orbit
PROBA	Project for On-Board Autonomy
SAA	South Atlantic Anomaly
SPE	Solar Proton Event
SPENVIS	SPace ENVironment Information System
SREM	Standard Environment Radiation Monitor

1 Introduction

The space environment is one of the most crucial aspects to be taken into consideration during the design of a spacecraft. For a mission to be successful, the effects of radiation, space debris, solar activity and atmospheric interaction have to be assessed carefully through all stages of the design phase and during operation. Wrong predictions of the radiation environment, debris concentration, solar activity, spacecraft charging or atmospheric drag on a spacecraft can lead to severe consequences: in the most favourable case, the mission performance may be reduced, in the worst case there may be the risk of loss of a spacecraft or even of human life (on manned missions).

The space radiation environment has adverse effects on all subsystems of a spacecraft: it leads to material deterioration (e.g. on solar panels), upsets in electrical components, component malfunctions or the loss of components. If experienced by a human being, radiation increases the risk of genetic defects with the potential of leading to cancer. In severe cases (phases of extreme solar activity) radiation sickness or death might occur.

The European Space Agency (ESA) together with its partners Paul Scherrer Institute (PSI) and Contraves Space developed a Standard Radiation Environment Monitor (SREM, [28]). The SREM is an instrument to measure proton and electron radiation levels and is currently part of the spacecraft PROBA-1, Integral, Rosetta, GIOVE-B and the recently launched Herschel and Planck observatories. On-board these satellites, the SREM serves the purpose of issuing warnings if predefined dose thresholds are exceeded. Moreover, the collected data serves as a valuable source for completing and extending our knowledge of the space radiation environment. Since the spacecraft carrying SREM instruments have a wide variety of orbits (PROBA-1 is in a Low Earth Orbit, Herschel and Planck orbit the Lagrange point L2), they allow for intercomparison of different radiation environments.

In Low Earth Orbits (LEO), one of the first ever artificial satellites Explorer-1 in early 1958 was also the first to experience the adverse effects of radiation on spacecraft. It found first evidence of what is now known as the Van Allen radiation belts and the South Atlantic Anomaly (SAA). They are results of the trapping of charged particles in the Earth's magnetic field and are discussed in more detail in Chapter 2.

This work treats aspects of the radiation environment in LEO as encountered by the SREM instrument on-board PROBA-1.



Figure 1.1: Picture of SREM flight model (courtesy of ESA)

1.1 The Standard Radiation Environment Monitor (SREM)

The SREM was developed to equip, at low cost, various different spacecraft with the same radiation detection instrument in order to allow for a standardised comparison between different environments. Three solid state detectors (silicon diodes) measure the energy deposited by charged particles. Figure 1.1 shows the instrument, one box of 2.6 kg and dimensions of $20 \times 12 \times 10\text{ cm}$.

These diodes (D_1 , D_2 , D_3) are arranged as follows: D_3 is a single diode for detection of both protons and electrons. D_1 and D_2 are two single diodes combined together in a telescope configuration. They can therefore be used separately or in a coincidence mode, where a particle is required to deposit energy in both of them simultaneously. D_1 and D_2 are separated by a double layer of aluminium and tantalum with respective thicknesses of 1.7 and 0.7 mm . This defines a proton energy cut-off of $\approx 43\text{ MeV}$ for coincidence detections.

The D_1/D_2 and D_3 main detector entrances have opening angles of 20° and are covered with 2 mm and 0.7 mm of aluminium, respectively, setting an overall detector cut-off energy of $\approx 20\text{ MeV}$ (D_1) and $\approx 10\text{ MeV}$ (D_3) for protons.

1.2 SREM Channels

If a particle is detected by the SREM silicon detectors, i.e. if energy is deposited in one of the diodes D_1 , D_2 , D_3 or in both D_1 and D_2 at the same time, a current is generated and the read-out electronics counts the particle. Depending on the amount of energy deposited and which silicon diode(s) it is deposited in, the detected particle is counted in one of 15 channels.

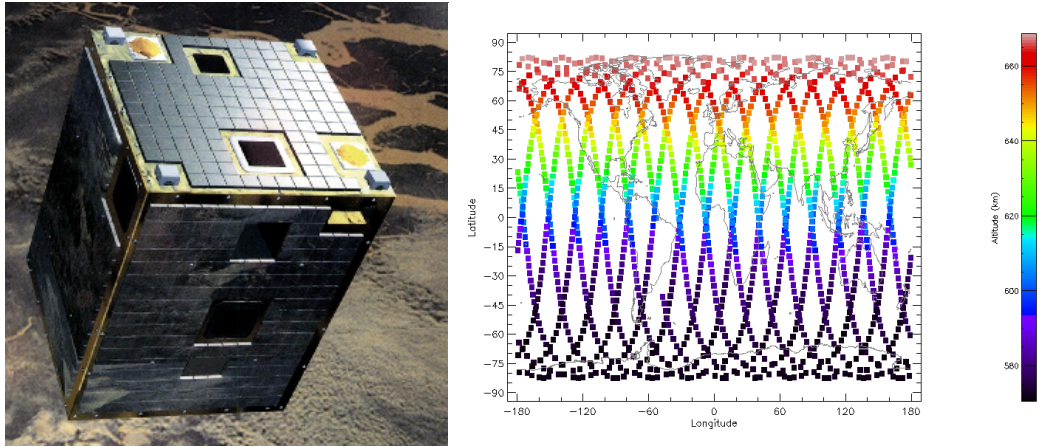


Figure 1.2: The PROBA-1 satellite [15] (artist’s impression, left side) and its orbit on March 31st, 2009 (right side, generated with SPENVIS [4]).

These 15 channels differ in their sensitivity to different particle energies and therefore allow for a certain level of energy resolution and particle species discrimination.

1.3 The PROBA-1 Satellite

The PROBA-1 satellite (Project for On-Board Autonomy, [15]) was launched on October 22nd, 2001 on a Antrix/ISRO PSLV-C3 launcher from Sriharikota in India. The satellite’s main goal is to study various aspects of on-board autonomy such as autonomous error handling.

PROBA-1 (Figure 1.2) is in a sun-synchronous orbit of $\approx 97.9^\circ$ inclination, an apogee of $\approx 661\text{ km}$ and a perigee of $\approx 564\text{ km}$. On March 31st, 2009 the two-line element was

```
PROBA 1
1 26958U 01049B 09090.05950884 -.00000279 00000-0 -21510-4 0 4652
2 26958 97.6303 155.5028 0080295 267.4557 91.7474 14.89645695404193
```

corresponding to an inclination $i = 97.6303^\circ$, an eccentricity $\epsilon = 0.0080295$, a mean motion of 14.896 rev/day , a right ascension of the ascending node of 155.5028° , an argument of perigee of 267.4557° and a mean anomaly of 91.7474° at the time the two-line element was generated (March 31st 2009, 1:15 UT). The time-dependent mean anomaly gives the position of the satellite along its orbital trajectory; since the orbit of PROBA-1 is sun-synchronous, the right ascension of the ascending node and the argument of perigee are also time-dependent and change seasonally.

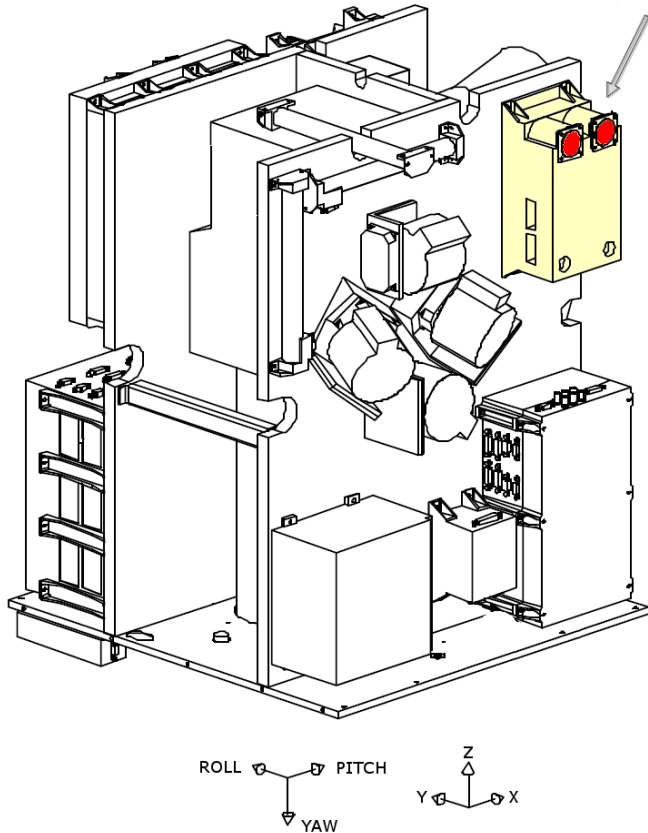


Figure 1.3: A schematic diagram indicating the orientation of the SREM on PROBA-1 and the PROBA-1 Cartesian coordinate system. For this work, a different spherical coordinate system only pertaining to the SREM is used (picture courtesy of ESA and Verhaert Space Systems).

1.3.1 SREM Location and PROBA-1 Coordinate System

Figure 1.3 shows how the SREM is mounted on the PROBA-1 satellite. The bottom of the SREM is fixed to the structure which has a shielding effect for charged particles. The SREM entrance openings (red) are not covered by any part of the satellite structure.

PROBA-1 uses a Cartesian coordinate system with x_{PROBA} corresponding to the satellite's pitch axis, y_{PROBA} to the roll axis and z_{PROBA} to the yaw axis. The velocity vector of PROBA-1 points in the $+y_{PROBA}$ direction. Since this work concentrates on the SREM, a coordinate system that is more natural to the instrument is used, based on

the following conversion:

$$x_{SREM} \rightarrow z_{PROBA}$$

$$y_{SREM} \rightarrow -x_{PROBA}$$

$$z_{SREM} \rightarrow -y_{PROBA}$$

Where convenient, a spherical coordinate system for the SREM is used to specify the directions of incoming particles¹:

$$x_{SREM} = \sin(\theta) \cos(\phi)$$

$$y_{SREM} = \sin(\theta) \sin(\phi)$$

$$z_{SREM} = \cos(\theta)$$

1.4 Thesis Outline

This work treats the SREM on-board the PROBA-1 satellite. The overall goals are to obtain the response function of the instrument for different directions and to compare data from the SREM on PROBA-1 with predictions based on simulation.

In Chapter 2, a brief overview introduces the particle environment that is experienced by PROBA-1 in its orbit. Some basic features of radiation belts around Earth are presented and the equations governing the movement of charged particles in Earth's magnetic field are given.

Key to the treatment of the SREM is knowledge of its response function that describes how counts registered in instrument channels are related to particle fluxes. Chapter 3 details GRAS/Geant4 simulations used to obtain the response function. Selected results are illustrated and discussed in Chapter 4.

The response function needs to be combined with a model for the flux in the PROBA-1 orbit to obtain the expected channel countrates. Chapter 5 therefore introduces the omnidirectional proton flux model AP-8 and enhances it with the Badhwar-Konradi pitch angle distribution.

Meant as a technical outline, Chapter 6 shows how various details (response function, flux models, spacecraft coordinates and attitude) are put together before Chapter 7 presents the results: both short-term and long-term countrate features from the SREM on PROBA-1 are compared and reproduced with simulated data.

¹Since spherical coordinates only pertain to directions in this work, a unit sphere is assumed, i.e. the radius r is set to be the unit distance.

Chapter 8 discusses the relevance of these results for the pursuit of human spaceflight, in particular with regard to dose rates for astronauts on the International Space Station (ISS) which traverses through a radiation environment similar in characteristic to that of PROBA-1.

Figure 1.4 summarises the outline of this work and explains how various aspects need to be combined.

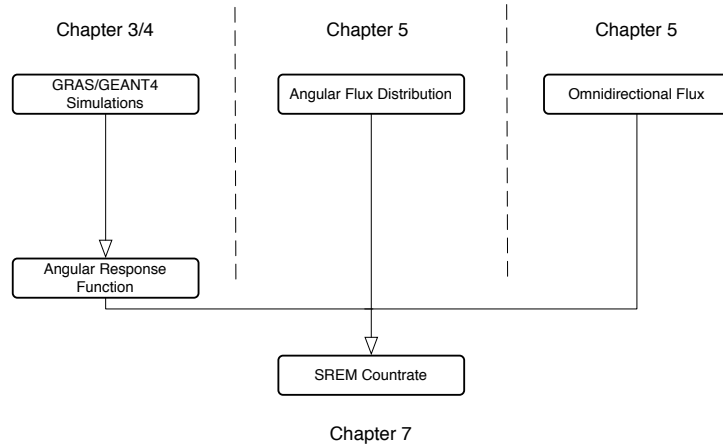


Figure 1.4: An outline of the work presented in this thesis. The main emphasis is on GRAS/Geant4 simulations for obtaining an angular response function and on predicting the SREM countrate by combining the response function with models for the particle flux.

2 The Radiation Belts

2.1 Trapped Radiation

The movement of a charged particle is fundamentally governed by the Lorentz force, $\vec{F} = q(\vec{E} + \vec{v} \times \vec{B})$, where q is the particle charge, \vec{v} the particle's velocity vector and \vec{E} and \vec{B} the electric and magnetic field vector, respectively. For charged particles in the magnetic field of Earth, a term representing gravitation may be added to extend the equation:

$$m \frac{d^2\vec{r}}{dt^2} = q(\vec{E} + \vec{v} \times \vec{B}) + m\vec{g} \quad (2.1)$$

The Lorentz force is responsible for particles gyrating (i.e. circling) around magnetic field lines. Combined with particle motion along (in parallel to) the magnetic field line, this leads to an overall motion of spiralling along the magnetic field line.

While the Lorentz force is sufficient to explain particle motion in a homogeneous magnetic field, the motion in Earth's inhomogeneous dipole magnetic field requires that additional aspects be considered:

In a slowly-varying¹ magnetic field, the magnetic moment μ of a particle's gyration is adiabatically constant. The constant μ is proportional to the gyration radius r_g and the velocity component perpendicular to the magnetic field line, v_\perp :

$$\mu \propto v_\perp r_g \quad (2.2)$$

As the field strength rises in an inhomogeneous magnetic field, r_g becomes smaller and v_\perp increases. Since the overall kinetic energy of the particle is constant too,

$$\frac{m}{2} (v_\perp^2 + v_\parallel^2) = \text{const.} \quad (2.3)$$

an increase of v_\perp is at the expense of v_\parallel . The point where $v_\parallel = 0$ is called the 'mirror point'. The gyrating particle changes direction at this point and spirals back along the magnetic field line until it reaches the conjugate mirror point. In effect, this leads to

¹A magnetic field is 'slowly-varying' if the variation is negligible on the scale of the gyration radius.

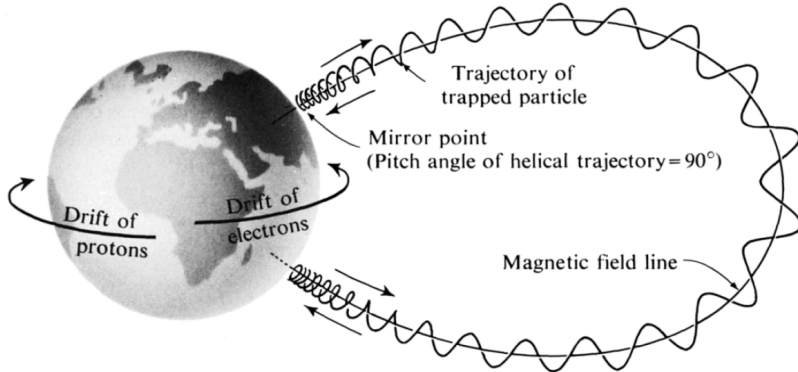


Figure 2.1: Basic motion of charged particles in the Earth’s magnetic field. Picture taken from Hess [20]. The gyro-, drift- and bounce-motions are illustrated.

a bouncing motion between the two conjugate mirror points, essentially ‘trapping’ the particle on a specific field line. Particle radiation that is due to particles confined in the Earth’s magnetosphere is called trapped radiation. The pitch angle α is the angle between the velocity vector \vec{v} and the magnetic field vector \vec{B} . At the mirror points, $\alpha = 90^\circ$, i.e. the velocity vector \vec{v} and the magnetic field vector \vec{B} are perpendicular to each other.

Aside from the gyro-motion along a magnetic field line and the bounce motion between two conjugate mirror points, a charged particle in the Earth’s magnetic field exhibits a drift motion to the East or West, depending on particle charge. Figure 2.1 summarises all three aspects of particle motion.

2.1.1 Inner Van Allen Belt

The inner Van Allen belt is a radiation belt of protons in the energy range from 0.1 MeV up to several 100 MeV . The assumed origin of these protons is mainly the β -decay of free neutrons produced when Galactic Cosmic Rays (GCRs) interact with molecules of the Earth’s atmosphere (Hess [20]). The process is denoted Cosmic Ray Albedo Neutron Decay (CRAND).

Protons from the inner Van Allen belt are virtually lost only through absorption in the Earth’s atmosphere. This occurs if a particle’s mirror point is at too low an altitude, i.e. the particle’s pitch angle does not reach $\alpha = 90^\circ$ before atmospheric absorption occurs. Particles getting absorbed due to a low mirror point altitude are usually identified by their pitch angle at the equator (equatorial pitch angle, α_E). Their equatorial pitch

angles are smaller than α_L , the so-called loss cone angle ($\alpha_E < \alpha_L$). The particles are then said to be ‘in the loss cone’.

2.1.2 Outer Van Allen Belt

The outer Van Allen Belt consists mainly of highly energetic electrons injected from the geomagnetic tail during ‘storms’ and accelerated through wave-particle interactions. It overlaps with the orbit of PROBA-1 only in the region of the polar horns ($L > 4.5^2$) and is therefore not a subject of this work.

2.2 South Atlantic Anomaly (SAA)

The axis of the Earth’s magnetic field is tilted by $\approx 11^\circ$ with respect to the Earth’s rotational axis. As a consequence, the inner Van Allen belt is closer to the Earth’s surface above Brazil and the South Atlantic than anywhere else. For the altitude range of $\approx 200 - 300\text{ km}$, the highest particle flux will be encountered in this geographic region, a phenomenon called South Atlantic Anomaly (SAA).

Practically all contributions to the proton radiation for PROBA-1 stem from the satellite passing the SAA, as Figure 2.2 indicates. Contributions from Solar Proton Events (SPE) at high latitudes are taken out of the dataset processed in this work.

2.3 McIlwain’s (B,L) - Coordinates

For defining locations in the magnetosphere, a geographical coordinate system is unintuitive. Due to the dislocation of the magnetic field with respect to Earth’s rotational axis, the magnetic field configuration at for example a longitude of -50° and latitude of -30° (location of the SAA) differs vastly from the magnetic field at the corresponding geographical location on the Northern hemisphere. Geomagnetic coordinates such as McIlwain’s (B,L)-coordinates are therefore used instead of geographical coordinates. (B,L)-coordinates make use of the symmetry inherent to a dipole magnetic field.

The L coordinates refer to so-called L-shells. An L-shell is mapped out by a particle’s mirroring and drift motions (Eastwards or Westwards) around the Earth and is therefore also called a drift-shell. By definition, a particle stays on the same L-shell (i.e. has the same L-coordinate) during the complete time of its trapping in the magnetosphere. In a pure dipole magnetic field, a group of magnetic field lines belongs to an L-shell. These

²McIlwain’s (B,L)-coordinates are treated in Section 2.3

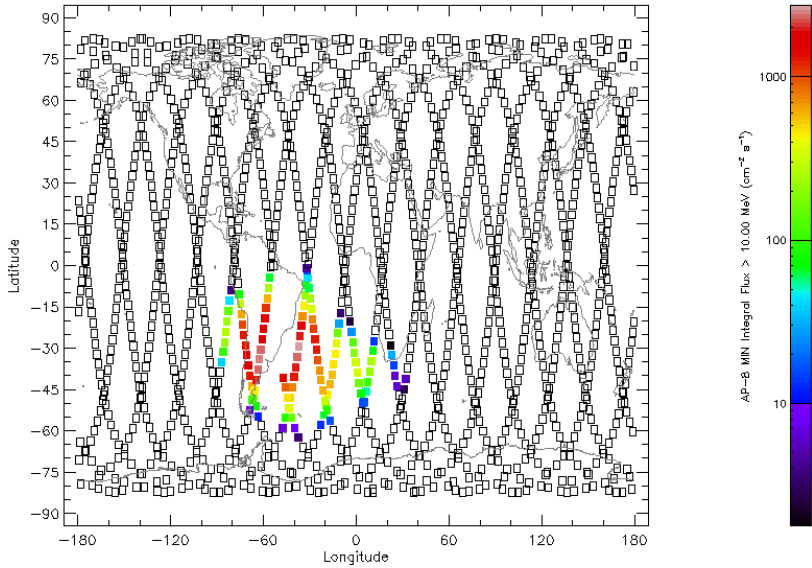


Figure 2.2: Integral proton flux ($E > 10\text{MeV}$) in the orbit of PROBA-1 on March 31st, 2009 as predicted by SPENVIS using the AP-8 MIN model.

magnetic field lines cross the geomagnetic equator at a distance R from the geomagnetic axis. An L-shell is identified using the distance R , i.e. the L-coordinates are given in units of Earth radii. In practice, for a magnetic field that is not a pure dipole, the L coordinates do not exactly match with the distance at which the equator is crossed but L is still the label used for a field line or drift shell.

The B coordinates give the magnetic field strength in gauss (G) at a certain location. For a given L-shell, the magnetic field a particle is subject too is stronger towards the poles than at the equator. The B-coordinates (the magnetic field strength) can therefore be used as a measure of latitude of a specific location on an L-shell.

3 SREM Simulations

3.1 Simulation Goals

Data from the SREM instrument on-board PROBA-1 is in the raw format of counts per time unit. For every sampling interval (which is usually 30 s), the number of counts in every instrument channel is obtained. The scientific goal is to obtain quantitative results about the particle flux that led to this countrate. Both its energy distribution and angular distribution are of interest.

The countrate C is related to the environmental flux $F(\theta, \phi, E)$ through the instrument response function $R(\theta, \phi, E)$ ¹.

$$C = \int_0^\infty \int_0^{2\pi} \int_0^\pi F(\theta, \phi, E) R(\theta, \phi, E) \sin(\theta) d\theta d\phi dE \quad (3.1)$$

For the SREM instrument, the response function has been determined as a function of energy $R(E)$ by Bühler et al. [8]. This thesis extends the response function to include angular resolution $R(\theta, \phi, E)$. The Monte-Carlo simulation tools GRAS/Geant4 are employed for this purpose. In principle, the angular response function could also be determined experimentally, e.g. by moving an ideal (known) proton source around the instrument and recording the instrument response. Simulation and experiment complement each other in the sense that simulations are easier to work with, more flexible and more economic. However, their validity has to be verified in an experiment.

The goals for the Monte-Carlo simulation are as follows:

- Find the response function $R(\theta, \phi, E)$ of the SREM instrument to proton and electron radiation on an applicable energy interval.
- Average the detector response $R(\theta, \phi, E)$ over the whole sphere to regenerate $R(E)$ and compare the value to the work performed by Bühler et al. [8].
- Based on this comparison, discuss the validity and scope of the obtained results.

¹The response function R includes the geometric factor G of the instrument aperture.

3.2 Geant4, GRAS and the Monte-Carlo Method

Complex problems in physics can usually not be solved in a closed, deterministic way. For example, the question "What is the probability of a proton with a given energy incident from a certain direction to be detected by the SREM?" cannot be answered directly. The interactions of a detection instrument with a proton are too complex to be treated in a closed mathematical expression in their entirety. Furthermore, some of the underlying physical processes are inherently non-deterministic. Computational simulation is therefore used to answer questions such as the above.

Simulations in the field of particle physics usually make use of the Monte-Carlo method. In a Monte-Carlo simulation, a set of primary particles is created and each of them is then ‘flown’, i.e. simulated. The interactions of the particle with surrounding matter are calculated step wise until the particle has deposited all of its energy or left the simulation space. In each step, the calculation is carried out according to well-established interaction ‘cross sections’, based on experimental data or theory. Provided that the number of primary particles was sufficient, a statistically reliable answer to the original question may be obtained.

This work uses Geant4 (Agostinelli et al. [1]) and GRAS (Santin et al. [32]) to perform Monte-Carlo simulations of the SREM. Originally, Geant4 and its predecessor GEANT3 were created by CERN for use with particle accelerators. GRAS is an application that simplifies the use of Geant4 by providing an extensive set of commands as an interface to the underlying Geant4 library, tailored for users in space research and engineering.

Usually it is estimated that Monte-Carlo simulations in particle physics are accurate within $\pm 10\%$ for any given observed value.

3.3 Interaction of Protons with Matter (Bethe’s Formula)

Protons passing through a solid body (e.g. a detector or its shielding) lose energy mainly due to excitation and ionisation of atoms. Both these physical processes, excitation and ionisation, are fundamentally governed by Coulomb interaction. The interaction cross-section for the processes is generally determined by the characteristics of the solid and the energy of the incoming proton.

Over a wide range of energies (starting from $\approx 2 \text{ MeV}$ upwards), the energy loss a proton encounters in a solid is best modelled by Bethe’s formula (or Bethe-Bloch formula). It describes the energy loss $-\frac{dE}{dx}$ that a heavy charged particle is subject to as it interacts with solid matter. The relationship, as implemented in the Geant4 electromagnetics module (CERN [11]) is:

3 SREM Simulations

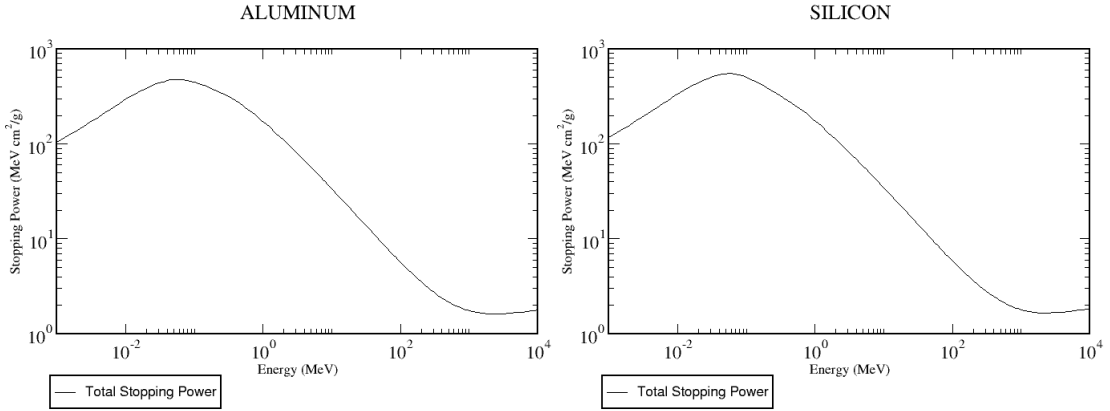


Figure 3.1: The total stopping power of aluminium (left) and silicon (right) for protons, as a function of proton energy. The total stopping power is described by Bethe's formula. The graphs were generated based on data by Berger [5] using the web-based PSTAR database provided by NIST - National Institute of Standards and Technology [29].

$$-\frac{dE}{dx} = 2\pi r_e^2 mc^2 n_{el} \frac{z^2}{\beta^2} \left[\ln \left(\frac{2mc^2 \beta^2 \gamma^2 T_{up}}{I^2} \right) - \beta^2 \left(1 + \frac{T_{up}}{T_{max}} \right) - \delta - \frac{2C_e}{Z} + F \right] \quad (3.2)$$

with

r_e	electron radius (classical)
m	electron (rest) mass
I	mean excitation energy of material
Z	atomic number of material
β^2	$1 - \left(\frac{1}{\gamma^2} \right)$
T_{up}	$\min(T_{cut}, T_{max})$
C_e	shell correction function
F	higher order corrections
z	charge of incident particle
γ	E/mc^2
δ	density effect function

A plot of this relationship for different values of energy E and different materials is shown in Figure 3.1. For this work, the values for $-\frac{dE}{dx}$ in aluminium (parts of SREM structure) and silicon (SREM sensitive detector material) are of special interest. The SREM encounters protons in the energy range 1 MeV-500 MeV. It can be seen clearly

that in this energy range, particle energy and deposited energy are inversely proportional. This means the higher the energy of an incident particle, the lower the energy loss in the detector mass. In fact, protons will encounter their biggest energy loss just before they are stopped completely, leading to a feature called the Bragg peak.

According to CERN [11], ‘the precision of Bethe-Bloch formula for $T > 10 \text{ MeV}$ is within 2%, below the precision degrades and at 1 keV only 20% may be guaranteed’.

Therefore, for ‘low energies’, in practice for $E < \approx 2 \text{ MeV}$, Geant4 uses proton parametrisation to predict energy loss.

In case of ‘high energies’, a speciality of Geant4 is the ‘range cut’. It determines at what energies secondary particles due to ionisation should explicitly be created (‘flown’) instead of only considering them as an energy loss to the primary particle.

The theory presented above is included in different ‘physics lists’ provided by Geant4.

For the proton simulations in this work, the physics list QGSP_BIC recommended for space physics simulations is used. QGSP_BIC includes provisions for simulating nuclear (hadronic) interactions².

3.4 Silicon PIN-Diode

The sensitive detector elements in the SREM are ORTEC (type Ultra) passivated ion-implanted silicon diodes. Each diode represents one of the three detecting elements ($D1$, $D2$, $D3$). The capability of these diode to detect charged particles shall be discussed using the example of the related PIN-diode.

PIN-diodes belong to the class of semiconductor solid-state detectors. Like conventional PN-diodes, they consist of a p-layer and a n-layer: The p-layer is a layer of silicon doped with a trivalent chemical element, the n-layer is a layer of silicon doped with a pentavalent chemical element. Due to the doping, the n-layer carries excess electrons (negative charge-carriers) and the p-layer excess holes (positive charge-carriers).

If the p-layer and the n-layer are pressed together, a charge-carrier free depletion region forms. This depletion region can be used for particle detection purposes. Charged particles such as protons can ionise the atoms in the depletion region, forming one or several electron-hole charge-carrier pairs. The electron-hole pairs then generate an electrical pulse in the diode that can be recorded by read-out electronics.

²Apart from the processes mentioned in this section (usually referred to as ‘electromagnetic’ in high energy physics), protons can also undergo nuclear interactions with the nuclei of the material they are passing. This results in production of collision products of various kinds that have to be tracked but often deposit most of their energy close to the collision site.

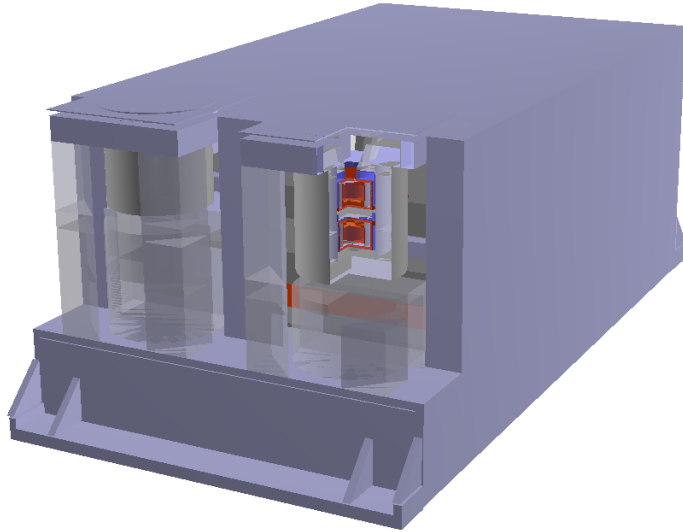


Figure 3.2: The GDML model of the complete SREM instrument, visualised in ROOT. A box cut has been applied to the coincidence detector assembly to show the detector arrangement.

In conventional PN-diodes, the depletion region can reach a thickness of $1 - 2\text{ mm}$ (Knoll [24]). For particle detection purposes, a bigger depletion layer is favourable to increase detector cross-section. Therefore, PIN-diodes are used for radiation detection purposes: between the p- and n-layers, an ‘intrinsic’ layer increases the volume of the depletion region (hence the name PIN, for the p-, i- and n-layers). Undoped (and specially purified) silicon makes up the i-layer.

The number of electron-hole pairs and therefore the amplitude of the resulting pulse depends on the energy of the incident particle³. A higher energy particle will lead to the generation of fewer electron-hole pairs per unit distance, as described by the Bethe’s formula.

3.5 SREM Geometry

The geometry of the SREM was made available by ESA TEC-EES in Geometric Description Markup Language (GDML). GDML is a markup language specifically designed for

³The shape and amplitude of the pulse is also influenced by the reverse bias voltage applied to the diode, to be determined by the instrument designer.

3 SREM Simulations

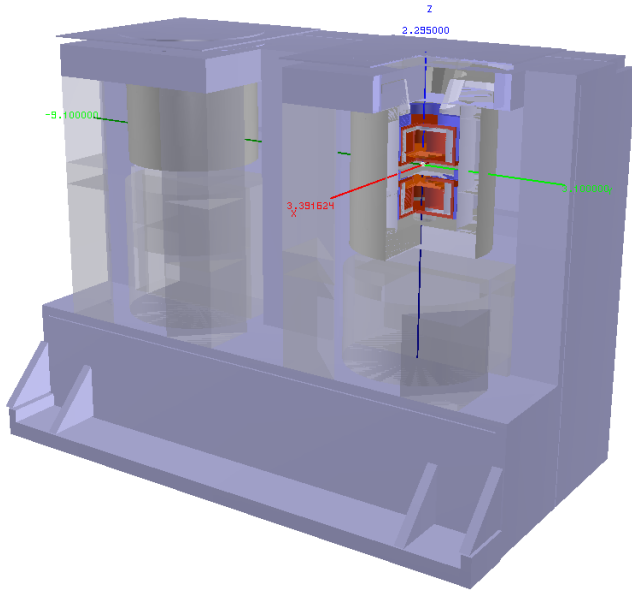


Figure 3.3: The simulated GDML model of the SREM instrument. The electronics part of the instrument has been replaced with an aluminium shield. A box cut has been applied to the coincidence detector assembly to show the detector arrangement.

implementing Geant4 geometries (Chytracek et al. [12], CERN [10]) and can be both imported and exported from within Geant4. GDML geometries are conveniently visualised using the ROOT data analysis framework (The ROOT Team [34]). This method is used throughout this work. The complete instrument can be seen in Figure 3.2.

A complete instrument simulation would require a spherical source around the whole instrument. In order to achieve a reasonable current through the actual sensitive detector elements, a vast number of primary events ($\approx 10^8$) would have to be generated, leading to long simulation times. For this work, it has been decided to run simulations with the actual detector part of SREM (shown in Figure 3.3) and to model the rest of the instrument with a 1 cm aluminium shield.

For this purpose, the original GDML geometry is edited and adjusted manually. The applied changes consist of

- removing parts of the instrument,
- resizing the housing of the instrument correspondingly,
- implementing an aluminium shield and
- adjusting the coordinate origin.

These adjustments in GDML code are documented in Appendix B.

3.6 Obtaining a Response Function

This section shall discuss how to use particle simulation to obtain an instrument response function. Qualitatively, the process of obtaining the instrument response consists of several steps:

1. Definition of instrument geometry and detector mass (Section 3.6.1). In this work, the detectors (silicon diodes) are included in the provided SREM instrument geometry. The sensitive detector volumes have to be defined and energy thresholds for the SREM channels have to be set. An appropriate coordinate system has to be introduced based on the location of the detector mass.
2. Definition of a particle source (Sections 3.6.2 and 3.6.3). The number and type of particles, their energies, their starting locations and flying directions have to be set.
3. After the simulation, normalisation has to be applied to the results to get a response function in the proper units, i.e. [cm^2], that can be used conveniently for further work (Section 3.6.4).

The response function can be seen as the ‘answer’ of the instrument to incident radiation. As discussed below, the response function will have units of [cm^2], corresponding to a cross-section.

3.6.1 Instrument Geometry and Detector Mass. Channel Thresholds

The adapted SREM geometry contains all parts of the instrument and can be used directly in GRAS/Geant4 for simulation purposes. However, the parts (physical volumes) containing the actual sensitive mass (where the energy deposition of incoming particles should be recorded) have to be defined. As outlined before, the sensitive physical volumes correspond to the ‘intrinsic’ layers of the three PIN-diodes in the SREM⁴.

Directly related to this, the energy thresholds for the 15 SREM channels (Table 3.1) have to be considered when processing the simulation results. For example, a particle depositing 0.7 MeV in detector $D1$ without depositing energy in $D2$ or $D3$ will be counted in channels $TC1$, $S12$ and $S13$.

A coordinate system has to be defined for the simulation. The origin is set to be between the detector masses $D1$ and $D2$ and the spherical coordinate directions are fixed as outlined in Figure 3.4.

⁴In the GDML geometry file, the sensitive physical volumes are identified as **SIL1** **SIL2** **SIL3** for $D1$, $D2$ and $D3$ respectively

3 SREM Simulations

Table 3.1: SREM channel thresholds, from Vuilleumeir [36] (discrimination levels) and Bühler [7] (minimum and maximum proton energies).

Counter	Detector	Energy deposition discrimination levels [MeV]	Proton energy[MeV]	
			Min	Max
TC1	D_1	$0.085 - \infty$	26	∞
S12	D_1	$0.25 - \infty$	26	∞
S13	D_1	$0.6 - \infty$	26	∞
S14	D_1	$2.0 - \infty$	24	566
S15	D_1	$3.0 - \infty$	22	646
TC2	D_2	$0.085 - \infty$	49	∞
S25	D_2	$9.0 - \infty$	53	318
C1	$D_1 \& D_2$	$0.6 - \infty \& 2.0 - \infty$	42	114
C2	$D_1 \& D_2$	$0.6 - \infty \& 1.1 - 2.0$	52	278
C3	$D_1 \& D_2$	$0.6 - \infty \& 0.6 - 1.1$	76	450
C4	$D_1 \& D_2$	$0.085 - 0.6 \& 0.085 - 0.6$	164	∞
TC3	D_3	$0.085 - \infty$	12	∞
S32	D_3	$0.25 - \infty$	12	∞
S33	D_3	$0.75 - \infty$	12	∞
S34	D_3	$2.0 - \infty$	12	∞

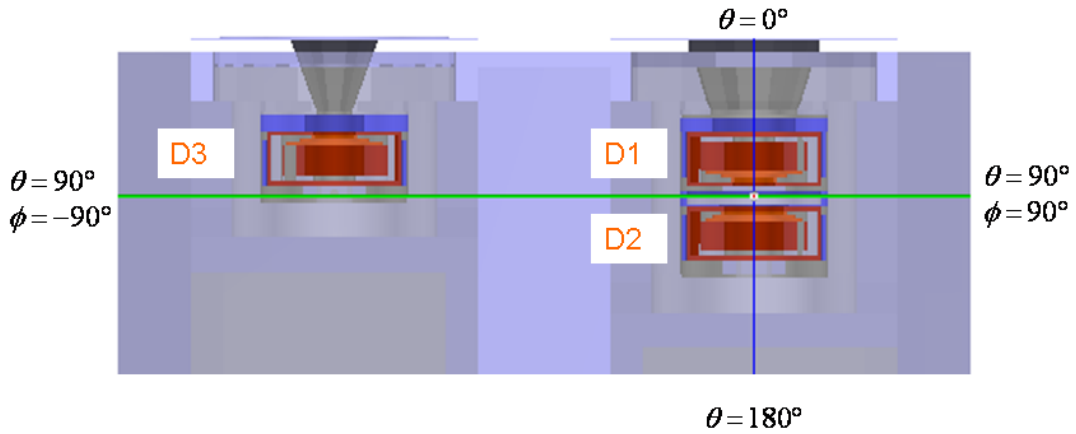


Figure 3.4: SREM detector setup and spherical coordinate system with azimuth angle ϕ and elevation angle θ . The origin is located between silicon diodes D_1 and D_2 .

A particle entering the detector through the main entrance has elevation angle $\theta = 0^\circ$ and a particle horizontally entering the detector from the side has $\theta = 90^\circ$.

3.6.2 Source Definition

Simulating the response of the SREM requires the definition of the particles that are to be ‘flown’ in the simulation: the particle type(s), energies, starting point(s) and starting direction(s).

The response function is obtained independently for protons and electrons. In the case of protons, the range of simulated discrete energies is $10\text{ MeV} - 500\text{ MeV}$, the lower limit being set by the detection threshold of the SREM and the upper limit being set by the energy of typical GCRs. For electrons, discrete energies in the range from 0.7 MeV to 10 MeV are used.

The definition of the particles’ starting points and their starting directions set the ‘geometry’ of the source. Since the SREM response is to be obtained with angular resolution, i.e. since the response shall be determined individually for different directions, a different source has to be specified for each of these directions. The 4π solid angle around the instrument is split in steps of $10^\circ \times 10^\circ$, resulting in $\frac{360}{10} \cdot \frac{180}{10} = 648$ simulated directions (Figure 3.5). A planar circle is set up as a source for each of these 648 directions. The planar source centres are given by $\theta = (10i + 5)^\circ$ and $\phi = (10j + 5)^\circ$, with $i = 0, \dots, 17$ and $j = -18, \dots, 17$.

Figure 3.6 shows the source location and the simulated particle trajectories for directions of $\theta = 45^\circ$ and $\phi = 45^\circ$ (left) and $\theta = 45^\circ$ and $\phi = 135^\circ$ (right).

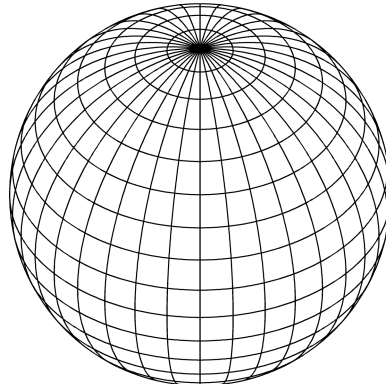


Figure 3.5: Dividing a 4π solid angle into 648 elements in steps of $10^\circ \times 10^\circ$. Towards the poles of the sphere (elevation $\theta = 0^\circ$ and 180°), the resulting solid angles are smaller. This has to be taken into account for normalisation.

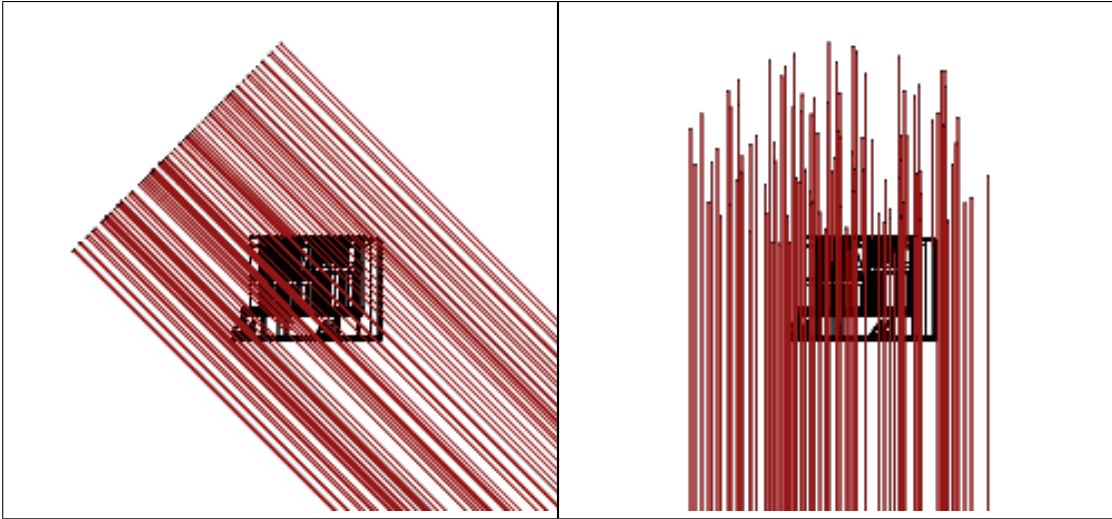


Figure 3.6: Circular planar source for $\theta = 45^\circ$ and $\phi = -45^\circ$ (left panel) and $\theta = 45^\circ$ and $\phi = -135^\circ$ (right panel). The figures illustrate how the circular planar source is moved around the SREM. They are generated in HepRApp (Perl [31]), using a parallel projection of a wireframe model of the SREM. The viewing angle is the same for both figures, i.e. the SREM is seen from the same direction of $\theta = 90^\circ$ and $\phi = 45^\circ$. In the left panel, the source is therefore seen from the side, in the right panel from the opposite azimuth direction.

To ensure that the particle beam from the source covers the instrument from all possible directions, a radius of $r \geq 14\text{ cm}$ is required for the circular source plane.

Defining a circular planar source for each of the 648 directions ensures that if all 648 circular planes are combined together, the result is a spherical omnidirectional source around the SREM.

3.6.3 Source Definition in GRAS

Geant4 and GRAS provide a module called the General Particle Source (GPS) that is used to specify the particle beam. Details of source setup used in this work are given in Appendix C. Here, the case of a circular planar source with $\theta = 45^\circ$ and $\phi = 45^\circ$ (as shown in Figure 3.6) shall be given as a particular example.

```
/gps/particle proton
/gps/ene/type Mono
/gps/ene/mono 100 MeV
```

```
/gps/pos/type Plane
/gps/pos/shape Circle
/gps/pos/radius 14.0 cm
/gps/pos/centre 7.0 7.0 9.89 cm
/gps/pos/rot1 0.5 0.5 -0.71
/gps/pos/rot2 -0.71 0.71 0
/gps/direction -7.0 -7.0 -9.89 cm
/gps/ang/type planar
```

The lines above define a proton source, monoenergetic with 100 MeV. The protons are generated from a circular plane of radius $r = 14\text{ cm}$.

The centre of the circular plane lies at $\vec{c} = \begin{pmatrix} 7 & 7 & 9.98 \end{pmatrix} \text{ cm}$ (this is the position vector for a point at 14 cm distance in direction $\theta = 45^\circ$ and $\phi = 45^\circ$, expressed in Cartesian coordinates). The circular plane needs to be perpendicular to the position vector of the circle centre and therefore needs to be rotated accordingly. This is achieved with GPS by defining two direction vectors $\vec{rot1}$ and $\vec{rot2}$ lying in the plane and thereby defining the plane's attitude. Their general form (use of directional derivative) is given in Appendix C.

Finally, the direction that the protons are to be flown in is defined as $\vec{d} = -\vec{c}$ (the position vector of the circle centre, inverted) and the protons are confined to start from the circular plane in a planar way, i.e. perpendicular to the plane.

3.6.4 Quantitative Treatment and Normalisation

Starting from

$$C = \int_0^\infty \int_0^{2\pi} \int_0^\pi F(\theta, \phi, E) R(\theta, \phi, E) \sin(\theta) d\theta d\phi dE \quad (3.3)$$

an expression for the detector response $R(\theta, \phi, E)$ needs to be obtained. From the GRAS simulation, the value of C (number of counts in the simulated detector) for a certain number of simulated primary particles N is known. The equation (3.3) has to be simplified, rearranged and solved to give an expression for R . The flux $F(\theta, \phi, E)$ has to be derived from the number of primary particles N through normalisation.

The dimensions of the terms in the integrand of (3.3) are

$$F \left[\frac{\#}{\text{cm}^2 \text{sr MeV s}} \right]$$

and

$$R \left[cm^2 \right].$$

F is defined as unidirectional flux, differential in energy. After integration, C therefore assumes the units of $\left[\frac{\#}{s} \right]$, as expected.

In order to solve for R , E is taken as constant (monoenergetic simulation), omitting the integration over energy:

$$C(E) = \int_0^{2\pi} \int_0^\pi F(\theta, \phi, E) R(\theta, \phi, E) \sin(\theta) d\theta d\phi \quad (3.4)$$

In the GRAS simulation, the solid angle sphere is divided into 648 discrete elements by lines of longitude and latitude like on a globe. The integration of the response function over the sphere therefore has to be replaced by an integration over each element s_i followed by a summation over all the 648 elements:

$$C = \sum_{i=1}^{648} \iint_{s_i} F_i R_i \sin(\theta) d\theta d\phi = \sum_{i=1}^{648} F_i R_i \iint_{s_i} \sin(\theta) d\theta d\phi = \sum_{i=0}^{648} F_i R_i \delta s_i \quad (3.5)$$

where \iint_{s_i} is the integration over the surface of the i -th solid angle element. Looking at one element i , the equation reads

$$C_i = F_i R_i \delta s_i \quad (3.6)$$

and R_i therefore is

$$R_i = \frac{C_i}{F_i \delta s_i} \left[cm^2 \right]. \quad (3.7)$$

The flux F_i corresponding to the number of simulated primary events N_i can be calculated through normalisation as follows:

$$F_i = N_i \frac{1}{\pi r^2} \frac{1}{\delta s_i} \left[\frac{\#}{cm^2 sr s MeV} \right] \quad (3.8)$$

In this equation, r is the radius of the simulated circular planar source ($r = 14\text{ cm}$). The normalisation underlying this equation that allows to express a number of primary particles as a flux is derived in Appendix C.

Replacing the flux F_i in (3.7) with the relationship obtained in (3.8), the response function R_i finally becomes

Table 3.2: Example of calculating the directional response function of channel *TC1* for 100 *MeV* protons.

θ [deg]	ϕ [deg]	C_i [#]	N_i [#]	δs_i [sr]	R_i [cm^2]	$R_i \delta s_i$ [$cm^2 sr$]
5	5	1107	10^6	0.0026515	0.6816	0.00180736
15	5	1062	10^6	0.0078740	0.6539	0.00514903
25	5	692	10^6	0.0128574	0.4261	0.00547854
\vdots	\vdots	\vdots	\vdots	\vdots	\vdots	\vdots
85	5	135	10^6	0.030307	0.8312	0.00251931
95	5	150	10^6	0.030307	0.9236	0.00279924
\vdots	\vdots	\vdots	\vdots	\vdots	\vdots	\vdots
155	5	2	10^6	0.0128574	0.0012	0.00001583
165	5	3	10^6	0.0078740	0.0018	0.00001455
175	5	15	10^6	0.0026515	0.0092	0.00002449
$\frac{1}{4\pi} \sum_{i=1}^{648} R_i \delta s_i = 0.0814704$						

$$R_i = \frac{r^2 \pi C_i}{N_i} \left[cm^2 \right] \quad (3.9)$$

Therefore, to obtain the response function R_i for a specific direction, the ratio of detected particles and primary particles $\frac{C_i}{N_i}$ has to be multiplied by $r^2 \pi$. In this work, r is set to 14 cm , therefore $r^2 \pi \approx 615.8$.

Previous work of Bühler et al. [8] has shown a 4π -averaged spherical response function, without angular resolution. For comparison purposes, this spherical response function $R_{4\pi}$ can be regenerated from a complete set of angular response functions R_i by

$$R_{4\pi} = \frac{1}{4\pi} \sum_{i=1}^{648} \iint_{s_i} R \sin(\theta) d\theta d\phi = \frac{1}{4\pi} \sum_{i=1}^{648} R_i \delta s_i = \frac{r^2}{4} \sum_{i=1}^{648} \frac{C_i}{N_i} \delta s_i \left[cm^2 \right] \quad (3.10)$$

Note that the response function $R_{4\pi}$ also has the same unit as a cross-section.

3.6.5 Calculating the Response

To illustrate the application of the formulas given above, the response of channel *TC1* to protons of energy 100 *MeV* from various directions shall be calculated.

The calculated R_i can be used to visualise the detector response in plots such as in Figure 3.7. The values calculated in Table 3.2 above are highlighted (bright strip) in

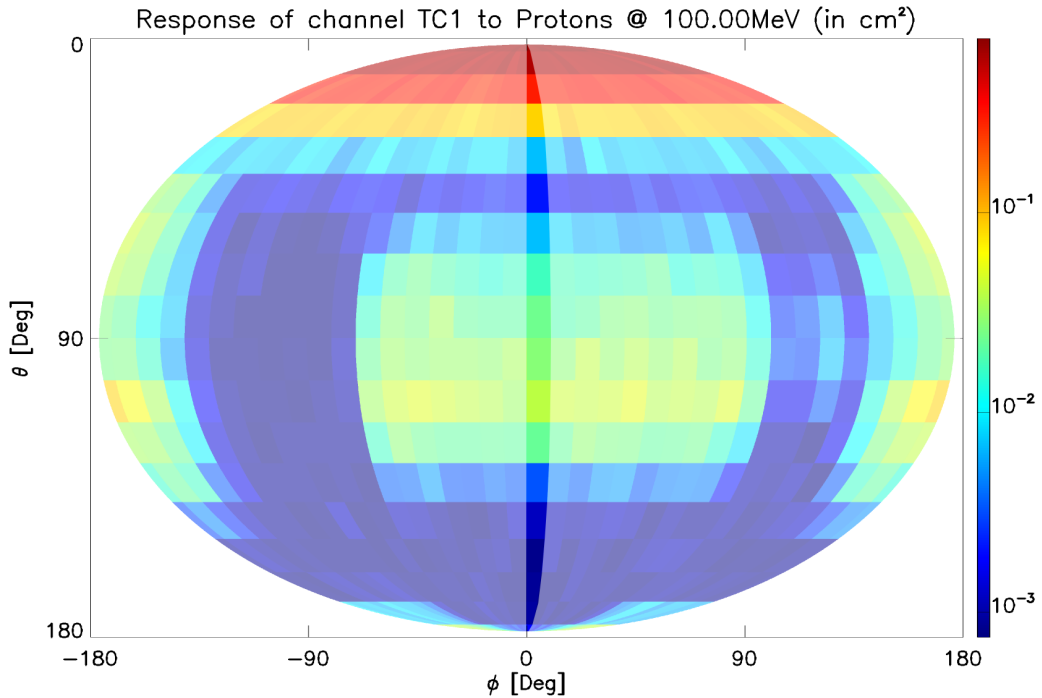


Figure 3.7: Example response plot as used throughout the document, made from values R_i calculated in Table 3.2. The values calculated in the table are shown in the bright strip. Response plots use the Mollweide projection to display the whole sphere around the SREM. The values of ϕ (azimuth angle) on the horizontal axis follow curved lines and directly correspond only to the line $\theta = 90^\circ$.

the figure. The plot (and all subsequent plots of response functions) uses the area-conserving pseudocylindrical Mollweide projection to display the response for all 648 directions around the SREM.

3.6.6 Simulation Error and Statistics

The outcome of Geant4 simulations presented in this work has three sources of error: first of all, the simulations as such are *per se* inaccurate (because of the very fact that they are simulations, see the brief discussion in Section 3.2).

Secondly, the SREM geometry is modified for this work (replacing the electronics parts of the instrument with an aluminium shield and not simulating the full spacecraft geom-

Table 3.3: Example of calculating the error of the directional response function of channel *TC1* for 100 MeV protons.

θ [deg]	ϕ [deg]	C_i [#]	N_i [#]	$\frac{\sqrt{C_i}}{N_i}$	R_i [cm^2]	$\Delta R_i = r^2 \pi \frac{\sqrt{C_i}}{N_i}$
5	5	1107	10^6	$3.32716e - 05$	0.6816	0.02048708
15	5	1062	10^6	$3.25883e - 05$	0.6539	0.02006636
25	5	692	10^6	$2.63059e - 05$	0.4261	0.01619793
\vdots	\vdots	\vdots	\vdots	\vdots	\vdots	\vdots
85	5	135	10^6	$1.16190e - 05$	0.8312	0.00715429
95	5	150	10^6	$1.22474e - 05$	0.9236	0.00754133
\vdots	\vdots	\vdots	\vdots	\vdots	\vdots	\vdots
155	5	2	10^6	$1.41421e - 06$	0.0012	0.00087072
165	5	3	10^6	$1.73205e - 06$	0.0018	0.00106651
175	5	15	10^6	$3.74166e - 06$	0.0092	0.00230392

etry). In particular, this results in an error of the directional response function on the backside of the instrument around spherical angles of $\phi = \pm 180^\circ$ and $\theta = 90^\circ$.

The third source of error is poor statistics of the simulation, i.e. low confidence in a result due to an insufficient number of primary particles being simulated and reaching the detector. Assuming N_i primary particles and C_i ‘successes’ (C_i particles are detected), then the success rate is

$$\frac{C_i}{N_i} \pm \frac{\sqrt{C_i}}{N_i} \quad (3.11)$$

with standard deviation $\frac{\sqrt{C_i}}{N_i}$.

Based on error propagation, the error of ΔR_i of the response function R_i can be calculated:

$$\Delta R_i = r^2 \pi \frac{\sqrt{C_i}}{N_i} \quad (3.12)$$

Table 3.3 shows an example calculation of the error ΔR_i , again for the case of 100 MeV protons in channel *TC1*.

3.6.7 Practical Considerations

The SREM simulations were run on a cluster computing system at ESA TEC-EES. 70 CPUs could be used in parallel. It takes $\approx 6\text{ s}$ to obtain one single response function for

3 SREM Simulations

defined values of E , θ and ϕ . A complete set of θ and ϕ values for a single monochromatic energy takes 64 min. Finally, for a set of 70 energies distributed between 10 MeV and 500 MeV, the net computing time is 74 h, not considering any pre- or post-processing.

4 Directional SREM Response to Protons and Electrons

4.1 Directional Response $R(\theta, \phi, E)$ to Protons

The directional response $R(\theta, \phi, E)$ was obtained for 648 spherical directions of incidence and 74 different primary proton energies E between 10 MeV and 500 MeV ¹. Not all illustrations can be given for all energies within the scope of this thesis. The directional responses for 50 MeV , 75 MeV , 100 MeV and 150 MeV have been selected and are presented in the figures that follow in this chapter. Every row represents a specific channel, and the colour-coding is the same along each row to allow for easy comparison between the response at different energies. Every column represents a discrete energy.

For purposes of comparison and reference, the spherical response, i.e. the response $R_{4\pi}(E)$ without considering any directional dependency, is shown after the directional response. $R_{4\pi}(E)$ is reconstructed from the directional response $R(\theta, \phi, E)$ obtained in this work by calculating the 4π -average of $R(\theta, \phi, E)$:

$$R_{4\pi} = \frac{1}{4\pi} \sum_{i=1}^{648} \int \int R \sin(\theta) d\theta d\phi = \frac{1}{4\pi} \sum_{i=1}^{648} R_i \delta s_i = \frac{r^2}{4} \sum_{i=1}^{648} \frac{C_i}{N_i} \delta s_i \quad [\text{cm}^2] \quad (4.1)$$

The spherical response has been determined earlier in simulations performed by Bühler et al. [8], using a spherical isotropic source, without any angular resolution and with a binned energy resolution (Bühler et al. [8] had simulated energy intervals instead of discrete energies). These results are plotted alongside the spherical response obtained in this work. The geometric model of the SREM in the simulations by Bühler et al. [8] included a modified ground plate but retained the electronics parts of the instrument. The resulting spherical responses differ slightly for that reason (see next sections).

¹The simulated primary proton energies were (in MeV): 10, 15, 20, 25, 27.5, 30, 32.5, 35, 37.5, 40, 42.5, 43, 43.5, 44, 44.5, 45, 45.5, 46, 47.5, 50, 51, 52, 52.5, 53, 54, 55, 57.5, 60, 62.5, 65, 67.5, 70, 72.5, 75, 77.5, 80, 82.5, 85, 87.5, 90, 92.5, 95, 97.5, 100, 102.5, 105, 107.5, 110, 112.5, 115, 117.5, 120, 125, 130, 135, 140, 145, 150, 155, 160, 165, 170, 175, 180, 190, 200, 225, 250, 275, 300, 350, 400 and 500.

4.1.1 Total Channels $TC1$, $TC2$ and $TC3$

Referring to Table 3.1, channels $TC1$, $TC2$ and $TC3$ count particles depositing more than 0.085 MeV in the respective detectors $D1$, $D2$ and $D3$. As such, these channels are ‘Total Channels’ (therefore their name TC), sensitive to particles over a wide energy range (as discussed in Section 3.3, higher energy particles deposit less energy as compared to a lower energy particle).

The directional responses of $TC1$, $TC2$ and $TC3$ are illustrated in Figure 4.1. In this figure, all plots share the same colour scale which allows for easy intercomparison.

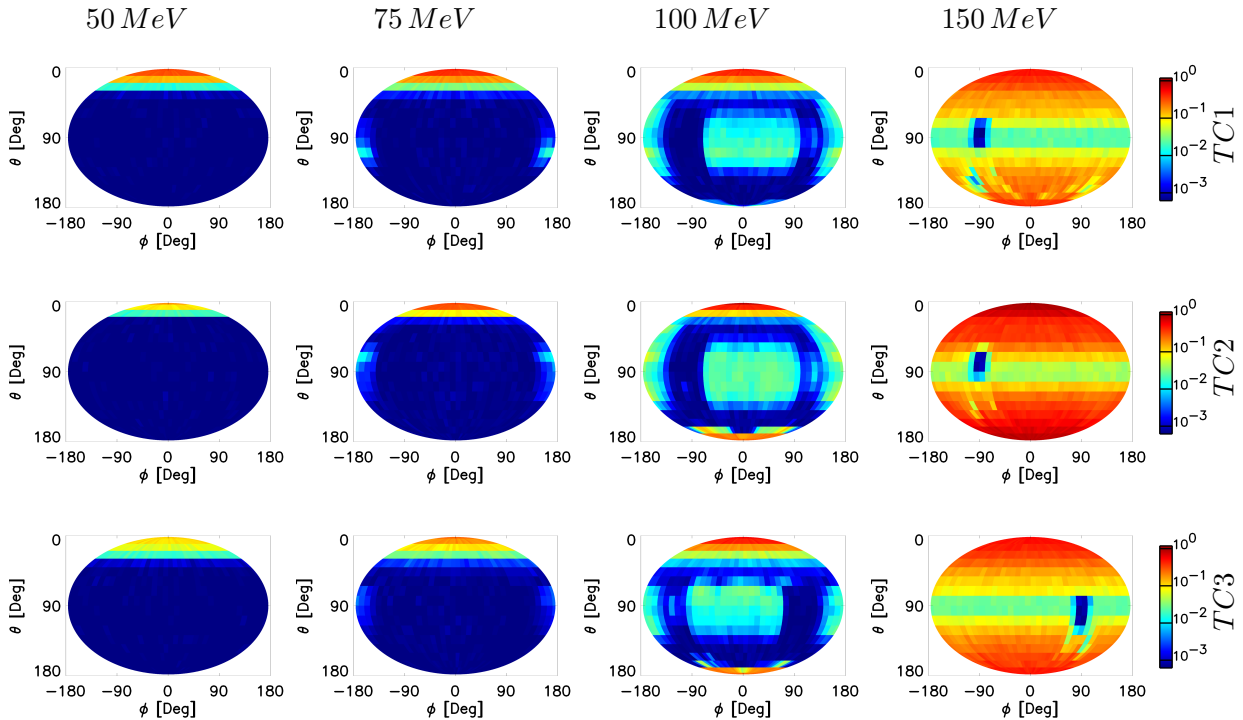


Figure 4.1: Directional response $R(E, \theta, \phi)$ of channels $TC1$, $TC2$ and $TC3$. The omnidirectional characteristic of these channels at high energies is clearly visible. All plots share the same colour scale.

- At 50 MeV , the total channels detect protons only through the main instrument entrance (20° opening angle) around $\theta = 0^\circ$.
- As the proton energy rises to more than 75 MeV , the back ($\phi = \pm 180^\circ$, $\theta \pm 90^\circ$) of the instrument (modified for simulations) can be penetrated.

- Finally, protons are detected through the bottom ($\theta = 180^\circ$) and the front of the instrument ($\theta = 90^\circ, \phi = 0^\circ$) from $\approx 100\text{ MeV}$ onwards.

$TC2$ and $TC3$ are the first to show response through the bottom; $TC1$ is better shielded by $D2$ and the aluminium-tantalum layer that is located between $D1$ and $D2$.

- For high energies (150 MeV is given as an example), $TC1$, $TC2$ and $TC3$ approximate omnidirectional detectors; they detect protons from practically all directions.
- Note the shielding (area of no response) at $\theta = 90^\circ, \phi = -90^\circ$ for $TC1$ and $TC2$ and at $\phi = +90^\circ$ for $TC3$: this is due to the diode assembly $D3$ shielding diodes $D1$ and $D2$ and vice versa.

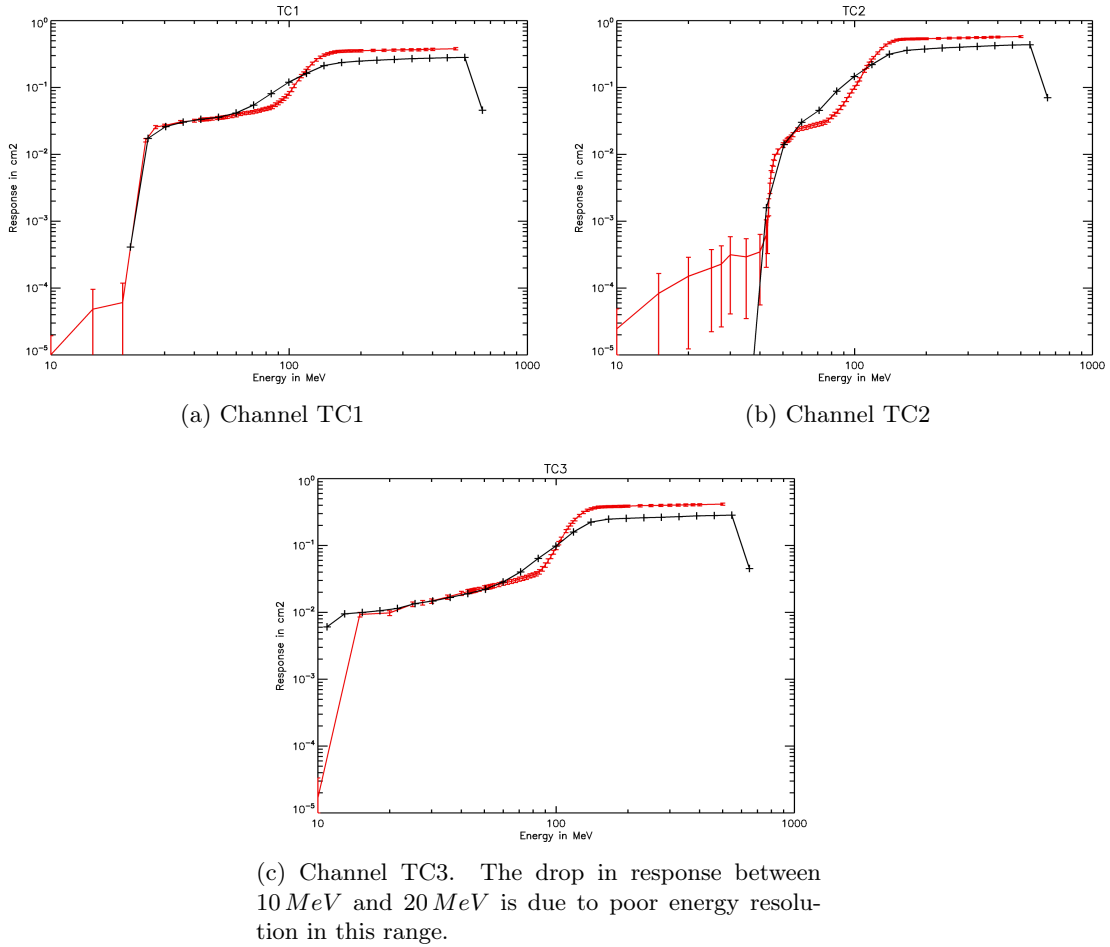


Figure 4.2: Comparison of 4π -averaged response functions of channels $TC1$, $TC2$ and $TC3$ obtained in this work (red, with errorbars) with previous data (black)

The spherical response $R_{4\pi}$ (Figure 4.2) indicates the low-energy cut-off for each channel and the general response characteristic. The rise in overall response as the instrument back, bottom and front become transparent to protons is clearly visible. The ‘step’ at $\approx 100 \text{ MeV}$ in the spherical response function is due to the response through the bottom of the instrument. The difference between the response obtained in this work (red) and previous data is due to the modified geometry of the instrument. The 1 cm aluminium plate that was added for the simulation is a stronger shield than the electronics parts of the SREM it replaces. The unmodified instrument ground plate used in this work, on the other hand, is a less strong shield. These differences lead to a less steep rise of the response, followed by an ‘overshoot’ at higher energies.

4.1.2 Channels $S12 - S15$

The directional responses of channels $S12$, $S13$, $S14$ and $S15$ are illustrated in Figure 4.3. In this figure, all plots share the same colour scale which allows for easy intercomparison.

$S12$ and $S13$ differ from $TC1$ only in the minimum required energy deposition in the detector diode (0.085 MeV for $TC1$, 0.25 MeV for $S12$ and 0.6 MeV for $S13$), corresponding to different high-energy cut-offs. Otherwise they exhibit a completely equivalent behaviour.

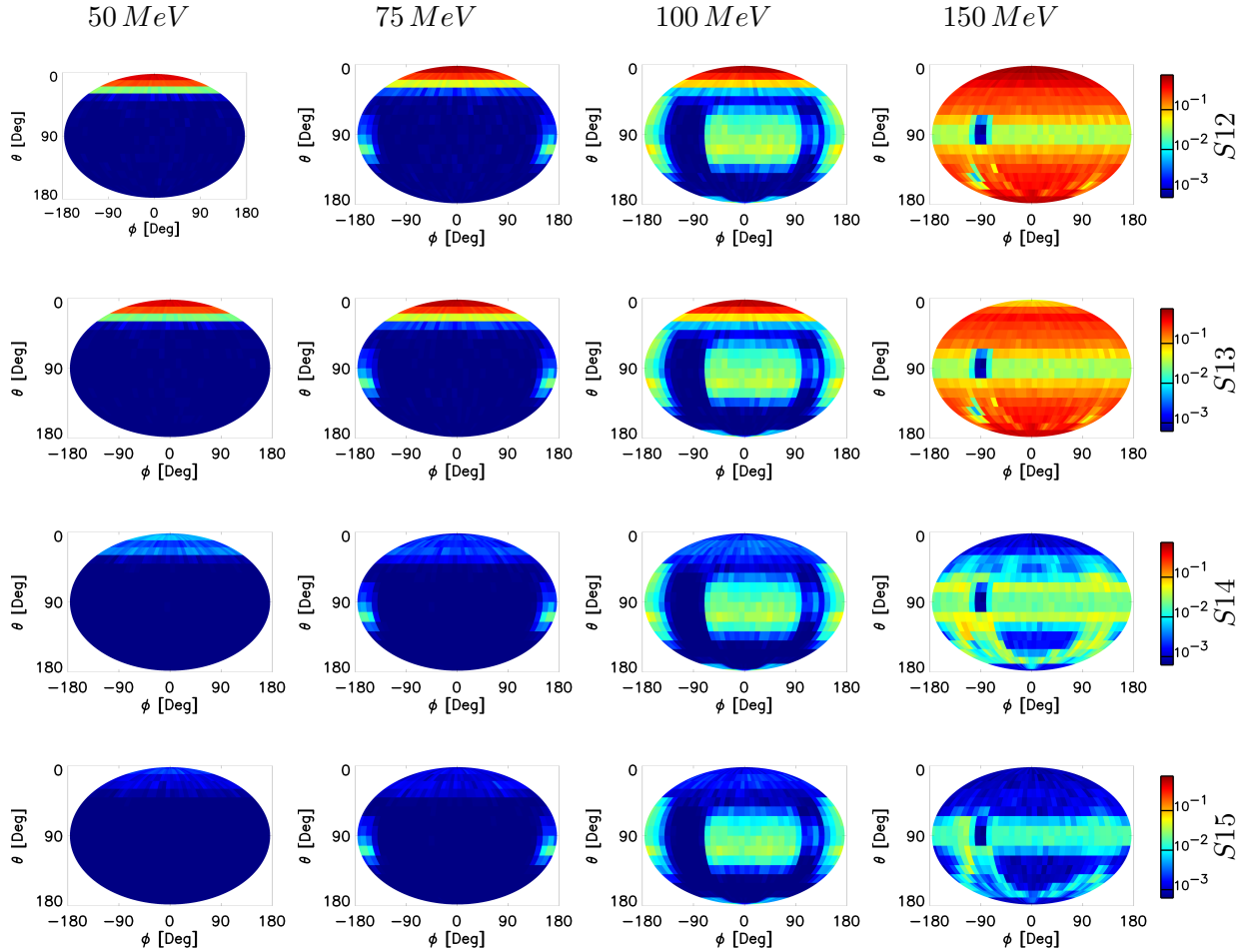


Figure 4.3: Directional response $R(E, \theta, \phi)$ of channels $S12$, $S13$, $S14$ and $S15$. The omnidirectional characteristic of these channels at high energies is clearly visible. All plots share the same colour scale.

- At ‘low energies’ around 50 MeV , channels $S12 - S15$ show response only through the main entrance around $\theta = 0^\circ$ (20° opening angle).
- Consequently, for energies up until 150 MeV , channels $S12$ and $S13$ show a response equivalent to the one of $TC1$ in the previous section: at 75 MeV , particles detected through the back of the instrument ($\phi = \pm 180^\circ$) can be observed before the front of the instrument around $\phi = 0^\circ$ becomes transparent at 100 MeV .
- For $S13$, the energy cut-off starts to become visible at 150 MeV as the response through the top decreases in comparison to $S12$ ($0.8 \cdot 10^{-2}$ instead of $2 \cdot 10^{-2}\text{ cm}^2$).

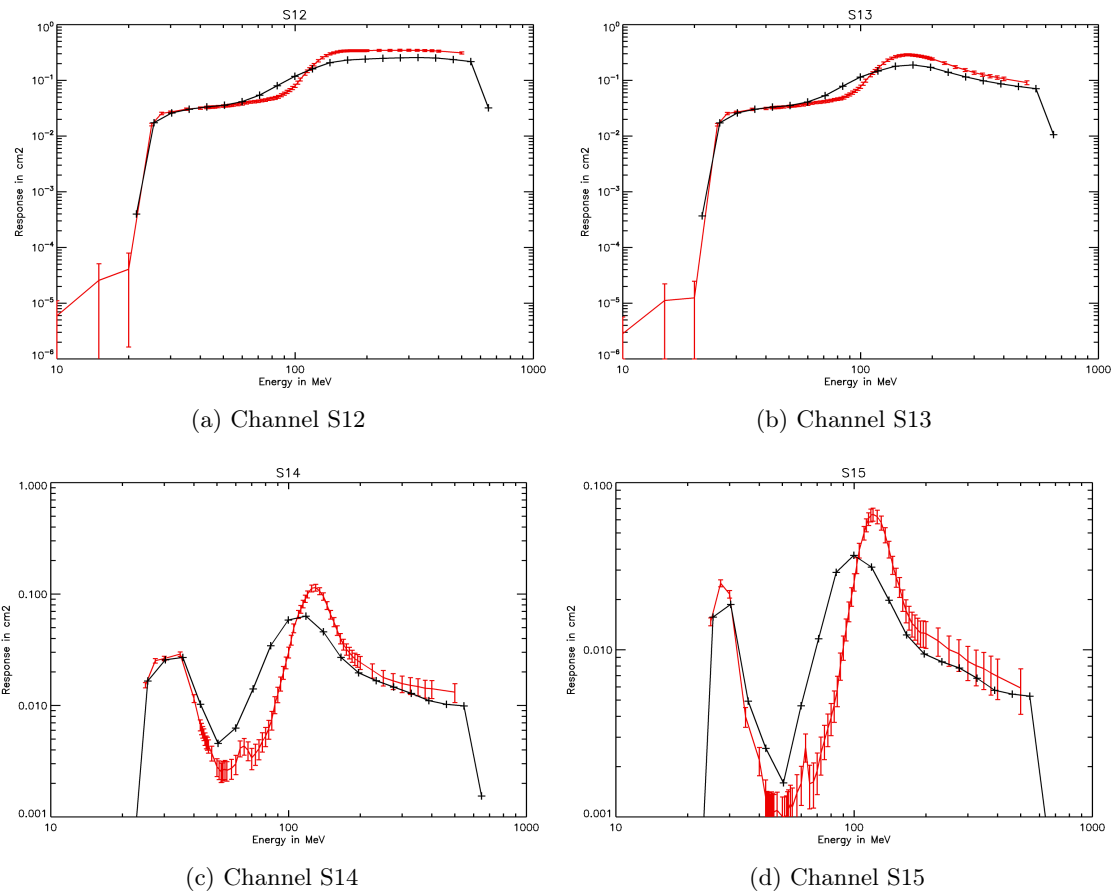


Figure 4.4: Comparison of 4π -averaged response functions of channels $S12$, $S13$, $S14$ and $S15$ obtained in this work (red, with errorbars) with previous data (black)

$S14$ and $S15$ are different in the characteristic of their response. As they require a (comparatively) high energy deposition (Table 3.1), protons through the main instrument

entrance with a primary energy above a specific threshold cannot be detected.

- For $S14$, the minimum energy deposition is 2 MeV ; there is no response through the main entrance at energies larger than $\approx 50\text{ MeV}$.
- For $S15$, the minimum energy deposition is 3 MeV ; there is no response through the main entrance at energies larger than $\approx 40\text{ MeV}$.
- As the proton energy rises to 100 MeV and above, the back and front become transparent: the shielding in these directions attenuates the proton energy to a level that allows them to deposit sufficient energy in $D1$ to be counted in channels $S14$ and $S15$.

$S14$ and $S15$ therefore have completely different directional characteristics in comparison to $S12$ and $S13$, indicated also by their spherical response graphs (Figure 4.4).

The response graphs of $S14$ and $S15$ have two distinct local maxima each: the lower energy maximum is due to the response through the main instrument entrance; the higher energy maximum is due to the response through the back, the front and the side of the instrument. Due to the modified back of the geometric model of the instrument, the response obtained in this work shows a considerably different higher energy maximum.

The spherical response of channels $S12$ and $S13$ again indicate the equivalence to $TC1$. The decline in response above $\approx 100\text{ MeV}$ as the channels start reaching their high-energy cut-offs is visible.

4.1.3 Coincidence Channels $C1 - C4$

Since coincidence detection in $C1$, $C2$, $C3$ and $C4$ requires the deposition of energy in silicon diodes $D1$ and $D2$ simultaneously, only particles with a trajectory through both detector masses are counted. Therefore, the coincidence channels are not susceptible to particles incident from elevation angles between 60° and 120° .

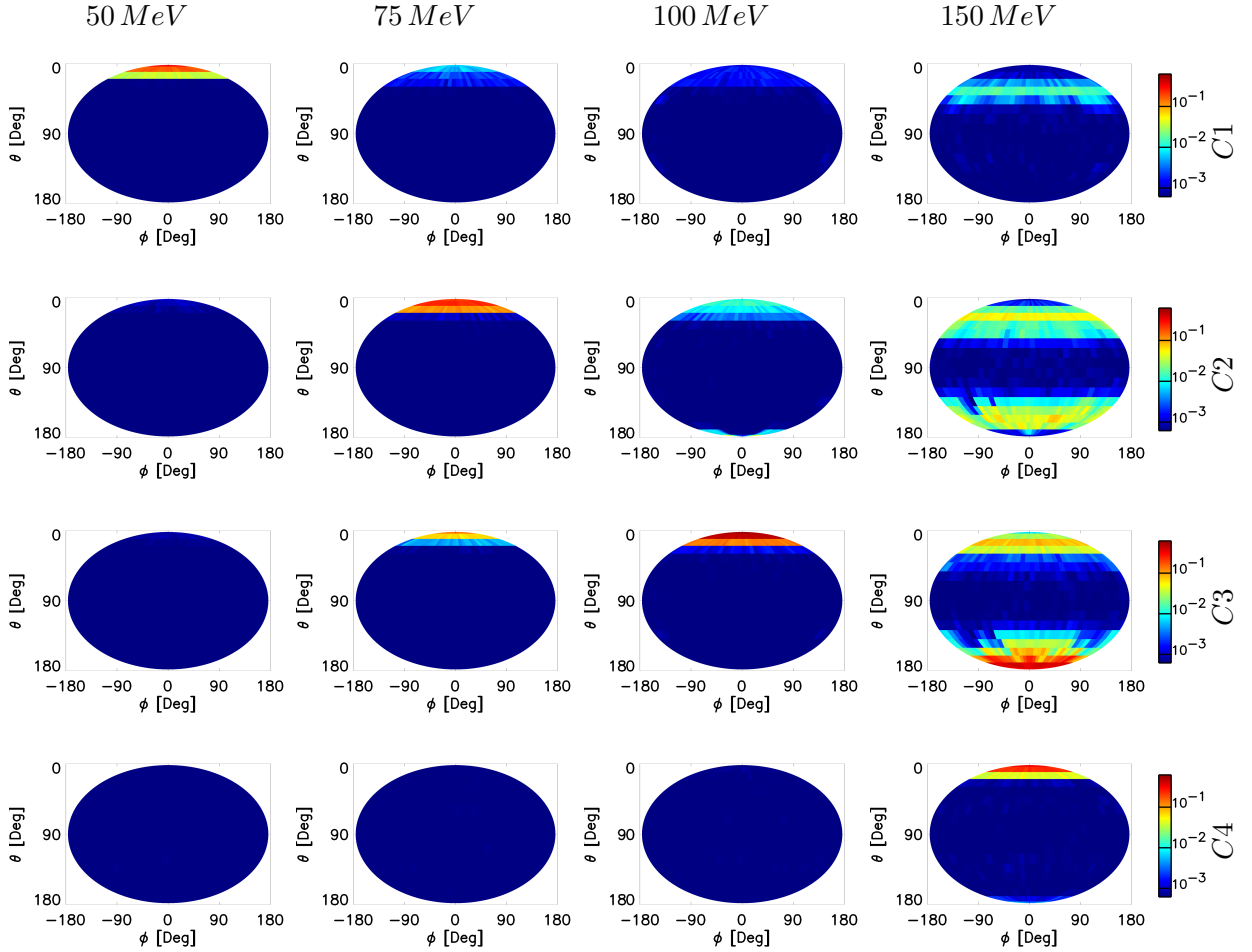


Figure 4.5: Directional response $R(E, \theta, \phi)$ of channels $C1$, $C2$, $C3$ and $C4$. The omnidirectional characteristic of these channels at high energies is clearly visible. All plots share the same colour scale.

The directional response of the coincidence channels is shown in Figure 4.5. In this figure, all plots share the same colour scale which allows for easy intercomparison.

- The coincidence channels $C1$ to $C4$ all show similar characteristics, but in different energy ranges.
- $C1$, the ‘low energy’ coincidence channel, detects particles from $\approx 50\text{ MeV}$ upwards and does not show any response through the instrument bottom.

To be counted in $C1$, a proton incident through the instrument bottom would have to first deposit more than 2 MeV in $D2$, pass the aluminium-tantalum layer between $D2$ and $D1$ and then deposit more than 0.6 MeV in $D1$. This process is energetically impossible: A proton depositing 2 MeV or more in $D2$ would have to be a proton with lower primary energy than is required to traverse the aluminium-tantalum layer.

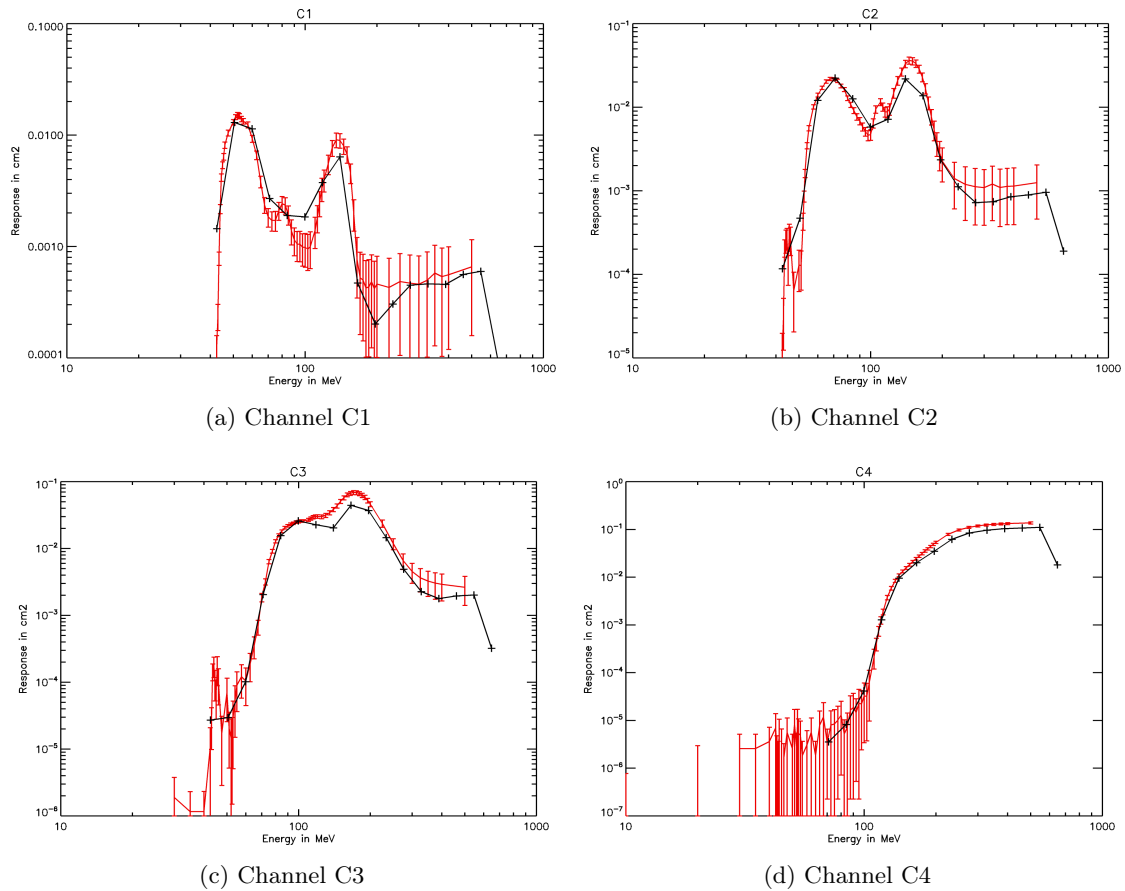


Figure 4.6: Comparison of 4π -averaged response functions of channels $C1$ - $C4$ obtained in this work (red, with errorbars) with previous data (black)

- As the energy rises, $C2$, $C3$ and $C4$ start detecting particles in the same manner

as $C1$.

- $C2$, $C3$ and $C4$, unlike $C1$, also show response through the instrument bottom as their energy deposition requirements in $D2$ are lower (0.6 MeV for $C2$, $C3$ and 0.085 MeV for $C4$).
- The ‘high energy’ coincidence channel is $C4$.

The spherical responses of the coincidence channels $C1$, $C2$ and also $C3$ show two distinct response peaks. The lower energy peak is due to detector response through the main instrument entrance. For $C2$ and $C3$, the high energy peak is due to both instrument response through the bottom and response at an elevation of $\theta = 30^\circ$ to 60° and $\theta = 120^\circ$ to 150° , as the entrance window shielding becomes transparent. In the case of $C1$, the higher energy peak is not due to instrument response through the bottom but due to the mentioned response at an elevation of $\theta = 30^\circ$ to 60° only.

4.1.4 Other Channels (S_{25} , S_{32} , S_{33} , S_{34})

The directional responses of channels S_{25} , S_{32} , S_{33} and S_{34} are illustrated in Figure 4.7. In this figure, the channels use different colour mappings due to their different energy ranges.

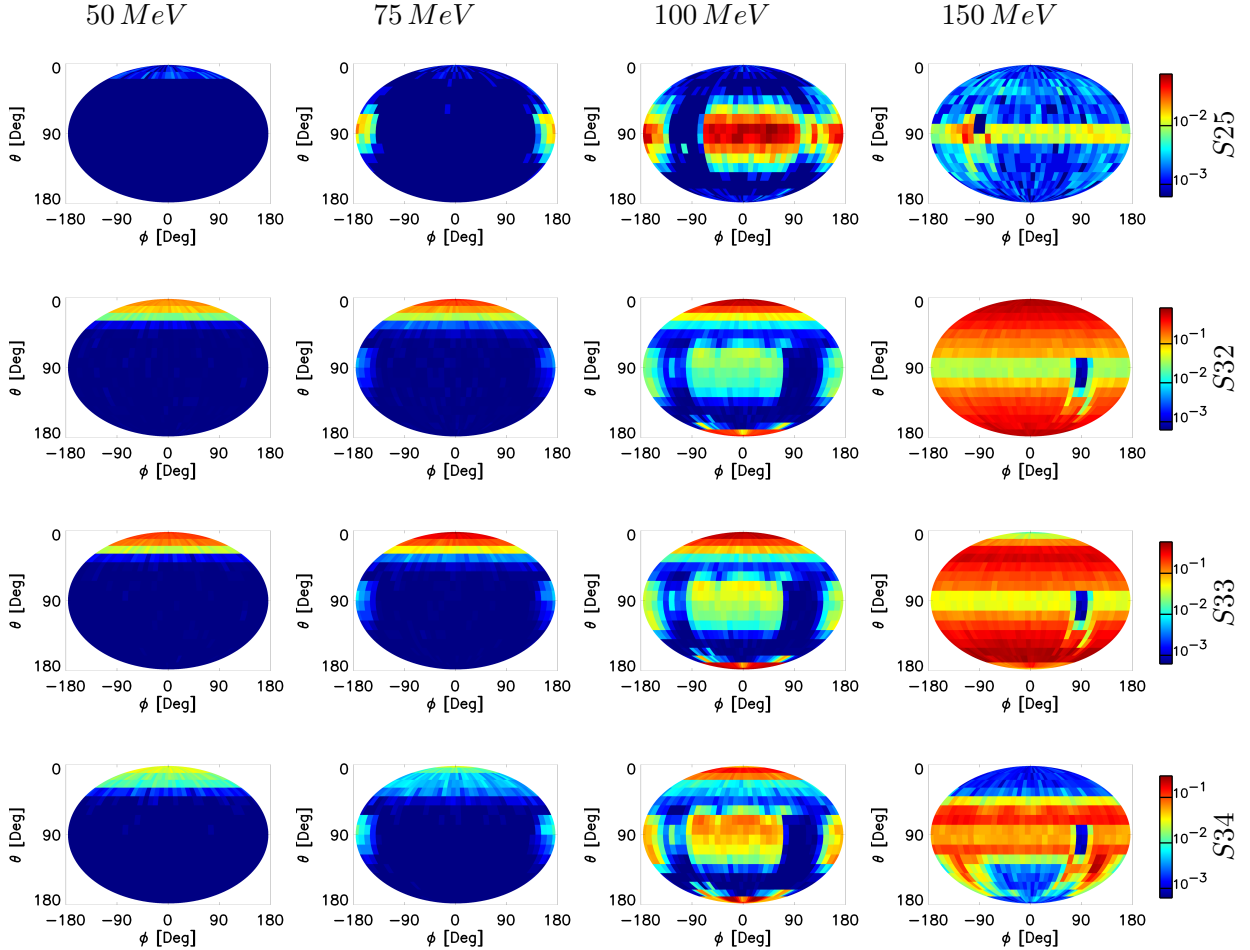


Figure 4.7: Directional response $R(E, \theta, \phi)$ of channels S_{25} , S_{32} , S_{33} and S_{34} . The omnidirectional characteristic of S_{32} and S_{33} at high energies is clearly visible.

Channels S_{32} , S_{33} and S_{34} in diode D_3 roughly correspond to S_{12} , S_{13} and S_{14} in diode D_1 (Table 3.1) and show a similar directional response. The main differences in the response are due to different shielding of the main entrance openings (the entrance of D_3 is less strongly shielded). Naturally, the region of less response is in direction $\theta = 90^\circ$,

4 Directional SREM Response to Protons and Electrons

$\phi = +90^\circ$ where $D3$ is shielded by $D1$. With respect to $S25$, the very directional characteristic shall be noted.

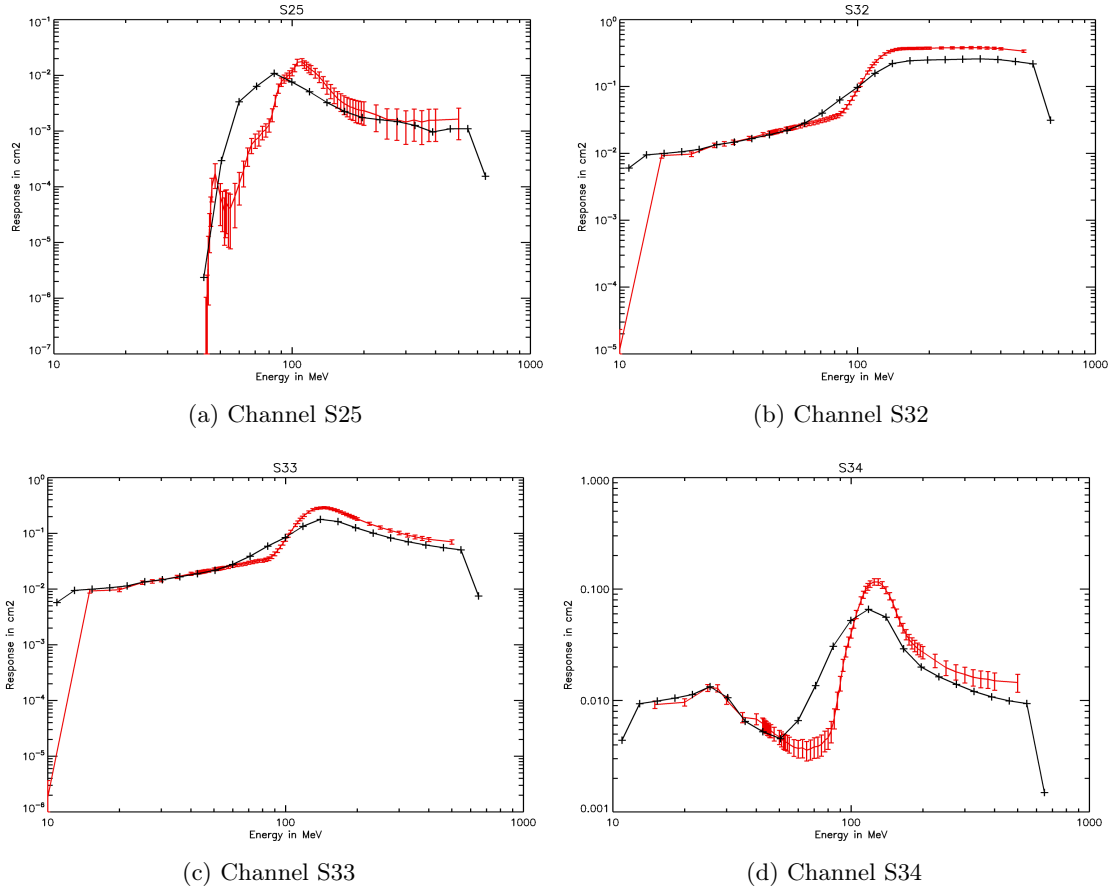


Figure 4.8: Comparison of 4π -averaged response functions of channels $S25$, $S32$, $S33$ and $S34$ for coincidence channels obtained in this work (red, with errorbars) with previous data (black)

The correspondence between the channels of diode $D3$ and diode $D1$ can also be observed in their spherical response, as shown in Figure 4.8. For $S25$, the data obtained in this work and previous data differ due to the aforementioned differences in the simulated geometries.

4.2 Integrated Response to Protons

The directional response function over wide energy ranges is not easily illustrated. Representative energies (50 MeV , 75 MeV , 100 MeV , 150 MeV) were chosen to convey the response characteristic of each channel. The integrated response is the directional response function $R(\theta, \phi, E)$ integrated over energy

$$R_{int}(\theta, \phi) = \int_{10\text{ MeV}}^{500\text{ MeV}} R(\theta, \phi, E) dE$$

and allows for an estimation of the directional characteristics of a channel in a single figure. Figure 4.9 shows the directional sensitivity of the coincidence channels using the integrated response.

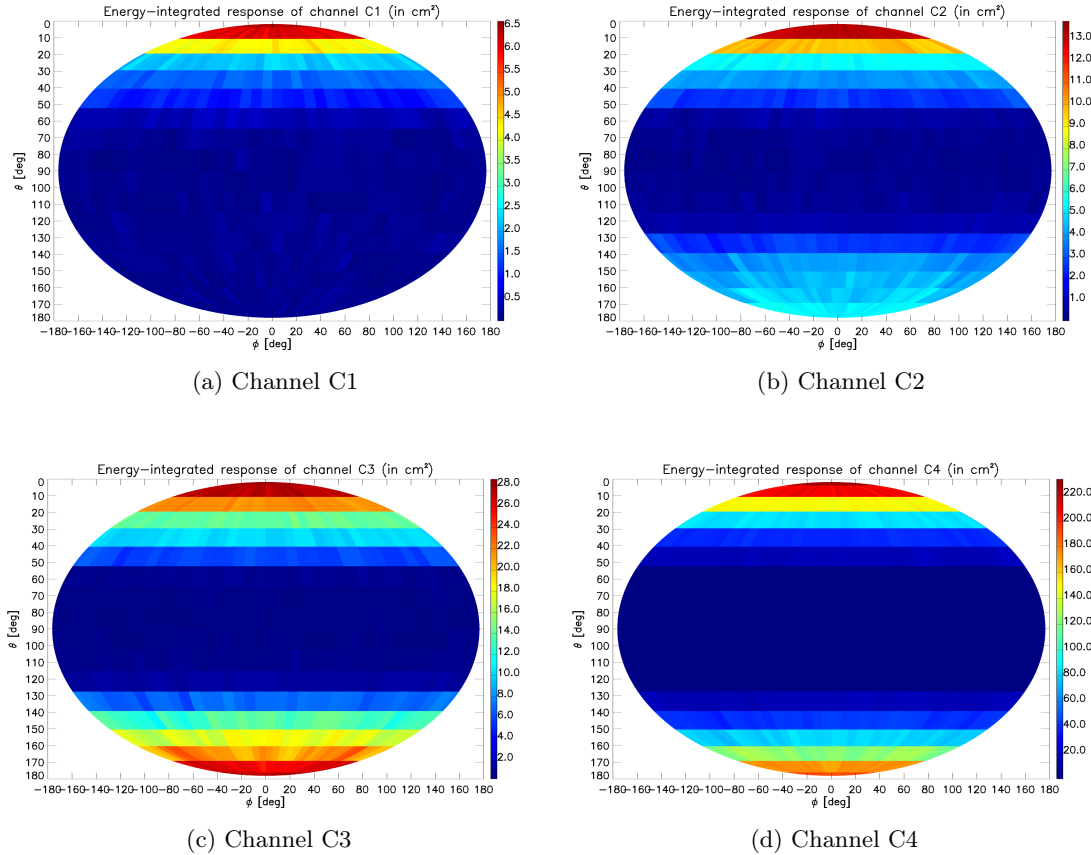


Figure 4.9: Energy-integrated SREM response of channels $C1 - C4$

4 Directional SREM Response to Protons and Electrons

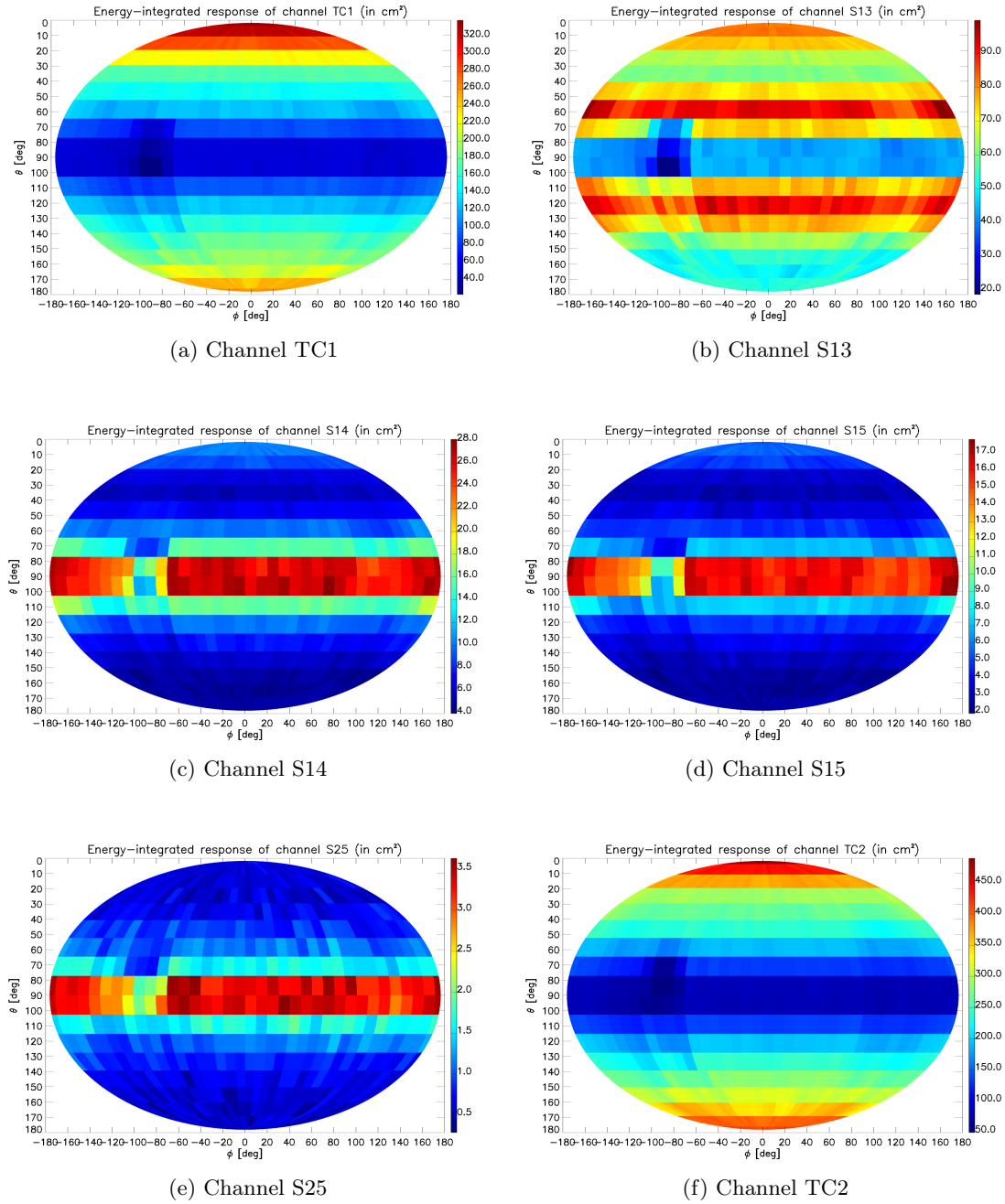


Figure 4.10: Energy-integrated SREM response of channels $TC1$, $S13$, $S14$, $S15$, $S25$ and $TC2$.

Similarly, Figure 4.10 indicates the omnidirectional characteristic of *TC1*, *TC2* and *S13* and illustrates the more directional response of *S14* and *S15*.

4.3 Directional Response $R(\theta, \phi, E)$ to Electrons

The main emphasis of this work is on the SREM response to protons due to the importance of protons in the inner Van Allen belt that is traversed by PROBA-1. However, the same simulation setup as is used for protons can be used for simulating the SREM response to electrons: the directional response of the SREM to electrons was therefore determined for diode $D3$, 648 directions of incidence and 10 different discrete energies between 0.7 MeV and 10 MeV . As examples, the response for primary electron energies for 0.7 MeV , 1 MeV , 5 MeV and 10 MeV are shown in Figure 4.11. Channels $S32$, $S33$ and $S34$ share the same colour mapping. $TC3$ shows a response that is higher by one order of magnitude and has its own colour mapping.

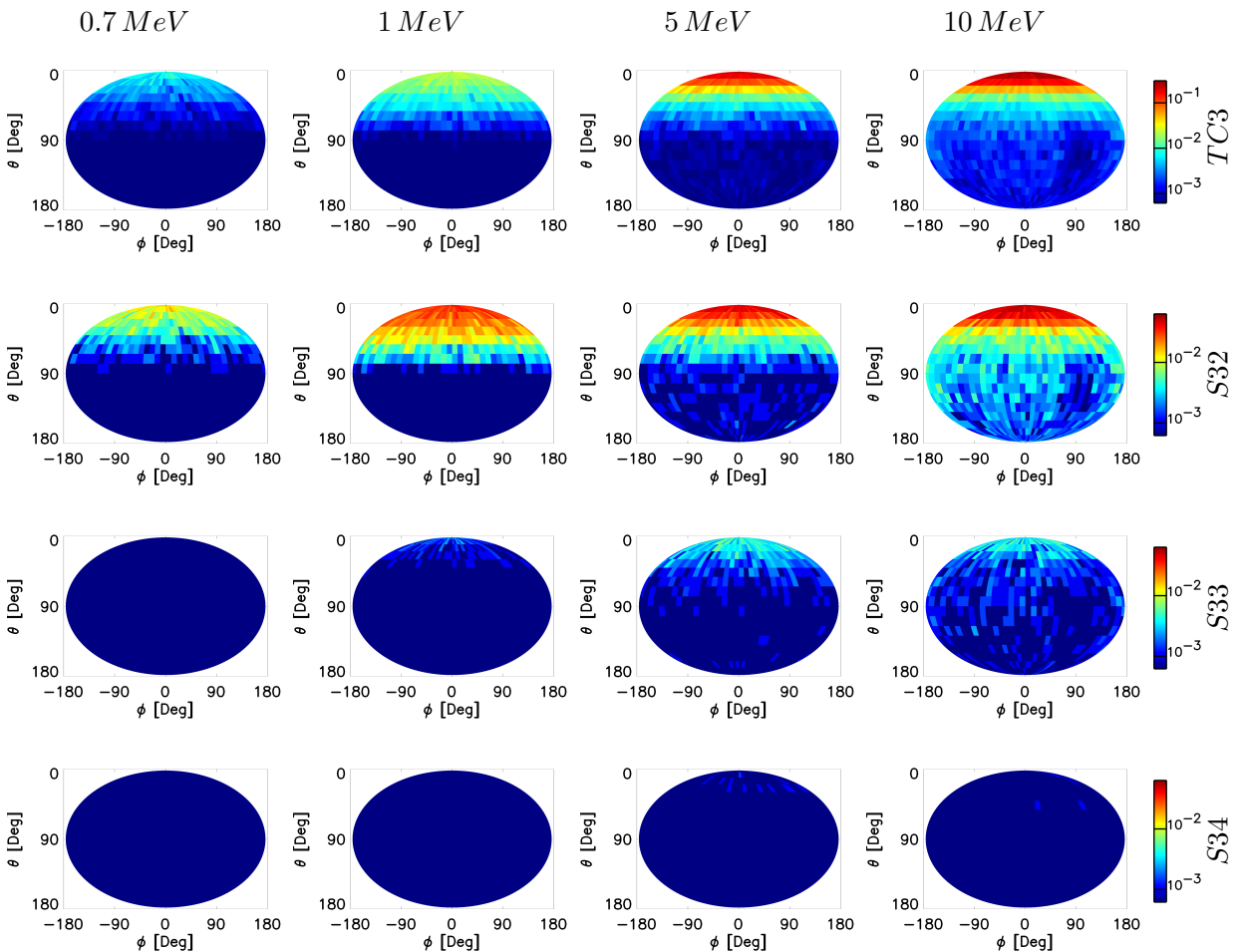


Figure 4.11: Directional response $R(E, \theta, \phi)$ of channels $TC3$, $S32$, $S33$, $S34$ to electrons

5 Flux Models

Chapter 4 presented the directional response function of the SREM that was obtained in GRAS/Geant4 simulations. In Chapter 5, models for the particle flux and the Earth's magnetic field are discussed. In particular, a model for flux anisotropies in LEO is introduced. Flux models, anisotropy models and magnetic field models are all required if countrates for the SREM are to be calculated.

5.1 AP-8 Omnidirectional Flux

AP-8 is a model for proton fluxes in a wide range of Earth orbits, covering L-values up to 6.6 Earth radii. First published by Vette [35] in 1976, it is based on measurements from several military and scientific satellites typically carrying solid state or scintillation detectors. In spite of its age, the AP-8 model still serves as a standard reference model. It consists of two independently-obtained datasets, AP-8 MIN and AP-8 MAX, measured during solar minimum and maximum, respectively. AP-8 MIN and AP-8 MAX themselves are static models (i.e. no time-dependent dynamic) and give flux values that correspond approximately to the long-term median flux¹. For a given coordinate in (B,L)-space, AP-8 gives an integrated, omnidirectional flux spectrum. The energy range from 0.1 MeV to 400 MeV protons is covered.

The AP-8 model, due to its omnidirectional characteristic, works best for long-term averaged flux predictions and total dose calculations, when anisotropies of flux even out over the course of time or are non-existent. For application in the PROBA-1 orbit, provisions for anisotropies in the flux have to be made, i.e. AP-8 has to be extended to account for the specific direction from which the flux is incident on the satellite and the SREM. The same provisions are necessary for modelling the flux experienced by the ISS. As a three-axis stabilised spacecraft, the space station has a preferred attitude. Different segments are therefore subject to vastly different flux spectra.

For protons in the inner Van Allen belt with energies above 25 MeV , protons fluxes are considered stable (Vette [35]).

The geomagnetic field has changed since the measurements that AP-8 is based on have been recorded, and with it has changed the location of the SAA. Its East-West movement

¹AP-8 gives the mean of logarithmic flux values, leading to the characteristic of a median value.

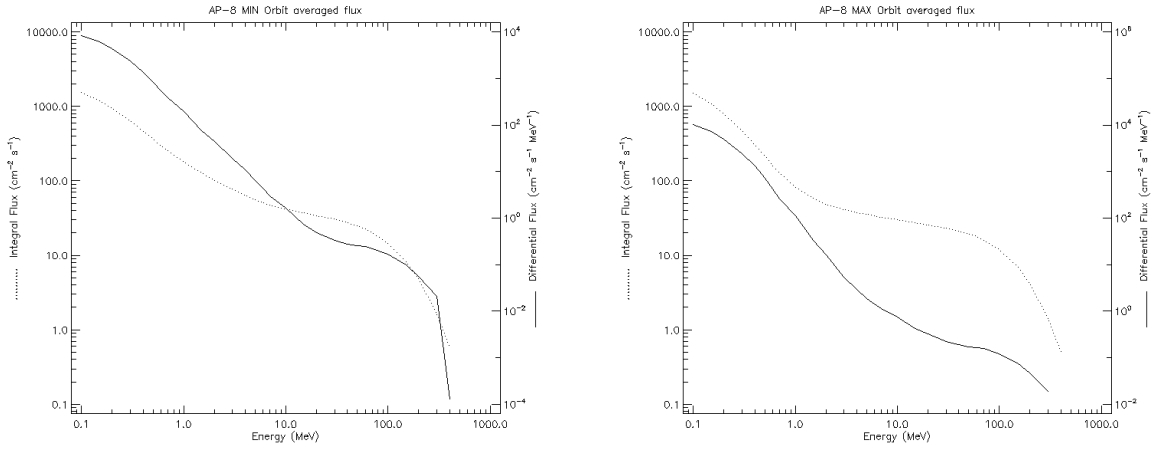


Figure 5.1: Proton fluxes in the orbit of PROBA-1 as predicted by the AP-8 MIN (left) and AP-8 MAX (right) models for March 31st, 2009. Figures generated using SPENVIS [4].

(longitudinal movement) is called secular drift and can be considered together with the AP-8 model to improve the fidelity of the predicted flux spectra.

5.2 Flux Anisotropies

Particle flux at a particular point in space is in general not isotropic, i.e. the flux depends on the direction that is observed. In the orbit of PROBA-1, two effects render the flux anisotropic: the East-West effect and the pitch angle distribution. The East-West effect stems from the interaction of radiation belt particles with the Earth's atmosphere; the pitch angle distribution is due to particle gyration around magnetic field lines and their mirroring in an inhomogeneous magnetic field.

The East-West effect and the pitch angle distribution are discussed below. For the special case of the SREM on PROBA-1, the East-West effect has very little effect due to the orientation of the satellite. The pitch angle distribution, however, is highly relevant.

5.2.1 East-West Effect

The East-West effect was first measured by Heckman and Nakano [19] and explained theoretically by Lenchek and Singer [26]. Particles incident on a detector from the Western direction (i.e. moving from West to East) have their guiding centre above the

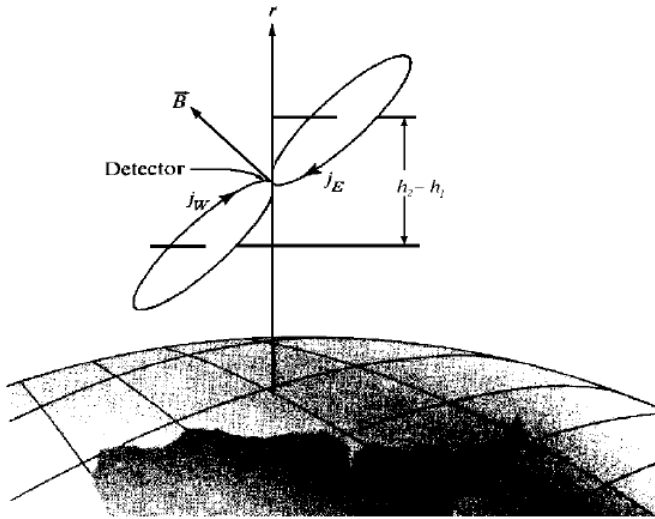


Figure 5.2: Illustration of the East-West effect. Two examples of charged particles, one with a guiding centre below and one with a guiding centre above the satellite are shown, representing an East-ward flux j_W and a West-ward flux j_E . These fluxes differ in relative strength.

detector. In contrast to that, particles incident on a detector from the Eastern direction (i.e. moving from East to West) have their guiding centre below the detector.

At low altitudes and given a steep atmospheric density gradient (atmospheric scale height), particles with a guiding centre below the satellite will experience significantly more atmospheric absorption than particles with a guiding centre above the satellite. This leads to different particles fluxes from the East and the West (Figure 5.2).

The SREM on PROBA-1 is assumed to be unaffected by the East-West effect since the main entrance is never positioned in the East-West direction, but rather more aligned along the North-South meridian.

5.2.2 Pitch Angle Distribution

A charged particle gyrating around and moving along a magnetic field line has a certain pitch angle with respect to the field line. The pitch angle α is the angle between magnetic field vector \vec{B} and the particle's velocity vector \vec{v} . At its mirror points, a particle's pitch angle is 90° . Assuming an ideal dipole magnetic field, the pitch angle at any other location along the magnetic field line is given by

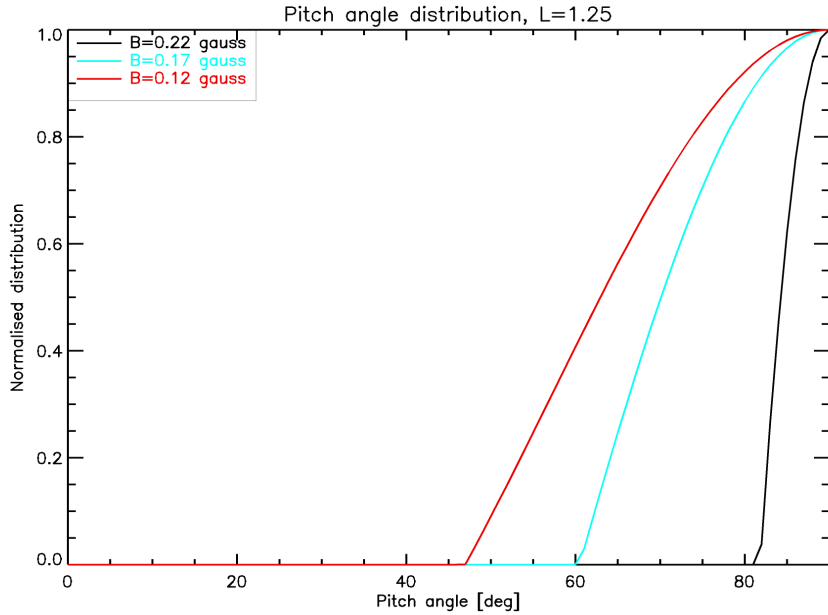


Figure 5.3: Normalised distribution of pitch angles for $L = 1.25$ Earth radii and various values of B

$$\sin^2(\alpha) = \frac{B_M}{B}$$

where B_M is the magnetic field strength at the mirror point and B is the magnetic field strength at the location in question.

At a specific location (B, L), particles with different pitch angles are encountered. Some particles are closer to their mirror point than others and therefore have a steeper pitch angle. At high magnetic latitudes, most encountered particles are close to their mirror points and the pitch angle distribution is a sharp peak around 90° . Near the magnetic equator, the peak of pitch angles is still centred around 90° , but much wider. Figure 5.3 shows the pitch angle distribution for one L-shell of the inner Van Allen belt ($L = 1.2$) and different magnetic latitudes B .

The figure is based on the Badhwar-Konradi model for pitch angle distribution (Badhwar and Konradi [3]) which is used in this work and is detailed in the next section. An alternative to the Badhwar-Konradi model is the Heckmann-Nakano model. As the Badhwar-Konradi model is applicable for a wider altitude range, it is chosen for this work.

5.3 Badhwar-Konradi Pitch Angle Distribution

The Badhwar-Konradi model starts from an omnidirectional flux $\mathcal{F}_{AP8}(B, L)$ as given by AP-8 and seeks to derive a unidirectional flux from it. In general, the derived unidirectional flux will be anisotropic. The derivation of a unidirectional flux from an omnidirectional flux is based on making some assumptions about the characteristics of the unidirectional flux, presented by Badhwar and Konradi [3]. In general, the omnidirectional flux $\mathcal{F}_{AP8} \left[\frac{\#}{cm^2 s} \right]$ and the unidirectional flux $F \left[\frac{\#}{cm^2 s sr} \right]$ are related by integration over the pitch angle

$$\mathcal{F}_{AP8}(B, L) = 4\pi \int_0^{\frac{\pi}{2}} F(B, L, \alpha) \sin(\alpha) d\alpha \quad (5.1)$$

at a specific position B, L . α is the pitch angle and the integration variable in this equation.

However, aside from this general relation, Badhwar and Konradi assume in particular that F can be written as the product of the omnidirectional flux \mathcal{F}_{AP8} and a dimensionless scale factor W_{BK} that introduces the anisotropy:

$$4\pi F(B, L, \alpha) = \mathcal{F}_{AP8}(B, L) W_{BK}(B, L, \alpha) \quad (5.2)$$

$\mathcal{F}_{AP8} W_{BK}$ on the right side of the equation represents an omnidirectional flux, i.e. a flux integrated over the whole sphere. The unidirectional F therefore has to be multiplied by 4π .

Badhwar and Konradi then make the following ansatz for F :

$$F(B, L, \alpha) = K \left(\frac{\sin(\alpha)}{\sqrt{B}} - \frac{\sin(\alpha_L)}{\sqrt{B}} \right) e^{-\beta \left(\frac{\sin(\alpha)}{\sqrt{B}} - \frac{\sin(\alpha_L)}{\sqrt{B}} \right)} \quad (5.3)$$

with $\alpha_L = \alpha_L(B, L)$ and $\beta = \beta(L)$. The parameter α_L is the loss cone angle at position (B, L) and β is a shape parameter with dimensions of $[\sqrt{G}]$. Both are discussed and derived in Section 5.3.1.

Using

$$\xi = \frac{\sin(\alpha)}{\sqrt{B}} - \frac{\sin(\alpha_L)}{\sqrt{B}},$$

(5.3) can be written as

$$F(B, L, \alpha) = K \xi e^{-\beta \xi}.$$

5 Flux Models

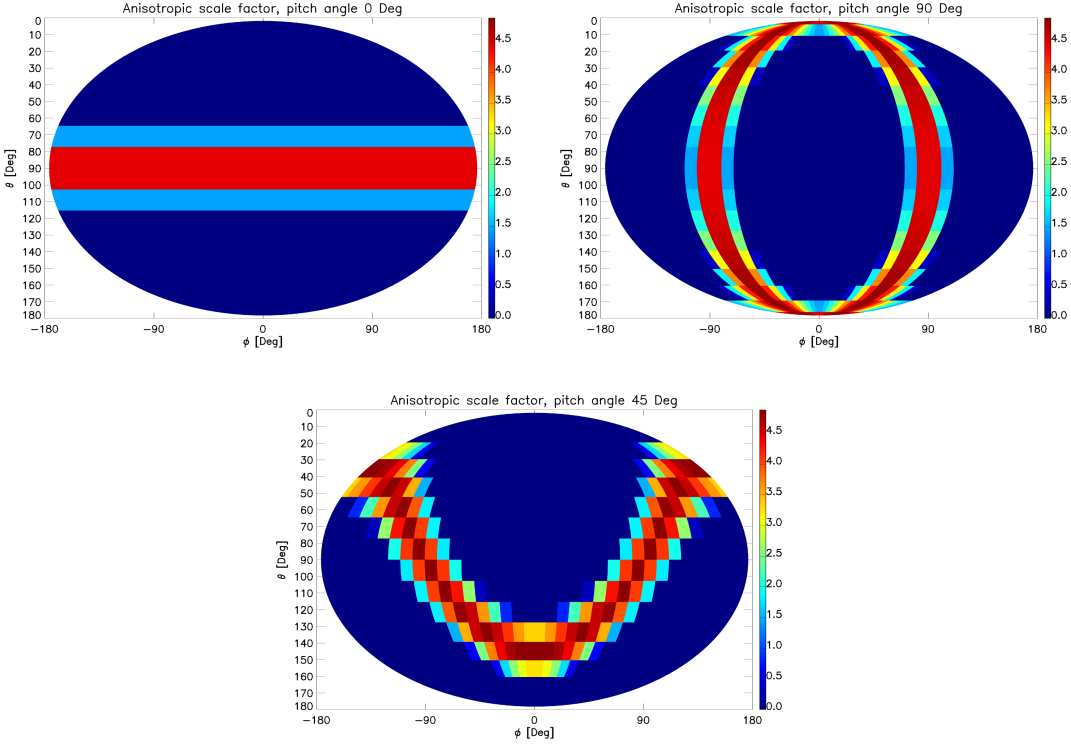


Figure 5.4: The anisotropic scale factor as given by the Badhwar-Konradi model for pitch angles of 0° (upper panel, left), 90° (upper panel, right) and 45° (lower panel). The anisotropic scale factor is used to introduce anisotropy in the AP8-model. All plots share the same colour mapping.

Comparing coefficients and requiring normalisation (performed in Appendix A), the factor K can be determined to be

$$K = \frac{\mathcal{F}_{AP8}}{4\pi \int_{\alpha_L}^{\pi/2} \xi e^{-\beta\xi} d\cos(\alpha)} \quad (5.4)$$

and the dimensionless scale factor $W_{BK}(B, L, \alpha)$ becomes

$$W_{BK}(B, L, \alpha) = \frac{\xi e^{-\beta\xi}}{\int_{\alpha_L}^{\pi/2} \xi e^{-\beta\xi} d\cos(\alpha)} \quad (5.5)$$

The directional flux observed by a detector in the direction with pitch angle α is

$$F(B, L, \alpha) = \frac{\mathcal{F}_{AP8}(B, L)}{4\pi} W_{BK}(B, L, \alpha) \quad (5.6)$$

This relationship can be used to obtain, for a specific location (B, L) the flux of particles with pitch angle α .

5.3.1 Determining α_L and β

The parameters α_L and β are determined and implemented following the procedure used in SPENVIS [4]. As outlined in a technical note by Kruglanski and Heynderickx [25], α_L is given by

$$\sin(\alpha_L) = \sqrt{\frac{B}{B_0}} \sin\left(\frac{\pi}{180} \frac{1}{p_1 + p_2 L}\right), \quad (5.7)$$

and β ($[\sqrt{G}]$) is given by

$$\beta = \frac{1}{p_3 + p_4 \ln L}. \quad (5.8)$$

Kruglanski and Heynderickx [25] derived the coefficients $p_1 - p_4$ by curve fits to the AP-8 model for a range of L-values and energies. The coefficients are therefore minimally energy and L-value dependent. The mean values used in this work (in accordance with SPENVIS) are given in Table 5.1.

Table 5.1: Coefficients for α_L and β

p_1	p_2	p_3	p_4
-0.032392	0.039836	0.13164	-8.8674

5.4 Magnetic Field Models

Both the AP-8 model and the Badhwar-Konradi pitch angle distribution require the spacecraft position in (B,L)-coordinates as an input parameter. In order to convert a latitude, longitude, altitude coordinate to (B,L)-space, a model of the magnetic field is required.

The most widely used magnetic field model is the International Geomagnetic Reference Field (IGRF). Additionally, the geomagnetic field model by Jensen and Cain [22] is of importance as it was used when compiling the AP-8 model.

5.4.1 Choice of (B,L)-Coordinates

Evaluating the AP-8 model at a specific location requires the input of McIlwain's (B,L)-coordinates. The same holds for the calculation of the Badhwar-Konradi pitch angle distribution. A coordinate transformation from geographical coordinates (i.e. longitude, latitude, altitude) to McIlwain's (B,L)-coordinates has to be performed. For this purpose, a geomagnetic model is employed to relate the geographic and magnetic coordinate systems. Depending on how the (B,L)-coordinates are used, different models are required [14].

For the AP-8 model, the (B,L)-coordinates have to be obtained using the Jensen and Cain 1960 [22] geomagnetic field model for AP-8 MIN and the GSFC 12/66 (updated to 1970, Cain [9]) geomagnetic field model for AP-8 MAX.

For the Badhwar-Konradi pitch angle distribution, the theoretical model itself is neutral to the choice of the geomagnetic model. However, for obtaining the coefficients p_1 to p_4 , a fit to the AP-8 omnidirectional flux spectrum is performed by Kruglanski and Heynderickx [25] using the Jensen and Cain 1960 [22] geomagnetic field model for coordinate conversion. The requirement is therefore that the same geomagnetic model be used for further calculations of the Badhwar-Konradi pitch angle distribution.

5.5 Practical Considerations and Summary

The AP-8 model is employed in this work to obtain omnidirectional proton flux predictions for the inner Van Allen belt. Care was taken to ensure that the proper magnetic field models are used for the transformation of PROBA-1 geographic coordinates to McIlwain's (B,L)-coordinates.

As the Earth's magnetic field has changed since the compilation of the AP-8 model and the generation of the geomagnetic field models, the predicted position of the SAA is not accurate (the SAA has been subject to a longitudinal drift and other modifications over the course of time). AP-8 and the coordinate conversion are therefore used with the secular drift option that takes into account the drift of the SAA in longitudinal direction. In practice, the secular drift option adjusts the geographical position of PROBA-1 during simulation. Some further improvements to the AP-8 model (better data interpolation at low altitudes) that are important for the SREM on PROBA-1 are considered in the same way as they are considered in SPENVIS.

6 Countrate Predictions

In Chapter 4, the angular response of the SREM was presented. Chapter 5 described the combination of the omnidirectional AP-8 flux model with the Badhwar-Konradi pitch angle distribution, resulting in an directional flux model. This directional flux model and the SREM response can be used to simulate and predict the countrate of the SREM.

How to join the various models and the SREM response in practice is subject of Chapter 6.

6.1 General Procedure

The SREM countrate in $\left[\frac{\#}{s}\right]$ at a specific point in space is given by the integral

$$C = \int_0^\infty \int_0^{2\pi} \int_0^\pi F(\theta, \phi, E) R(\theta, \phi, E) \sin(\theta) d\theta d\phi dE \quad (6.1)$$

The angular response function $R(\theta, \phi, E)$ in $[cm^2]$ has been determined in Chapter 7 and can be used directly in the equation above.

The directional flux F in $\left[\frac{\#}{cm^2 sr MeV s}\right]$ has been derived in Chapter 5 as a function of pitch angle and energy at a specific location, and will have to be converted to being a function of θ and ϕ , i.e. $F(\theta, \phi, E)$.

The integration of (6.1) over energy and direction can then be carried out for any location for which a countrate prediction is needed.

The required steps are:

1. Choose a location (in LEO) that the simulation should be carried out for (Section 6.1.1).
2. Evaluate the AP-8 omnidirectional flux model in this location (Section 6.1.2).
3. Determine the magnetic field (components of the magnetic field vector) in this location (Section 6.1.3).
4. Choose the attitude of the SREM instrument with respect to the magnetic field vector (Section 6.1.4). In other words, choose the pitch angle of the SREM in this location. Use the Badhwar-Konradi model to obtain the anisotropic scale factor.

5. Multiply the AP-8 omnidirectional flux \mathcal{F}_{AP8} with the anisotropic scale factor to obtain a directional flux $F(\theta, \phi, E)$ (Section 6.1.5).
6. Obtain the directional response function $R(\theta, \phi, E)$ from the GRAS/Geant4 simulation results. Choose the directional response function of the SREM instrument channel that the countrate should be obtained for (Section 6.1.6).
7. Use the directional response function and the directional flux to evaluate the integral in (6.1) and obtain a countrate (Section 6.1.7).

The details of these steps and their practical implementation and applications are discussed in the next sections. It shall be noted, however, that a countrate prediction for a single point does not guarantee a meaningful result. The AP-8 flux that is used as a basis for the predictions is a static model that can differ considerably from real fluxes at a specific location and time. After countrates have been calculated for set of points along the spacecraft trajectory, the results can be integrated and averaged.

6.1.1 Choice of Location and Location Coordinates

The location in LEO that the SREM countrate simulation should be run for is chosen. The simulation of SREM countrates is compared to actual SREM data from PROBA-1 and the simulation is therefore run along the PROBA-1 orbit. The SREM data from PROBA-1 is available in the Common Data Format (CDF, [27]) and conveniently includes the position of PROBA-1 with a sample rate of 30 s. This information of PROBA-1 position is used in this work.

The position of PROBA-1 is given in the Geocentric Equatorial Inertial (GEI) coordinate system and needs to be converted to the GDZ (altitude, latitude, East longitude) system. The ONERA-DESP library (Boscher et al. [6]) is employed for this purpose.

6.1.2 AP-8 Model Evaluation

As discussed in Chapter 5, AP-8 is a non-dynamic model of proton fluxes with two versions, AP-8 MIN and AP-8 MAX. The AP-8 model is evaluated for all positions along the PROBA-1 orbit. The AP-8 model is easily accessible through a library developed as a backend to SPENVIS [4] by Kruglanski and Heynderickx [25]. It supplies the integral AP-8 flux spectrum in units of $\frac{\#}{cm^2 s}$ for a set of McIlwain's coordinates B and L. The integral flux spectrum can be differentiated (3-point Lagrangian) to obtain the differential flux spectrum with units $\frac{\#}{cm^2 s MeV}$. The positional information from PROBA-1 (in GDZ coordinates) is converted to B,L-coordinates with the Jensen and Cain 1960 [22] magnetic field model.

6.1.3 Magnetic Field Evaluation

The directional distribution of the flux encountered by the SREM depends on the angle between SREM and magnetic field vector, i.e. the pitch angle of the SREM instrument. Since as a primary goal, the SREM simulation shall be compared with actual SREM data, the pitch angle that the SREM instrument has on PROBA-1 at a specific location in its orbit is determined.

There are two possible approaches:

1. PROBA-1 is carrying a magnetometer that measures the magnetic field components with a usual sampling rate of 0.5 Hz . The output of this magnetometer can be used to give the pitch angle of the SREM.
2. Based on the position of the PROBA-1 satellite, a magnetic field model can be employed to return the magnetic field vector given at this position by the model.

Since the use of the model introduces an additional complication and possibly larger error into the calculation, the PROBA-1 magnetometer data are used in this work. Being available for intervals of 2 s (0.5 Hz), linear interpolation is used to obtain a value between two samples.

6.1.4 SREM Attitude

The magnetic field vector is determined from PROBA-1 magnetometer data in G in spacecraft-centred, spacecraft-fixed Cartesian coordinates. In order to determine the pitch angle for the SREM, the magnetic field vector is transformed to spherical SREM coordinates θ, ϕ .

With the SREM pitch angle and McIlwain's (B,L)-coordinates as in input, the Badhwar-Konradi model is used to obtain the anisotropic scale factors.

6.1.5 Directional Flux $F(\theta, \phi, E)$

The directional flux $F(\theta, \phi, E)$ is calculated from the AP-8 omnidirectional flux \mathcal{F}_{AP8} by applying to it the anisotropic scale factors as given by the Badhwar-Konradi model.

6.1.5.1 SREM Pitch Angle and PROBA-1 Magnetometer

The directional $F(B, L, \alpha)$ flux as a function of particle pitch angle α and position in (B,L)-space has been derived:

$$F(B, L, \alpha) = \frac{\mathcal{F}_{AP8}(B, L)}{4\pi} W_{BK}(B, L, \alpha) \quad (6.2)$$

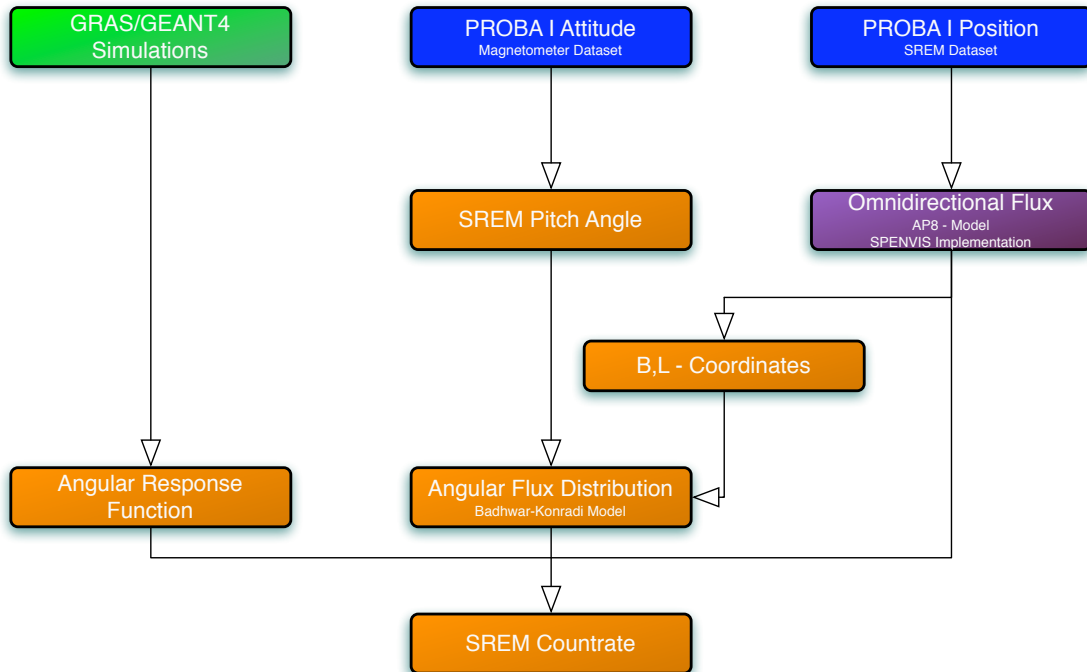


Figure 6.1: Block diagram showing the process of obtaining SREM countrate predictions. Input parameters are coloured in blue and simulation results in green. Violet colour indicates that a library implementation is used that is also employed by SPENVIS. Orange designates procedures and functions that have been implemented exclusively for this work.

In order to use this relationship in (6.1), the dependency on the pitch angle α has to be changed to a dependency on θ and ϕ , i.e.

$$F(\alpha) \rightarrow F(\theta, \phi)$$

For a looking direction $\vec{l}(\theta, \phi)$, the corresponding particle pitch angle is the angle between \vec{l} and \vec{B}

$$\cos \alpha = \frac{\vec{l} \cdot \vec{B}}{|\vec{l} \cdot \vec{B}|} \quad (6.3)$$

6.1.6 Directional Response Function $R(\theta, \phi, E)$

The response function is readily obtained from the results of Chapter 4. In practice, it can be accessed using the Interactive Data Language (IDL, [21]) procedure `angular_rfunc`

developed for this work (see Appendix D for an overview of all IDL scripts developed within the scope of this work). After calling

```
angular_rfunc,0,rfunc
```

`rfunc` holds $R_{TC1}(\theta, \phi, E)$, the response function of channel 0, i.e. *TC1*.

6.1.7 Evaluation of Integral and Countrate Calculation

Summation over all direction and numerical (trapezoidal) integration over energy is performed to obtain a simulated SREM countrate.

6.2 Example Calculation

The following is an example calculation of an SREM countrate prediction for a single location in the PROBA-1 orbit. The steps are numbered according to the general procedure outlined in Section 6.1.

1. The chosen location is at -45.00° longitude, -15.13° latitude and 592.18 km altitude, i.e. in the SAA. PROBA-1 passed it on April 19th, 2004 at 13:38:27 UTC.
2. The (B,L)-coordinates for this location are $B = 0.198$ and $L = 1.191$. For these values of B and L , the omnidirectional AP-8 MIN model gives an integral flux ($E > 10 \text{ MeV}$) of $997.8 \frac{\#}{\text{cm}^2 \text{s sr}}$.
3. The magnetometer on PROBA-1 measured the magnetic field vector (in Cartesian SREM coordinates) to be $\vec{B} = \begin{pmatrix} 0.10 & 0.18 & 0.02 \end{pmatrix}$ gauss. This corresponds to the spherical SREM coordinates of $\phi = 60.8^\circ$ and $\theta = 84.3^\circ$ for the direction of the magnetic field vector.
4. For a looking direction of $\vec{l} = \begin{pmatrix} 0 & 0 & 1 \end{pmatrix}$ (i.e. through the main instrument entrance with $\theta = 0^\circ$), the pitch angle is $\alpha = 84.3^\circ$.
5. , 6. and 7.: Multiplying the AP-8 omnidirectional flux with the anisotropic scale factor and the instrument response and then summing over all looking directions and energies predicts countrate of 246.14 counts. The measured countrate by the SREM on PROBA-1 is 173.76 counts.

6.3 Implementation

All software necessary for the countrate prediction procedure has been implemented in IDL, a language and programming environment heavily used by ESA to process data

from e.g. satellites. Since the software library providing the AP-8 model and the SREM data from PROBA-1 are both interfaced with IDL, it was natural to use IDL for all programming related to this work.

In its scope and presentation to the user, IDL resembles MATLAB as a high-level vector oriented language. However, IDL also shows similarities to FORTRAN, a programming language that had been (and still is) in wide use for computational physics purposes.

The vast amount of SREM data from PROBA-1 that had to be amalgamated into meaningful output called for the ability to use multiple processors and to address sufficient memory, something that IDL is capable of doing.

6.3.1 IDL Scripts

Figure 6.1 shows all functional elements that are required to perform countrate predictions for the SREM. Several functions and procedures (coloured in orange) were implemented in IDL for this work. Their functionality, input parameters and output are detailed in Appendix D.

7 Simulation Results

In the preceding chapters, a procedure for obtaining SREM countrate predictions has been developed and presented. The procedure shall be tested against real data from the SREM instrument on-board the PROBA-1 satellite. This allows for an estimation of the reliability, error and potential shortcomings of countrate predictions by this method.

The quality of the simulation results can be assessed under two different aspects: Firstly, whether the method is capable of reproducing short-term countrate features and secondly whether it is capable of reproducing long-term integrated countrates. The following sections will treat both aspects, starting with presenting a selected short-term feature.

7.1 April 19th, 2004: Short Term Observation

On April 19th, 2004 the PROBA-1 satellite was observing the Brazilian city of Sao Paolo as it was traversing the SAA. For the purpose of ground observation, the satellite had to be slewed to keep cameras on target. The attitude (and consequently the satellite's pitch angle) changed during this period, providing a unique insight into the pitch angle dependency of SREM countrates.

Figure 7.1, taken from Evans et al. [16], summarises the results: as the pitch angle of the SREM varied between $\approx 84^\circ$ (13:38 UTC) and $\approx 23^\circ$ (13:43 UTC), the coincidence counters (upper panel) show a clear pitch angle dependence; the decrease in pitch angle results in a decreased countrate. On the other hand, the counters *S34*, *TC2* and *TC1* (lower panel) are unaffected by the pitch angle variation.

This countrate characteristic can be reproduced using the SREM response functions and the AP-8/Badhwar-Konradi model presented in this work.

The Badhwar-Konradi distribution presented in Section 5.3 illustrates the change in flux anisotropy that the SREM was subject to during this pass of the SAA. At a pitch angle of 84° , the flux is mainly concentrated around $\theta = 0^\circ$ and 180° . For a pitch angle of 23° , the flux is concentrated loosely between an elevation of $\theta = 40^\circ$ and $\theta = 130^\circ$ (Figure 7.2).

7 Simulation Results

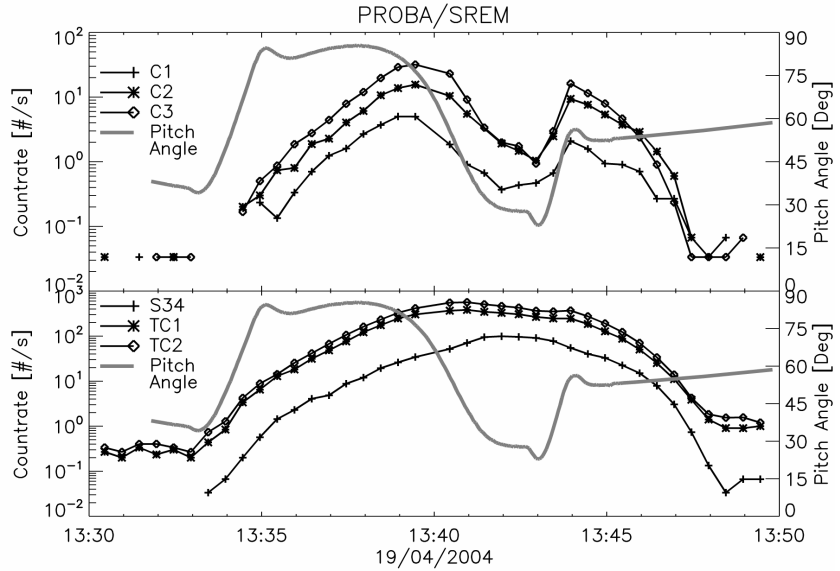


Figure 7.1: Pitch-angle dependence of SREM countrates. Taken from Evans et al. [16]

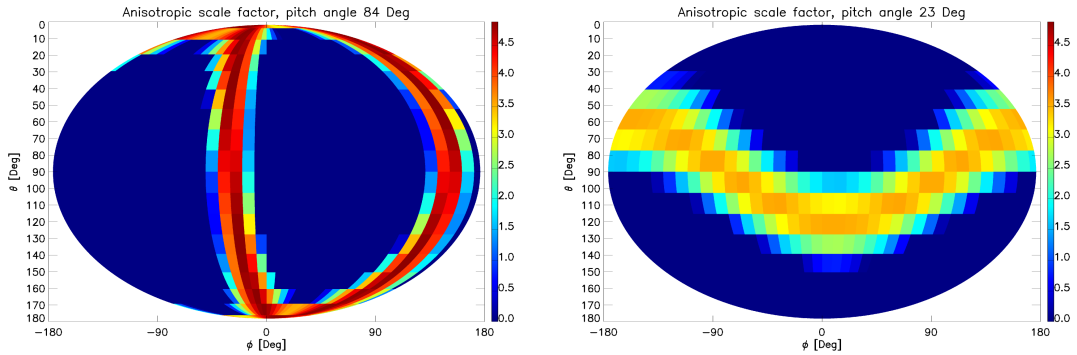


Figure 7.2: The anisotropic scale factor as given by the Badhwar-Konradi model for pitch angles of $\approx 84^\circ$ (left panel) and $\approx 23^\circ$ (right panel). The anisotropic scale factor is used to introduce anisotropy in the AP-8 model. Both panels share the same colour mapping.

Depending on the SREM channel, this change in flux direction has a different effect. Channels $TC1$, $C1$ and $C3$ shall serve as examples. Their angular response to a flat spectrum has been discussed in Section 4.1.1 and is shown in Figures 4.1 and 4.5. While $TC1$ is rather omnidirectional (i.e. receptive to flux from all directions), $C3$ requires particles to be incident either from around $\theta = 0^\circ$ or $\theta = 180^\circ$ (this is due to the fact

7 Simulation Results

that $C3$ is a coincidence counter). In particular, this means that $C3$ does not show any significant response around $\theta = 90^\circ$.

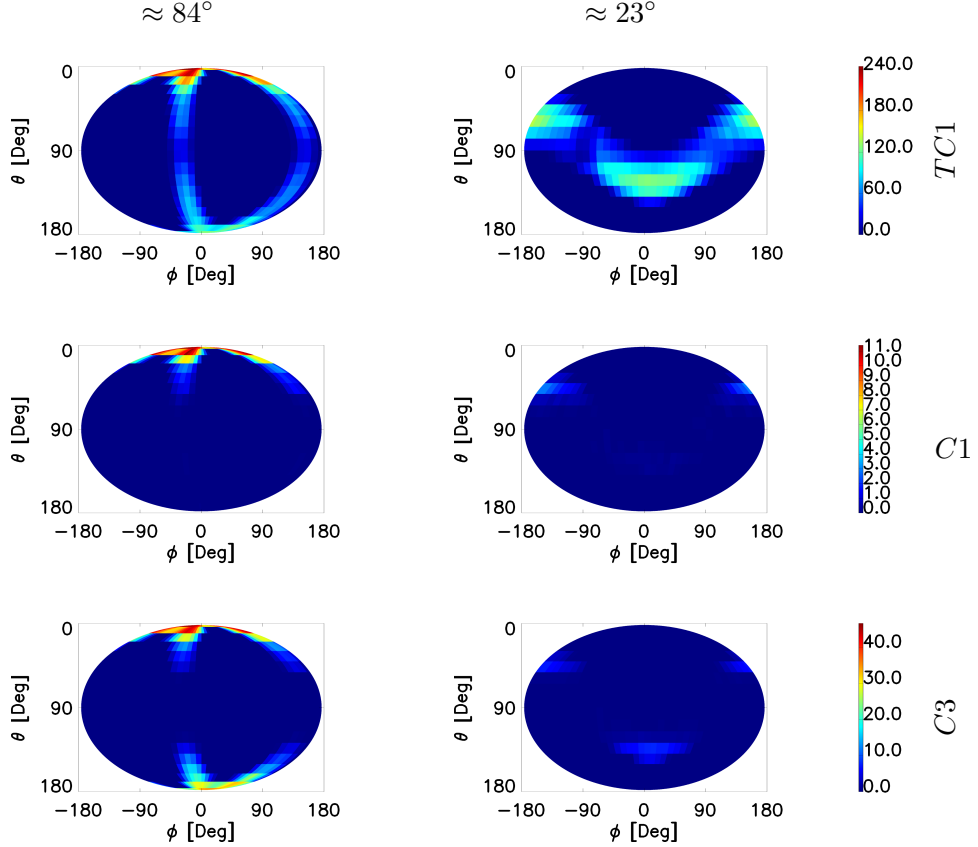


Figure 7.3: Angular countrate of channels $TC1$, $C1$ and $C3$ at pitch angles of $\approx 84^\circ$ and $\approx 23^\circ$, colour-coded in $\frac{\#}{s}$. For $\approx 23^\circ$ (right panel), $TC1$ still shows response while $C1$ and $C3$ almost fade out.

It follows that $C3$ will show a lower countrate for a pitch angle of 23° , when the flux is concentrated around $\theta = 90^\circ$. $TC1$, being omnidirectional, will be less affected than $C3$ (Figure 7.3).

Plotting countrate over time, this prediction turns out to be accurate. AP-8/Badhwar-Konradi follows and reproduces the characteristic of the observed countrate.

7 Simulation Results

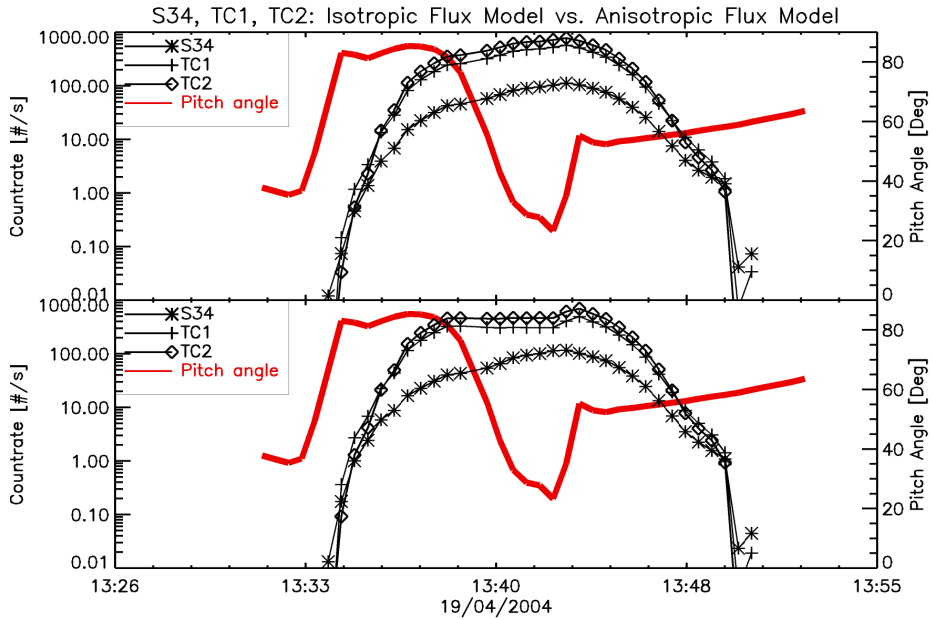


Figure 7.4: Simulated countrates of SREM channels $S34$, $TC1$, $TC2$ for a varying pitch angle. The reasonably omnidirectional nature of these channels renders them insensitive to pitch angle changes. Applying an isotropic flux model (upper panel, AP-8 MIN) and an anisotropic flux model (lower panel, AP-8 MIN/Badhwar-Konradi) yields similar countrate characteristics.

The general behaviour of countrates over time is illustrated in Figures 7.4 and 7.5. As supported by the measured data (Figure 7.1), channels $S34$, $TC1$ and $TC2$ are only slightly affected of any pitch angle-induced flux anisotropies. Their countrates follow the omnidirectional AP-8 model, and including anisotropic contributions does not greatly modify the results.

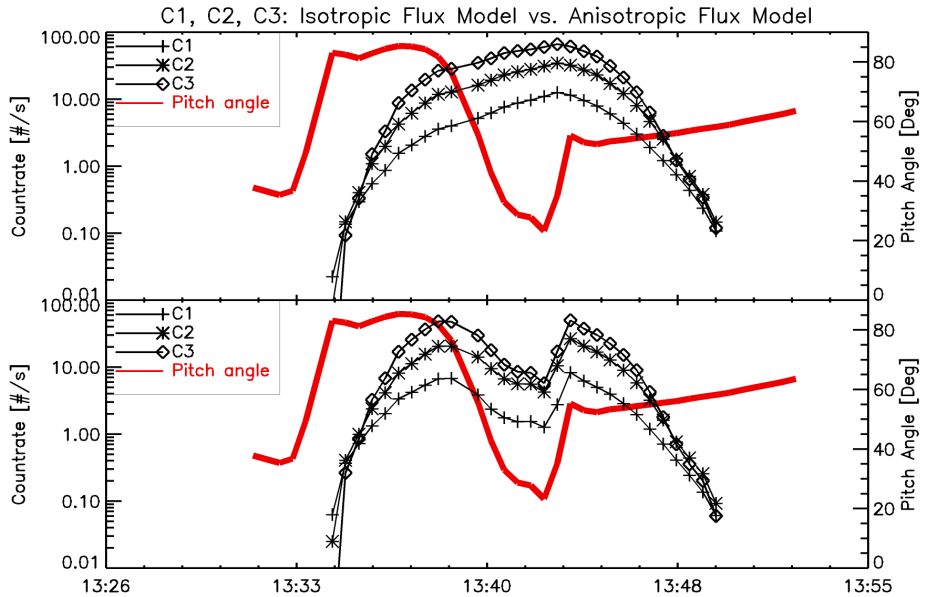


Figure 7.5: Simulated countrates of SREM channels C_3 , C_1 , C_2 under a varying pitch angle. The channels have a highly directional response and are sensitive to pitch angle anisotropies. Applying an omnidirectional flux model (upper panel, AP-8 MIN) does not reproduce the observed countrates. An anisotropic flux model (lower panel, AP-8 MIN/Badhwar-Konradi) is required to match the measured characteristics shown in Figure 7.1.

Channels C_1 , C_2 and C_3 have proved to be sensitive to flux anisotropies. The upper panel in Figure 7.5 indicates clearly the discrepancy with the AP-8 model. Only if an anisotropic scale factor as given by the Badhwar-Konradi model is introduced can the measured profile in Figure 7.1 be reproduced.

7.2 Long-Term Integrated Countrates

Short-term countrate characteristics have been shown in the previous section to be driven by flux anisotropies. An equivalent analysis for long-term countrates is possible using SREM data from PROBA-1 covering the period from 2001 to 2009.

When comparing accumulated (integrated) countrates over days, months and years, the SREM data has to be prepared accordingly. This includes the discrimination and suppression of counts other than those from protons, in particular electron contributions and counts due to cosmic rays and Solar Proton Events (SPE).

7 Simulation Results

In order to suppress cosmic rays and other background, a simple cut-off threshold for the countrate will be used; depending on the channel, countrates below $0.1 - 6 \frac{\#}{s}$ are disregarded.

7.2.1 Background Suppression

Figure 7.6 gives an overview of countrates for all 15 channels. For the period between October 29th, 2001 and March 26th, 2009, the countrate $\left[\frac{\#}{s} \right]$ is shown on the horizontal axis in histograms. A general characteristic ('knee followed by exponential decay') can be observed across all channels. The background cut-off has been chosen based on the 'knee' as this has been found to correspond to previous background estimations.

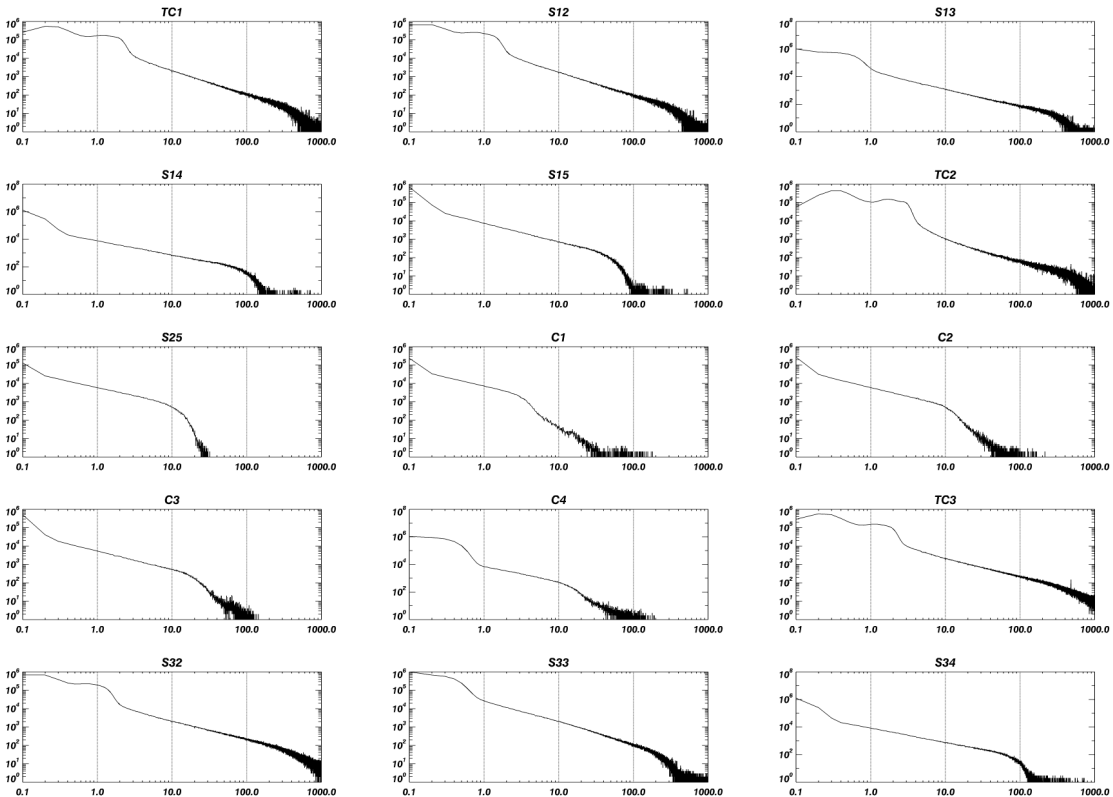


Figure 7.6: Histograms of SREM countrates used for determining background levels. The countrate on the horizontal axis is given in $\left[\frac{\#}{s} \right]$, the value in vertical direction indicates how often a specific countrate occurred in the time period between October 29th, 2001 and March 26th, 2009.

7 Simulation Results

This results in the following background thresholds (Table 7.1), given in $\frac{\#}{s}$:

Table 7.1: SREM background levels, in $\frac{\#}{s}$

TC1	S12	S13	S14	S15	TC2	S25	
4	3	1.5	0.5	0.4	6	0.25	
C1	C2	C3	C4	TC3	S32	S33	S34
0.2	0.2	0.4	1.0	3.0	2.0	0.9	0.8

7.2.2 Long-Term Pitch Angle and Flux Distribution

The short term observation of April 19th, 2004 gives a unique insight into the pitch angle dependency of SREM countrates. During one pass of the SAA, all pitch angles between $\approx 23^\circ$ and $\approx 86^\circ$ were sampled. This is not the usual situation: unless a slew manoeuvre is commanded from ground, the attitude of PROBA-1 with respect to the magnetic field during one single pass of the SAA varies less strongly.

Long-term data from between October 29th, 2001 and March 26th, 2009 is therefore used to get better sampling of the pitch angle dependence of the countrate (Figure 7.7). The figure shows the long-term countrate of channel $C2$ and simulated countrates with and without the Badhwar-Konradi pitch angle distribution.

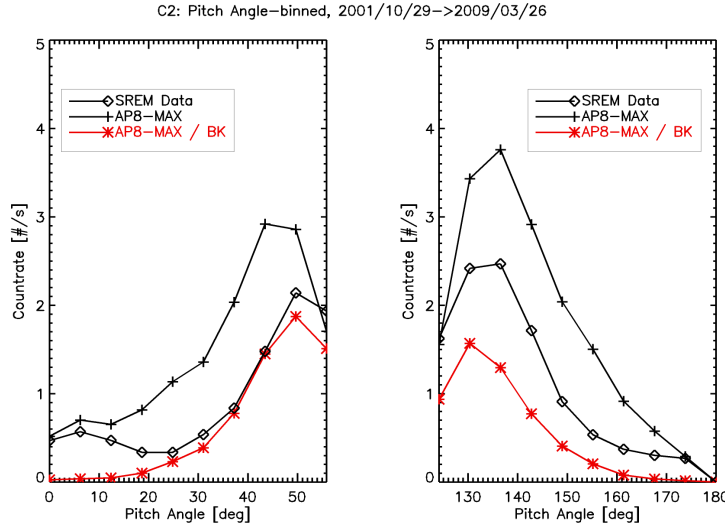


Figure 7.7: Long-term mean of the countrate (channel $C2$) as a function of the SREM pitch angle

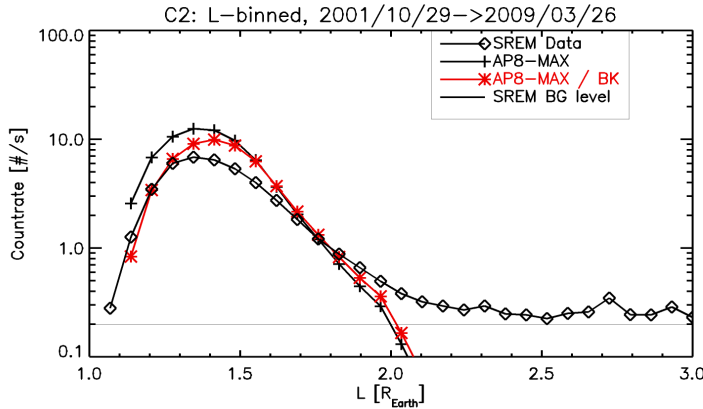


Figure 7.8: Countrate of channel C2 compared to AP-8 MAX and AP-8 MAX with a Badhwar-Konradi anisotropic scale factor

The countrate maxima occur for pitch angles between 40° and 50° (left panel in figure 7.7) and 130° and 140° (right panel in figure 7.7), when PROBA-1 passes the SAA in the North-South and South-North directions and the encountered radiation spectrum is hardest.

The effect of the directionality of the flux is clearly visible: the omnidirectional AP-8 model overestimates the countrate, including the Badhwar-Konradi model corrects for this and results in a more accurate countrate prediction for pitch angles between 40° and 50° (the range between 130° and 140° is underestimated). Due to this being a long-term observation, data taken during different solar conditions and magnetic field conditions are averaged. The achieved accuracy of countrate predictions is to be considered very good, taking into account the static nature of the underlying flux models.

A crucial conclusion in this context is that for PROBA-1, flux anisotropies do not even out in the long-term. This can be understood by considering that the satellite has a preferred attitude with respect to the magnetic field when it passes the SAA.

7.2.3 Magnetic L-Value Profile

Long-term SREM data can be used to obtain a profile of the inner Van Allen belt in terms of the L-coordinates of the magnetic field (magnetic L-value).

The L-binned long-term countrate profile of the PROBA-1 SREM is given in Figures 7.8 and 7.9. Both figures show the inner Van Allen belt with a countrate maximum at $L \approx 1.3$ Earth radii. $C2$ detected an average of $\approx 7 \frac{\#}{s}$ at the maximum while $TC2$ shows

7 Simulation Results

a countrate larger than $300 \frac{\#}{s}$, a difference that is due to the generally higher and more omnidirectional response of $TC2$.

Comparisons to both AP-8 MIN and AP-8 MAX have been carried out. In line with the short term countrate observations and the pitch angle dependency of countrates discussed in the previous section, the coincidence channel $C2$ does not show satisfactory agreement with omnidirectional AP-8 models. Both AP-8 MIN and AP-8 MAX exceed the SREM data.

The prediction can again be improved by combining AP-8 with an anisotropic scale factor. In Figure 7.8, the red graph is a combination of the AP-8 MAX model with the anisotropic scale factor as given by the Badhwar-Konradi model. For L -values < 1.3 Earth radii, it reproduces SREM data with high fidelity. For higher values of L up until $L \approx 1.7$ Earth radii, the countrate is still overestimated.

The AP-8 model and SREM data show good agreement for the reasonably omnidirectional channel $TC2$ (Figure 7.9), which is in contrast to coincidence-channel $C2$. The adjustments due to the Badhwar-Konradi model do not yield any significant difference for $TC2$.

A similarity between the countrate predictions for channel $C2$ and channel $TC2$ is the overestimation of the countrate for L -values around ≈ 1.5 Earth radii.

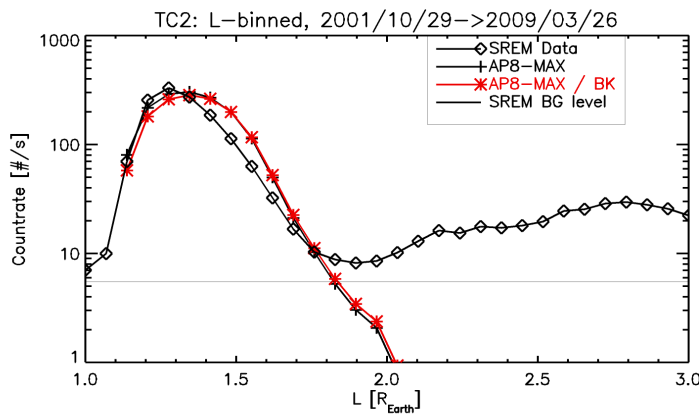


Figure 7.9: Countrate of channel $TC2$ compared to AP-8 MAX and AP-8 MAX with a Badhwar-Konradi anisotropic scale factor. Note: The $TC2$ channel is also sensitive to $> 2.8 MeV$ electrons, which is seen above $L = 2$.

8 Human Spaceflight

The previous chapter has shown the improvement that can be made to the AP-8 flux model by additionally considering a prediction of the flux anisotropy. The countrates of the SREM instrument can be simulated and reproduced much more faithfully, both their short-term characteristics and long-term integrated countrates. Consequently, the SREM instrument can be used to coarsely measure and map flux anisotropies.

8.1 Overview

Various kinds of radiation have adverse effects on the performance of spacecraft and their components. However, radiation becomes an even more crucial factor when it comes to human spaceflight. Human beings have their natural habitat on Earth, protected by both the Earth's magnetic field and the Earth's atmosphere which serve as a shield and attenuator against various types of radiation. In space, harsh radiation environments can lead to both short-term and long-term effects on a human being's health. When an energetic particle is absorbed by cellular matter in the human body, the deposited energy can lead to ionisation (molecular changes). Depending on where these changes take place, they might have no effect (the usual case), lead to physiological changes in the cell (leading to the cell's death) or cause cell mutation.

This situation is critical in long-term human outposts like the International Space Station (ISS) or in long-term space journeys like a possible future flight to Mars. It can, however, be mitigated by taking precautions in the form of spacecraft shielding, lowering health risks to an acceptable level.

The dose that an astronaut on the ISS can expect is primarily determined by the space station's orbit. Figure 8.1 shows that its orbit leads the ISS through the SAA where it encounters mainly proton radiation. This is the most significant contribution to the station's radiation budget. The second contribution is galactic radiation from cosmic rays (disregarding SPEs which are singular non-typical events). Also, during extravehicular activities ('space walks') at high latitudes, electron radiation can play a significant role (Johnson et al. [23]).

The term 'dose' refers here to the absorbed dose D which is a measure for the energy imparted to matter by ionising radiation. Different types of radiation, even when imparting

the same amount of energy, have different effects on human tissue depending on particle type and tissue type. The equivalent dose H is the absorbed dose weighted with a factor w_R accounting for particle type. The effective dose E is the equivalent dose additionally weighted with a factor w_T accounting for different types of tissues (Hajek [17]).

$$E = w_T H = w_T w_R D \quad (8.1)$$

It shall be noted that $w_R = 5$ for protons (as encountered in the SAA) while $w_R = 1$ for photonic radiation (gamma rays). This is due to the higher ionising potential of protons. Mapping the proton flux in LEO by instruments such as the SREM is therefore crucial to assessing radiation risks.

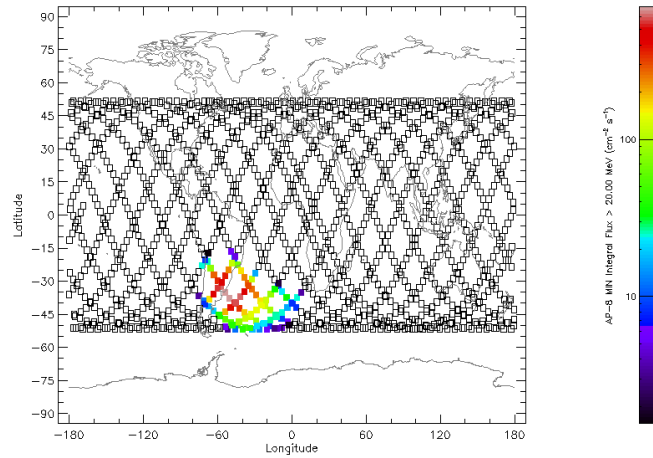


Figure 8.1: A typical trajectory of the ISS for one day with colour-coded integral proton flux. All flux contributions are due to the SAA. Figure generated with SPENVIS.

8.2 Pitch Angle Anisotropies in the ISS Orbit

The radiation environment experienced by the ISS is similar to the environment encountered by PROBA-1 and measured by the SREM. For both spacecraft, virtually all the encountered proton flux stems from SAA traversals. The importance of flux anisotropies in the SAA has been shown in previous chapters both by simulation and comparison with measured SREM data. Due to anisotropies of the flux, different modules of the ISS will encounter different fluxes. This is due to the fact that the ISS is orbit-stabilised, i.e. the ISS has a preferred attitude as it moves through the SAA. Flux anisotropies cannot even out in the long term, again similar to PROBA-1. Knowledge of flux anisotropy

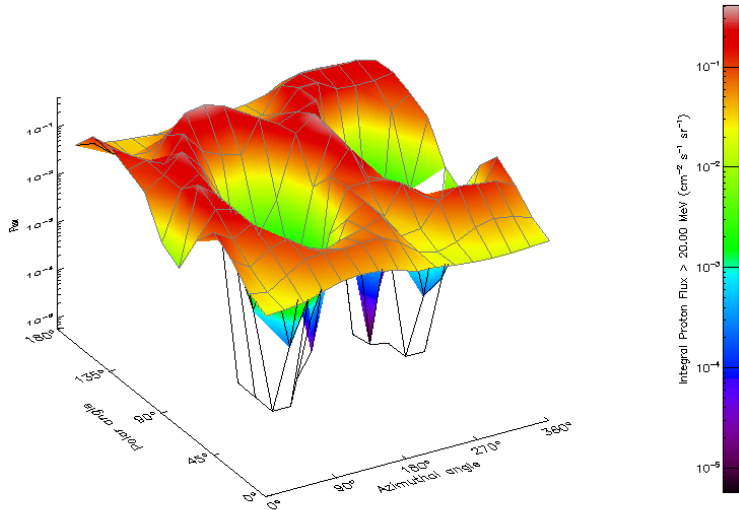


Figure 8.2: Flux anisotropy for protons with energy $E > 20 \text{ MeV}$ during a one-day ISS orbit (left panel, as generated with SPENVIS) . The polar angle is measured from the forward direction (ISS velocity vector) and the azimuth angle is measured from zenith.

characteristics is therefore critical to the protection of astronauts. Those parts of the station that statistically, over a long period of time, will encounter higher fluxes can then be equipped with additional shielding. The parts of the ISS that accommodate the crew for the most part of their stay on the station can be located strategically to minimise the flux.

Investigations of the omnidirectional and anisotropic flux for ESA's Columbus module have been carried out by Ersmark et al. [13], where a strong altitude dependence for dose rates due to protons is reported, leading to the conclusion that lower orbits are to be preferred in terms of radiation exposure.

The proton flux anisotropy for a typical ISS orbit is shown in Figure 8.2. In the direction of the magnetic field vector approximately perpendicular to both the forward and the zenith direction, no flux is to be expected (this corresponds to $\theta \approx 80^\circ$ and $\phi \approx 130^\circ / 310^\circ$, in Figure 8.2 above). The flux anisotropy within the space station, i.e. after the primary radiation passes the hull, is vastly different from the anisotropy outside the station (Ersmark et al. [13]) due to anisotropic shielding of the station. This results in the situation that dose rate estimations for the ISS based on omnidirectional fluxes yield more pessimistic values than directional models.

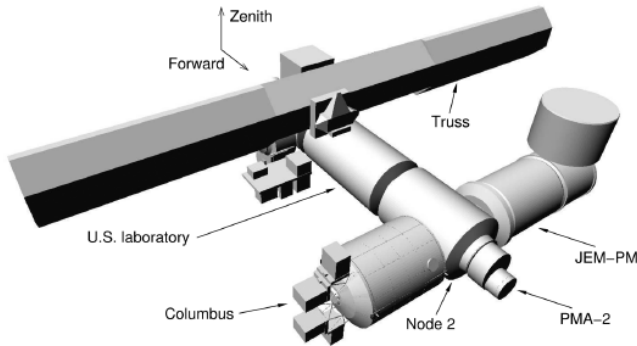


Figure 8.3: A geometric model of the ISS, taken from Ersmark et al. [13]. The polar angle is measured from the forward direction (ISS velocity vector) and the azimuth angle is measured from zenith.

As anisotropy characteristics of the proton flux play a key role in the assessment of astronaut radiation exposure and space station design, instruments like the SREM should be given a greater importance due to the valuable radiation dataset they supply. In this work, a procedure for flux estimations, taking into account the Badhwar-Konradi pitch angle distribution, has been used to estimate fluxes in the orbit of PROBA-1. This could easily be adapted to the orbit of the ISS or another future space station.

9 Conclusion

9.1 Summary

The Standard Radiation Environment Monitor is a widely applicable particle detection instrument on ESA space missions. Within the scope of this work, its response function to both protons and electrons has been obtained from GRAS/Geant4 simulations. For protons, the directional response for 648 different directions of incidence and 74 discrete energies was obtained. Likewise, for electrons, 10 discrete energies and the same 648 directions of incidence were simulated.

For the inner Van Allen belt, a combination of the AP-8 model for proton fluxes and the Badhwar-Konradi model for flux anisotropies yielded excellent approximations of SREM countrates: both long-term and short-term countrate characteristics can be reproduced or the prediction can at least be improved considerably.

A set of scripts to access the simulated SREM response function, evaluate the AP-8 flux model, obtain the Badhwar-Konradi pitch angle distribution and determine the SREM attitude using the PROBA-1 magnetometer was developed in IDL. The scripts are linked together in a procedure to predict SREM countrates.

9.2 Conclusions

The obtained directional response function of the SREM leads to a better understanding of the instrument. Knowledge of the response function is a crucial step towards deriving flux spectra from measured countrates. The directional characteristics of the different SREM channels can be used to map the pitch angle distribution of protons in the inner Van Allen Belt. By adjusting the attitude of PROBA-1 accordingly, further measurements of flux anisotropies due to the pitch angle effect should be possible and should be considered.

The geometric model of the SREM used in this thesis is sufficient for countrate predictions. Based on the simulated directional response function, both long-term and short-term countrate features can be reproduced.

9 Conclusion

This work shows the importance of considering anisotropies when comparing data with models. The AP-8 model can be extended with the Badhwar-Konradi model to yield unidirectional anisotropic flux predictions. Combined with the directional response function, the AP-8/Badhwar-Konradi model is well suited for SREM countrate predictions.

SPENVIS is an extremely useful tool for long-term integrated and omnidirectional countrate predictions. However, for point-wise countrate predictions as necessitated by the pitch angle investigation in this work, specific software scripts have to be produced.

Pitch angle anisotropies as investigated in this work have considerable relevance for human spaceflight as they give a preferred direction of flux incidence that can be shielded to mitigate risks to astronauts stemming from radiation exposure.

Obtaining the response function of a particle instrument is a crucial step towards using the instrument to its full extent. In this work, the response function and proton flux models have been used to reproduce actual SREM data. Future work on the instrument will certainly include the opposite step, i.e. deriving the actual particle flux based on measured countrates. This has to be considered as the final scientific goal of any particle instrument.

Appendix A

Badhwar-Konradi Scale Factor

A.1 Normalisation

The factor K in equation

$$F = K \left(\frac{\sin(\alpha)}{\sqrt{B}} - \frac{\sin(\alpha_L)}{\sqrt{B}} \right) e^{-\beta \left(\frac{\sin(\alpha)}{\sqrt{B}} - \frac{\sin(\alpha_L)}{\sqrt{B}} \right)} = K\xi e^{-\beta\xi}$$

shall be determined with the normalisation requirement that

$$\mathcal{F} = 4\pi \int_0^{\frac{\pi}{2}} F \sin(\alpha) d\alpha$$

Therefore

$$\mathcal{F} = 4\pi \int_0^{\frac{\pi}{2}} K\xi e^{-\beta\xi} \sin(\alpha) d\alpha = K \left(4\pi \int_0^{\frac{\pi}{2}} \xi e^{-\beta\xi} \sin(\alpha) d\alpha \right)$$

which can be solved for K :

$$K = \frac{\mathcal{F}}{4\pi \int_0^{\pi/2} \xi e^{-\beta\xi} d\cos(\alpha)}$$

Appendix B

Modifications to Geometric Model

The original geometry file (in GDML format) `srem_v02.gdml` was modified in four steps, outlined in the following sections B.1 to B.4:

B.1 Removing Electronics and Parts of the Structure

The physical volumes bearing the following names were removed/commented:

```
PSP20x92a4370 DEEL0x92a4318 DEP50x92a42c0 DEP10x92a4268 DEPL0x92a4210 DEMA0x92a41b8
AEC00x92a4160 AEFY0x92a4108 AEFY0x92a4108 AEFX0x92a40b0 AEFX0x92a40b0 AEEL0x92a4058
AEPL0x92a4000 AEP20x92a3fa8 AEP30x92a3f50 AEMA0x92a3ef8 FEC00x92a3ea0 FEC00x92a3ea0
FEC00x92a3ea0 FEFY0x92a3e48 FEFY0x92a3e48 FEFY0x92a3e48 FEFY0x92a3e48 FEFY0x92a3e48
FEFY0x92a3e48 FEFX0x92a3df0 FEFX0x92a3df0 FEFX0x92a3df0 FEFX0x92a3df0 FEFX0x92a3df0
FEFX0x92a3df0 FEEL0x92a3d98 FEEL0x92a3d98 FEEL0x92a3d98 FEEL0x92a3d98 HM270x92a3d40
HM220x92a3be0 HM210x92a3b88 HM140x92a3b30 HM130x92a3ad8 HM130x92a3ad8 HM120x92a3870
HM110x92a3818 HM110x92a3818 HM100x92a37c0 HM100x92a37c0 HM100x92a37c0 HM100x92a37c0
HM090x92a3768 HM090x92a3768 HM080x92a3710 HM080x92a3710 HM070x92a36b8 HM070x92a36b8
HM060x92a3660 HM060x92a3660 HM060x92a3660 HM060x92a3660 HM040x92a3608 HM040x92a3608
HM030x92a35b0 HM030x92a35b0 COV70x92a2b60 COV70x92a2b60 COV60x92a2b08 COV60x92a2b08
COV60x92a2b08 COV50x92a2ab0 COV40x92a2a58 COV40x92a2a58 COV30x92a2a00 COV20x92a29a8
COV20x92a29a8 COV10x92a2950 BC070x92a28f8 BC060x92a28a0 BC050x92a2848 BC040x92a27f0
BC030x92a2798 BC030x92a2798 BC020x92a2740 BC020x92a2740
```

B.2 Adjusting Cover Plates

In order to adjust the side covers, the following statements

```
<position name="HM010x92cff88inSBAL0x92a9078p"
    unit="mm" x="-133.5999999999999" y="-60" z="44.749999000000003" />
<position name="HM010x92cff48inSBAL0x92a9078p"
    unit="mm" x="-133.5999999999999" y="60" z="44.749999000000003" />
<box aunit="radian" lunit="mm" name="HM010x92b6c98"
    x="191.800004" y="2" z="88.500004000000004" />
```

were replaced by

```
<position name="HM010x92cff88inSBAL0x92a9078p"
    unit="mm" x="-52.35" y="-60" z="44.749999000000003" />
<position name="HM010x92cff48inSBAL0x92a9078p"
    unit="mm" x="-52.35" y="60" z="44.749999000000003" />
<box aunit="radian" lunit="mm" name="HM010x92b6c98"
    x="28.5" y="2" z="88.50000400000004" />
```

For the bottom cover, the following statements

```
<position name="BC010x92cecc0inSBAL0x92a9078p" unit="mm" x="-120.95" y="0" z="1" />
<box aunit="radian" lunit="mm" name="BC010x92b4cc0"
    x="212.8999999999998" y="117.5" z="2" />
```

were replaced by

```
<position name="BC010x92cecc0inSBAL0x92a9078p" unit="mm" x="-35" y="0" z="1" />
<box aunit="radian" lunit="mm" name="BC010x92b4cc0" x="60" y="117.5" z="2" />
```

B.3 Adding Aluminium Shielding

A 1 cm aluminium shield was defined

```
<box aunit="radian" lunit="mm" name="SBOX_____" x="10" y="117.5" z="88.6" />+
```

and positioned to model the parts of the instrument that had been taken away on the back:

```
<position name="SPOS_____inSBAL0x92a9078p" unit="mm" x="-60.8" y="0" z="46.975" />+
<physvol>
    <volumeref ref="SHIELD_____"/>
    <positionref ref="SPOS_____inSBAL0x92a9078p"/>
</physvol>

<volume name="SHIELD_____">
    <materialref ref="ALUMINUM0x92a55c0"/>
    <solidref ref="SBOX_____"/>
</volume>
```

B.4 Adjusting the Origin

```
<position name="SBAL0x92ceae8inMARS0x92a8e88p"
    unit="mm" x="33" y="0" z="-75.99999000000003" />
```

Appendix B Modifications to Geometric Model

for `srem_v02_final.gdml` adjusted to position the origin between the detectors $D1$ and $D2$:

```
<position name="SBAL0x92ceae8inMARS0x92a8e88p"  
        unit="mm" x="33" y="-30" z="-70.599999000000003" />
```

for `srem_v02_final_d1.gdml` adjusted to position the origin in the detectors $D1$:

```
<position name="SBAL0x92ceae8inMARS0x92a8e88p"  
        unit="mm" x="33" y="-30" z="-73.4373" />
```

for `srem_v02_final.gdml` adjusted to position the origin in detectors $D3$:

```
<position name="SBAL0x92ceae8inMARS0x92a8e88p"  
        unit="mm" x="33" y="30" z="-78.5527" />
```

Appendix C

Details of Source Setup and Normalisation

C.1 Directional Derivatives

The orientation of the circular plane used in the source geometry is set by two direction vectors lying in the plane. The direction vectors can be obtained from the position vector of the circular plane centre by building the directional derivatives.

The position vector of the centre of the circular plane is:

$$\vec{c} = \begin{pmatrix} \sin(\theta) \cos(\phi) \\ \sin(\theta) \sin(\phi) \\ \cos(\theta) \end{pmatrix}$$

The directional derivatives $\overrightarrow{rot1}$ and $\overrightarrow{rot2}$ are obtained by differentiation with respect to θ ($\overrightarrow{rot1}$) and ϕ ($\overrightarrow{rot2}$) and subsequent normalisation:

$$\overrightarrow{rot1} = \frac{d\vec{c}}{d\theta} = \begin{pmatrix} \cos(\theta) \cos(\phi) \\ \cos(\theta) \sin(\phi) \\ -\sin(\theta) \end{pmatrix}$$

$$\overrightarrow{rot2} = \frac{d\vec{c}}{d\phi} = \begin{pmatrix} -\sin(\phi) \\ \cos(\phi) \\ 0 \end{pmatrix}$$

$\overrightarrow{rot1}$ and $\overrightarrow{rot2}$ are used as input to the General Particle Source.

C.2 Flux Normalisation of a Circular Planar Source

A number of primary particles N_i is generated in a circular plane in order to simulate the response of the SREM instrument in a specific direction. The flux F_i that corresponds to this number N_i shall be derived. This flux is not a physical flux, it is only part of the GRAS/Geant4 simulation.

The unit of flux F_i is $\left[\frac{\#}{cm^2 sr}\right]$ ¹ while N_i has units $\#$. In terms of units, the flux normalisation is a conversion

$$\left[\#\right] \rightarrow \left[\frac{\#}{cm^2 sr}\right]$$

and consists of two steps:

1. A circular planar source has radius r and an area πr^2 . The number of particles per cm^2 from the circular plane is therefore $\frac{N_i}{\pi r^2} \left[\frac{\#}{cm^2}\right]$.
2. A single circular plane is a unidirectional source, i.e. it covers only one direction of 648 overall directions. The overall 648 planar sources are not distributed equally around the SREM. Due to the method chosen for dividing the spherical angle in 648 elements of $10^\circ \times 10^\circ$, the circular planes lie more densely towards the poles of the sphere. As a consequence, the simulated particle flux per unit solid angle (sr) is higher towards the poles, something that has to be taken into account when calculating the flux F_i . F_i has to be scaled with a factor δs_i [sr] corresponding to the solid angle of each $10^\circ \times 10^\circ$ element.

$$\delta s_i = \iint_{s_i} \sin(\theta) d\theta d\phi$$

Including the solid angle δs_i also introduces the unit [sr] into the normalisation. The centre of each $10^\circ \times 10^\circ$ element is given by $\theta = (10i + 5)^\circ$ and $\phi = (10j + 5)^\circ$, with $i = 0, \dots, 17$ and $j = -18, \dots, 17$.

Combining the two normalisation steps, the flux per cm^2 and per sr therefore is:

$$F_i = N_i \frac{1}{\pi r^2} \frac{1}{\delta s_i} \left[\frac{\#}{cm^2 sr}\right]$$

¹The complete unit is $\left[\frac{\#}{cm^2 sr s Mev}\right]$. Energy and time dependence can be disregarded when treating the geometric aspects of the source.

Appendix D

IDL Scripts

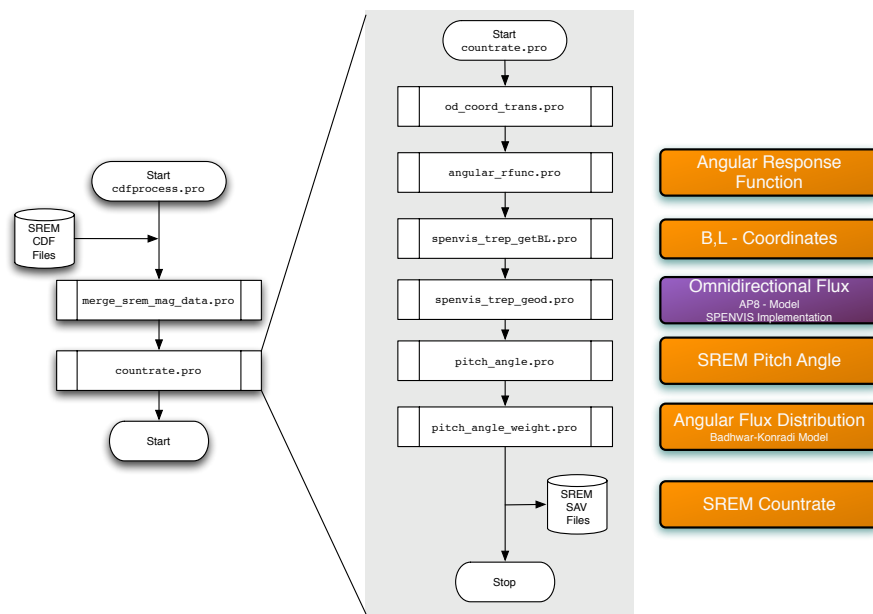


Figure D.1: Flow chart of the countrate calculation procedure implemented in IDL. The procedure predicts SREM countrates based on the directional response function, the SREM location and attitude, and proton flux models. The rightmost column indicates the correspondence between IDL scripts (.pro) and elements of the conceptual flow chart presented in Figure 6.1.

D.1 IDL Script Headers

```
;+
; NAME:
;      CDFPROCESS
```

```
;  
; PURPOSE:  
;     Calculate SREM countrate predictions. CDFPROCESS serves as a wrapper  
;     script and calls READ_CDF to read an SREM cdf-file, MERGE_SREM_MAG  
;     to include PROBA-1 magnetometer data and COUNTRATE_F to calculate  
;     the predicted countrates.  
;  
;     CDFPROCESS can be multithreaded using MULTITHREAD.  
;  
; AUTHOR:  
;     Martin Siegl, ESTEC/TEC-EES  
;     martin.siegl@esa.int  
;     siegl@sbg.at (permanent)  
;  
; CALLING SEQUENCE:  
;     CDFPROCESS, filesearchlist  
;  
; INPUT PARAMETERS:  
;     filesearchlist:  
;         An array returned by FILE_SEARCH containing the pure filenames  
;         (no path) of the sav-files to be processed.  
;  
; INPUT KEYWORD PARAMETERS:  
;     N/A  
;  
; MODIFICATION HISTORY:  
;     2009-06-01: First documented version  
;  
;  
;+  
; NAME:  
;     MERGE_SREM_MAG  
;  
; PURPOSE:  
;     Merge SREM dataset with PROBA magnetometer dataset. For each recorded  
;     SREM datapoint in the structure srem_data, retrieve the magnetometer  
;     reading from the structure mag_data and put it together in the structure  
;     srem_data_mag.  
;     Linear interpolation is performed on the magnetometer data if necessary.  
;  
; AUTHOR:  
;     Martin Siegl, ESTEC/TEC-EES  
;     martin.siegl@esa.int  
;     siegl@sbg.at (permanent)  
;  
; CALLING SEQUENCE:
```

```
; MERGE_SREM_MAG, srem_data, mag_data, srem_data_mag, sim_data_mag
;
; INPUT PARAMETERS:
;   srem_data:
;     comes from the SREM cdf files
;
;   mag_data:
;     comes from the PROBA magnetometer
;
;   srem_data_mag:
;     merges both datasets
;
;     sim_data_mag is a copy of srem_data_mag with an additional countrate_sim field,
;     pitch angle field and field for B,L coordinates
;
; INPUT KEYWORD PARAMETERS:
;   N/A
;
; MODIFICATION HISTORY:
;   2009-04-21: First documented version
;
;+
; NAME:
;   COUNTRATE_F
;
; PURPOSE:
;   Predict the countrate of one channel of the SREM instrument
;   at a specific orbital position given the S/C attitude, the pitch
;   angle and the AP8-flux at this position and considering the SREM
;   detector response.
;   COUNTRATE_F has a subset of the functionality of COUNTRATE.
;   COUNTRATE_F is a 'fast' version of COUNTRATE optimised for speed.
;
; AUTHOR:
;   Martin Siegl, ESTEC/TEC-EES
;   martin.siegl@esa.int
;   siegl@sbg.at (permanent)
;
; CALLING SEQUENCE:
;
;   COUNTRATE,sim_data_mag[,solar_model=solar_model]
;
;
; INPUT PARAMETERS:
;
```

```
;      sim_data_mag:  
;      comes from MERGE_SREM_MAG  
;  
;  
; RETURN VALUE:  
;  
; INPUT KEYWORD PARAMETERS:  
;      N/A  
;  
; MODIFICATION HISTORY:  
;      2009-05-01: First documented version  
;  
;+  
; NAME:  
;      PITCH_ANGLE_WEIGHT  
;  
; PURPOSE:  
;      Calculates the Badhwar-Konradi pitch angle distribution  
;  
; AUTHOR:  
;      Martin Siegl, ESTEC/TEC-EES  
;      martin.siegl@esa.int  
;      siegl@sbg.at (permanent)  
;  
; CALLING SEQUENCE:  
;  
;      PITCH_ANGLE_WEIGHT, alpha, Bc, Lc  
;  
; INPUT PARAMETERS:  
;      alpha:  
;      pitch angle in radians (scalar or vector)  
;  
;      Bc:  
;      McIlwain's B coordinate  
;  
;      Lc:  
;      McIlwain's L coordinate  
;  
;  
; RETURN VALUE:  
;      The normalised weight of the pitch angle, i.e. the anisotropic  
;      scaling factor that is to be multiplied with the Ax8 omnidirectional  
;      flux.  
;  
; INPUT KEYWORD PARAMETERS:  
;
```

```
;  
; MODIFICATION HISTORY:  
;  
;  
;+  
; NAME:  
;      PITCH_ANGLE  
;  
;PURPOSE:  
;  
;      PITCH_ANGLE returns the angle (in radians) between an instrument  
;      looking direction theta, phi and the magnetic field vector.  
;  
; AUTHOR:  
;      Martin Siegl, ESTEC/TEC-EES  
;      martin.siegl@esa.int  
;      siegl@sbg.at (permanent)  
;  
; CALLING SEQUENCE:  
;  
;      pitch_angle,theta,phi,b_srem  
;      returns the pitch_angle (angle between direction theta, phi and the  
;      magnetic field vector)  
;  
; INPUT PARAMETERS:  
;      theta, phi:  
;      Spherical coordinates for the direction that the pitch angle should be  
;      obtained for.  
;  
;      b_srem  
;      Magnetic field vector in Cartesian coordinates, in the SREM coordinate  
;      system. Can (but does not have to) be a unit vector giving the direction  
;      of the magnetic field vector.  
;  
; RETURN VALUE:  
;      The pitch angle, i.e. the angle between the looking direction theta, phi  
;      and the magnetic field field vector b_srem.  
;  
;  
; INPUT KEYWORD PARAMETERS:  
;      N/A  
;  
; MODIFICATION HISTORY:  
;
```

D.2 Data Structures

The SREM data from PROBA-1 is available in CDF-files McCuire [27] and is read into IDL using the `read_cdf\end` procedure, yielding the following data structure below. The fields marked bold were added within the scope of this work.

```
IDL> help,sim_data_mag,/struct
** Structure <793bd8>, 24 tags, length=920, data length=898, refs=1:
    EPOCH          DOUBLE      6.3249590e+13
    LABEL_COUNTERS BYTE       Array[3, 15]
    COUNTRATE      DOUBLE      Array[15]
    LABEL_ORBIT    BYTE       Array[6, 3]
    ORBIT          DOUBLE      Array[3]
    LABEL_MAGFIELD BYTE       Array[7, 3]
    MAGFIELD       DOUBLE      Array[3]
    LSHELL         DOUBLE      3.2216192
    FITQUAL        INT        1
    LABEL_PROTPARAM BYTE      Array[40, 3]
    PROTPARAM      DOUBLE      Array[3]
    PROTPARERR     DOUBLE      Array[3]
    LABEL_ELECPARAM BYTE      Array[40, 3]
    ELECPARAM      DOUBLE      Array[3]
    ELECPARERR     DOUBLE      Array[3]

    JDAY           DOUBLE      2453114.9
    B_VEC          FLOAT       Array[3]
    B_TOT          FLOAT       0.273811
    JD_OFFSET      FLOAT       0.00000
    PITCH_ANGLE    DOUBLE      1.1744113
    COUNTRATE_SIM  DOUBLE      Array[15]
    COUNTRATE_SIM_OMNI
                    DOUBLE      Array[15]
    BC             DOUBLE      0.28705211
    LC             DOUBLE      3.2552940
```

`JDAY`] is the Julian day, calculated from `EPOCH`

`B_VEC` and `B_TOT` are the \vec{B} -vector and its magnitude, respectively. The values are taken from the PROBA-1 magnetometer.

`PITCH_ANGLE` is the pitch angle of the SREM, i.e. the angle between magnetic field vector and SREM z -axis.

`COUNTRATE_SIM` and `COUNTRATE_SIM_OMNI` are the simulated SREM countrates with and without the Badhwar-Konradi anisotropic scale factor, respectively.

`BC` and `LC` are the (B,L)-coordinates as given by the applicable geomagnetic field model.

Appendix E

List of Plotted Figures Accessing Response Functions

All figures in this thesis report showing response functions, directional countrates or long-term data analysis can be conveniently reproduced using IDL scripts (procedures) developed within the scope of this work. The required commands are detailed in the following table.

Table E.1: Commands (procedure calls) for reproducing plots of response functions, directional countrates and data analysis shown in this work.

Figure	Procedure Call
4.3	<code>response_plot,[1,2,3,4],[50,75,100,150]</code>
4.1	<code>response_plot,[0,5,11],[50,75,100,150]</code>
4.7	<code>response_plot_thesis,[6],[50,75,100,150]</code> <code>response_plot_thesis,[12],[50,75,100,150]</code> <code>response_plot_thesis,[13],[50,75,100,150]</code> <code>response_plot_thesis,[14],[50,75,100,150]</code>
4.5	<code>response_plot,[7,8,9,10],[50,75,100,150]</code>
4.11	<code>response_plot,[11],[0.7,1,5,10],particle='electron_d3'</code>

Appendix F

Paper Accepted for RADECS2009

The results of this thesis work were submitted to the ‘10th European Conference on Radiation Effects on Components and Systems’ (RADECS 2009) in the category ‘Late News’. The paper was accepted for publication and presentation at the conference as abstract 1266.

The extended abstract of M. Siegl, H.D.R. Evans, E.J. Daly, G. Santin, P. Nieminen, P. Bühler: ‘Inner Belt Anisotropy Investigations Based on the Standard Radiation Environment Monitor (SREM)’ is included in the next pages.

Inner Belt Anisotropy Investigations Based on the Standard Radiation Environment Monitor (SREM)

M. Siegl, H.D.R. Evans, E.J. Daly, G. Santin, P. Nieminen, P. Bühlner

Abstract—The Standard Radiation Environment Monitor (SREM) is a particle detector developed for wide use on ESA spacecraft. It is flying on several ESA missions, most recently the HERSCHEL and PLANCK space telescopes. Using data from the SREM unit on PROBA-1 in LEO, pitch angle anisotropies in the inner Van Allen belt are investigated.

The sensitivity of the SREM to pitch angle induced flux anisotropies can be linked to the directional response function of the SREM, obtained using GRAS/Geant4 Monte-Carlo simulations. The directional response function is combined with an anisotropic version of the AP8 model (based on the Badhwar-Konradi anisotropy distribution) to yield improved count predictions. The importance of considering flux anisotropies is shown for both short-term data and long-term integrated counts. Significant improvements to the AP8 model can be realised.

Index Terms—Anisotropy, AP8, Inner Belt, SREM

I. INTRODUCTION

THE Standard Radiation Environment Monitor (SREM) [1] was developed to equip various spacecraft with the same radiation detection instrument. This allows for a standardised comparison between radiation spectra in different Earth orbits as well as in interplanetary space. Currently, an SREM instrument is part of the ESA spacecraft PROBA-1, INTEGRAL, Rosetta, GIOVE-B and the recently launched HERSCHEL and PLANCK observatories. Aside from mapping particle environments, the SREM also serves the purpose of issuing dose warnings if predefined thresholds are exceeded.

It is known that the inner belt fluxes have strong directionality depending on altitude and energy, with the anisotropy being greater at lower altitude and higher energy. This effect is important to consider in cases where a spacecraft has on average a preferred altitude with respect to the magnetic field (e.g. the ISS).

II. SREM INSTRUMENT

Fig. 1 shows the SREM instrument, a single box of 2.6 kg and dimensions of $20 \times 12 \times 10\text{ cm}^3$. Three solid state detectors (silicon PIN-diodes) measure the energy deposited by charged particles. These diodes (D_1 , D_2 , D_3) are arranged as follows: D_3 is a single diode for detection of both protons and electrons. D_1 and D_2 are two single diodes combined together in a telescope configuration. D_1 and D_2 can therefore be used separately or in a coincidence mode, where a particle

is required to deposit energy in both of them simultaneously. D_1 and D_2 are separated by a double-layer of aluminium and tantalum with respective thicknesses of 1.7 and 0.7 mm . This defines a proton energy cut-off of $\approx 43\text{ MeV}$ for coincidence detections.

The D_1/D_2 and D_3 main detector entrances have opening angles of 20° and are covered with 2 mm and 0.7 mm of aluminium, respectively, setting an overall detector cut-off energy of $\approx 0.5\text{ MeV}$ for electrons and $\approx 10\text{ MeV}$ for protons for the D_3 detector.



Figure 1. Picture of SREM flight model

For the study of inner-belt anisotropies, the SREM on PROBA-1 in a sun-synchronous orbit is chosen.

A. SREM channels

A particle depositing energy in one of the silicon diodes is registered in one or several of 15 channels (Table I), depending on the amount of deposited energy and which silicon diode(s) it was deposited in.

B. Detector Simulation Setup and Coordinate System

Fig. 2 details the simulation setup of the detectors D_3 (single) and D_1/D_2 (telescope configuration). The spherical coordinate system used in this article to indicate incident particle direction is shown.

III. SREM SENSITIVITY TO PITCH ANGLE

The 15 channels of the SREM instrument cover different energy ranges and a dependency on the pitch angle of the SREM can be observed, *i.e.* a dependency on the angle between the main entrance of SREM and the magnetic field vector.

Manuscript received June 5, 2009.

M. Siegl (corresponding author), H.D.R. Evans, E.J. Daly, G. Santin and P. Nieminen are with ESA TEC-EES. Address: European Space Agency, ESTEC, Postbus 299, Noordwijk, 2200 AG, The Netherlands. E-mail address of the corresponding author: martin.siegl@esa.int (Martin Siegl).

P. Bühlner, Auhofstrasse 22/3, 1130 Vienna, Austria.

Counter	Detector	Energy deposition discrimination levels [MeV]	Proton energy[MeV]	
			Min	Max
TC1	D1	0.085 – ∞	27	∞
S12	D1	0.25 – ∞	26	∞
S13	D1	0.6 – ∞	27	∞
S14	D1	2.0 – ∞	24	542
S15	D1	3.0 – ∞	23	434
TC2	D2	0.085 – ∞	49	∞
S25	D2	9.0 – ∞	48	270
C1	D1 & D2	0.6 – ∞ & 2.0 – ∞	43	86
C2	D1 & D2	0.6 – ∞ & 1.1 – 2.0	52	278
C3	D1 & D2	0.6 – ∞ & 0.6 – 1.1	76	450
C4	D1 & D2	0.085 – 0.6 & 0.085 – 0.6	164	∞
TC3	D3	0.085 – ∞	12	∞
S32	D3	0.25 – ∞	12	∞
S33	D3	0.75 – ∞	12	∞
S34	D3	2.0 – ∞	12	∞

Table I
SREM ENERGY DEPOSITION DISCRIMINATION LEVELS AND DETECTED PROTON ENERGY RANGE

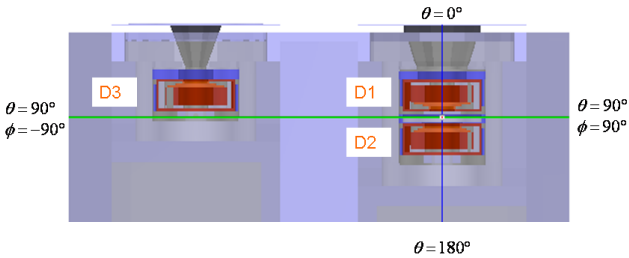


Figure 2. SREM detector setup and spherical coordinate system with azimuth angle ϕ and elevation angle θ

Fig. 3 indicates this dependency: During a traversal of the SAA on April 19th, 2004, the pitch angle of the SREM varied between $\approx 84^\circ$ (13:38 UTC) and $\approx 23^\circ$ (13:43 UTC) due to a spacecraft pointing activity. The coincidence channels (upper panel) show a clear pitch angle dependence; the decrease in pitch angle results in a decreased countrate. On the other

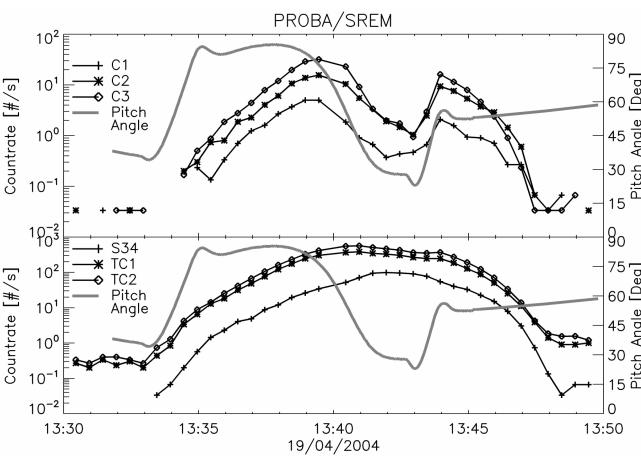


Figure 3. Pitch-angle dependence of measured PROBA/SREM countrates. Taken from [2]

hand, the channels $S34$, $TC2$ and $TC1$ (lower panel) are largely unaffected by the pitch-angle variation. The difference between the channels can be explained by investigating their directional response functions.

IV. SREM RESPONSE SIMULATION

The SREM response function has been determined in GRAS ([3])/Geant4 ([4], [5]) simulations. In these simulations, a geometric model of the relevant SREM parts (complete detector assembly including full shielding, without electronics) was irradiated with protons of between 10 MeV and 500 MeV . An instrument response with an angular resolution of $10^\circ \times 10^\circ$ was obtained. This allows for a detailed investigation of the channel characteristics in terms of their response to protons of various energies incident from different directions.

The coincidence channels require a particle to deposit energy both in diodes $D1$ and $D2$. Consequently, only primary particles that result in the deposition of energy in both detector masses are counted. Channels $TC1$ and $TC2$, however, are susceptible to radiation over a wide energy band and respond also to particles incident from flat angles (Fig. 4).

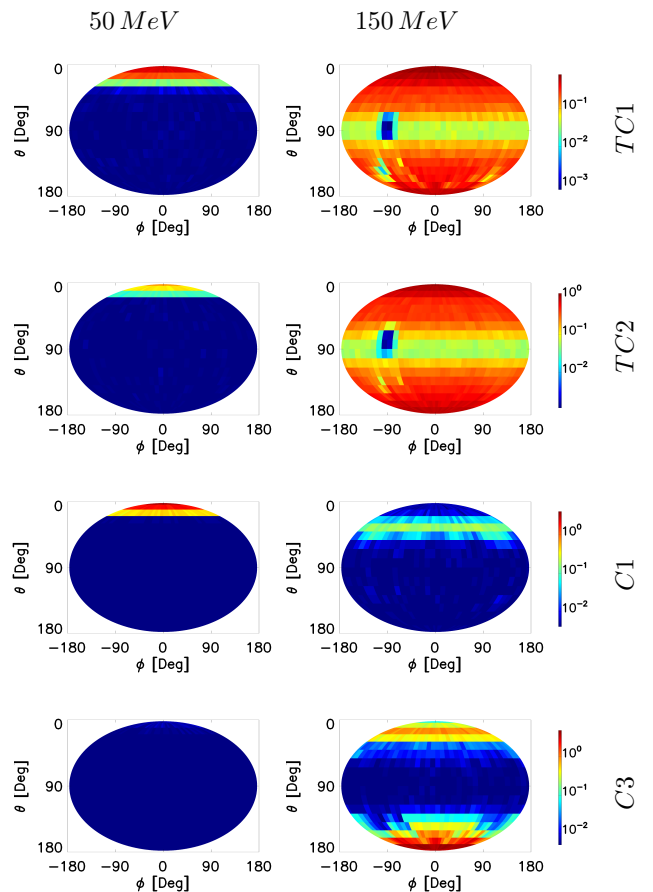


Figure 4. SREM directional response for monoenergetic protons of 50 MeV and 150 MeV . The colour-coded response is in units of cm^2 . The colour mapping is kept identical for every channel (row) to allow for comparison. From an energy of $\approx 100\text{ MeV}$ upwards, channels $TC1$ and $TC2$ show an omnidirectional response while coincidence channels $C1$ and $C3$ retain their directional characteristics. Note for channels $TC1$ and $TC2$ the shielding at $\phi = -90^\circ$ stemming from detector $D3$.

The characteristic of SREM channels to show different response to the same particle spectrum, depending on their direction of incidence, can be used to measure the anisotropy of the particle environment.

TC1 is a reasonably omnidirectional channel for high energy ranges. It can therefore be used together with an omnidirectional flux model to obtain reasonable countrate predictions when the spectrum is hard. However, the coincidence channels *C1* to *C4* require the use of a directional flux model that provides anisotropies in order to compare with countrates.

V. SREM COUNTRATE PREDICTIONS

The pitch angle dependence of the countrate can be predicted using a combination of the AP8 omnidirectional flux model [6] and the Badhwar-Konradi model [7] for flux anisotropy. The AP8 model is a static omnidirectional model of the inner-belt proton flux and does not provide directional fluxes. The main contributions to flux anisotropies in the inner belt are pitch angle anisotropy due to the particles mirroring and the East-West effect [8] due to atmospheric absorption of particles.

Given the strong directional response of the coincidence channels, an anisotropy model is required to simulate their response more accurately. Various models for pitch angle anisotropies have been proposed, such as the Heckmann-Nakano [9] and the Badhwar-Konradi models [7].

The Badhwar-Konradi model is employed in this work due to its general applicability whereas the Heckmann-Nakano model is based on the atmospheric scale height. For SREM pitch angles of $\approx 84^\circ$ (13:38 UTC) and $\approx 23^\circ$ (13:43 UTC) on April 19th, 2004, the Badhwar-Konradi model gives anisotropic scale factors (Fig. 5) that are used to convert the omnidirectional AP8 flux into an anisotropic flux.

Folding the anisotropic flux from the AP8/Badhwar-Konradi model with the SREM response functions across an energy range of 10 MeV to 500 MeV, angular countrates are obtained (Fig. 6).

The angular countrate demonstrates the interrelation between highly anisotropic flux and the resulting countrate characteristics. For a pitch angle of $\approx 84^\circ$ (so pointing nearly perpendicular to the field line), channel *TC1* detects particles predominantly through the main entrance ($\theta = 0^\circ$). For a pitch angle of $\approx 23^\circ$, the particle flux is spread between $\theta = 30^\circ$ and 140° , as suggested by Fig. 5. *TC1* shows response also in this region and therefore senses the flux. Channel *C3*, on the contrary, shows no response in this range of elevation angles and consequently reaches a countrate minimum at a pitch angle of $\approx 23^\circ$.

The general behaviour of countrates over time is illustrated in Figures 7 and 8. As supported by the measured data (Fig. 3), channels *S34*, *TC1* and *TC2* are only slightly affected of any pitch-angle induced flux anisotropies. Their countrates follow the omnidirectional AP8 model, and including anisotropic contributions does not greatly modify the results.

Channels *C1*, *C2* and *C3* have proved to be sensitive to flux anisotropies. The upper panel in figure 8 indicates clearly the discrepancy with the AP8 model. Only if an anisotropic scale

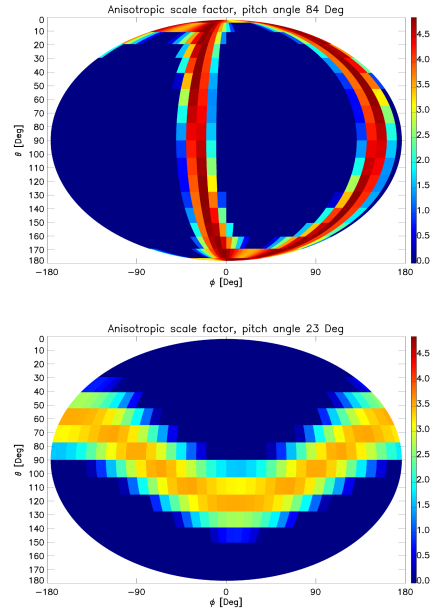


Figure 5. The anisotropic scale factor as given by the Badhwar-Konradi model for pitch angles of $\approx 84^\circ$ (upper panel) and $\approx 23^\circ$ (lower panel). The anisotropic scale factor is used to introduce anisotropy in the AP8-model. Both panels share the same colour mapping.

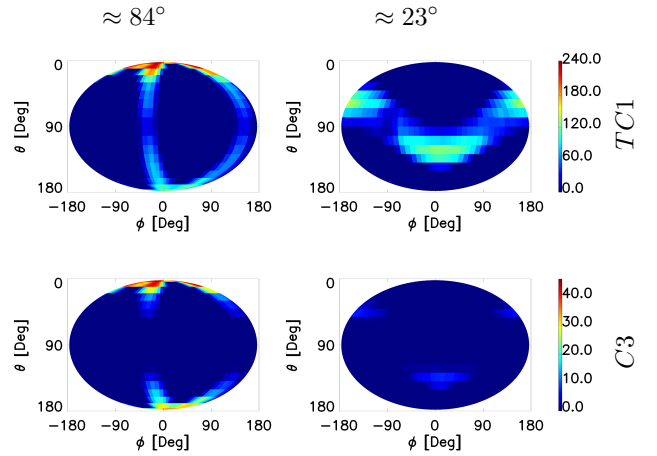


Figure 6. Angular countrate of channels *TC1* and *C3* at pitch angles of $\approx 84^\circ$ and $\approx 23^\circ$, colour-coded in $\frac{\#}{s}$. For $\approx 23^\circ$ (right panel), *TC1* still shows response while *C3* almost fades out.

factor as given by the Badhwar-Konradi model is introduced, can the measured profile in Fig. 3 be reproduced.

VI. LONG-TERM OBSERVATIONS

Short-term countrate characteristics have been shown in the previous section to be driven by flux anisotropies. An equivalent analysis for long-term countrates is possible using SREM data from PROBA-1 covering the period from 2001 to 2009. The L-binned countrate profile of PROBA-1 SREM is given in Figures 9 and 10. They show the inner Van Allen belt with a countrate maximum at $L \approx 1.3$ Earth radii. Comparisons to both AP8-MIN and AP8-MAX have been carried out. Even for long-term countrates, *C2* does

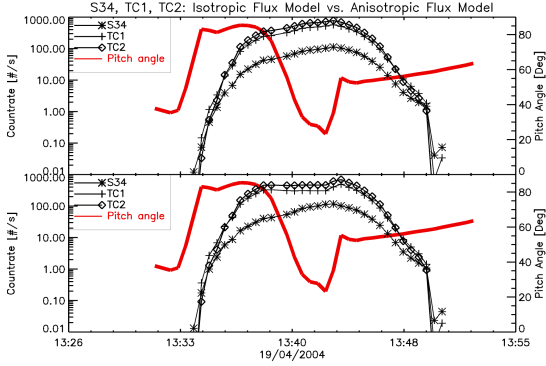


Figure 7. Simulated countrates of SREM channels $S34$, $TC1$, $TC2$ under a varying pitch angle. The reasonably omnidirectional nature of these channels renders them insensitive to pitch angle changes. Applying an isotropic flux model (upper panel, AP8-MIN) and an anisotropic flux model (lower panel, AP8-MIN/Badhwar-Konradi) yields similar countrate characteristics.

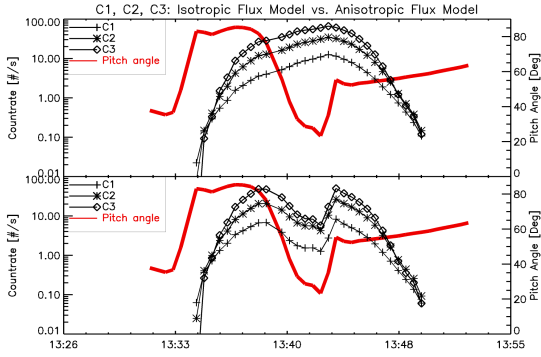


Figure 8. Simulated countrates of SREM channels $C3$, $C1$, $C2$ under a varying pitch angle. The channels have a highly directional response and are sensitive to pitch angle anisotropies. Applying an omnidirectional flux model (upper panel, AP8-MIN) does not reproduce the observed countrates. An anisotropic flux model (lower panel, AP8-MIN/Badhwar-Konradi) is required to match the measured characteristics shown in figure 3.

not show satisfactory agreement with omnidirectional AP8 models. Both AP8-MIN and AP8-MAX exceed the SREM data. The prediction can again be improved by combining AP8 with an anisotropic scale factor, as given by the Badhwar-Konradi model.

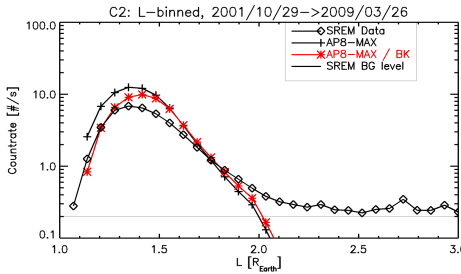


Figure 9. Countrate of PROBA/SREM channel $C2$ compared to AP8-MAX and AP8-MAX with a Badhwar-Konradi anisotropic scale factor.

In contrast to coincidence-channel $C2$, the AP8 model and SREM data show good agreement for the reasonably omnidirectional channel $TC2$ (figure 10). The adjustments due

to the Badhwar-Konradi model do not yield any difference.

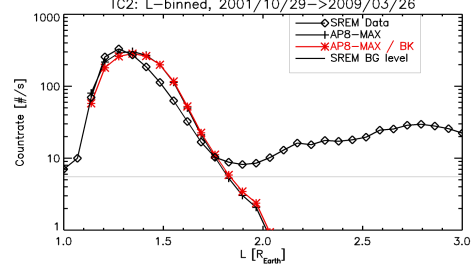


Figure 10. Countrate of PROBA/SREM channel $TC2$ compared to AP8-MAX and AP8-MAX with a Badhwar-Konradi anisotropic scale factor. Note: The $TC2$ channel is also sensitive to $> 2.8 \text{ MeV } e^-$, which is seen above $L = 2$.

VII. CONCLUSION

The SREM is a widely applicable instrument on ESA space missions and combines a versatile design with the capability of detecting spectral features and flux anisotropies. Both for short-term and long-term inner belt countrate data from PROBA-1, the SREM coincidence channels' countrates are sensitive to pitch angle flux anisotropies. Their countrates show good agreement with predictions if the Badhwar-Konradi model for pitch angle anisotropy is combined with the AP8 model.

Mapping SREM countrates from PROBA-1 as a function of pitch angle could therefore be used to further investigate inner-belt anisotropies. By adjusting the attitude of PROBA-1 accordingly, measurements of flux anisotropies due to the pitch angle effect should be possible. This work shows that it is important to consider anisotropies in comparing data with models. Furthermore, we are confident that SREM indicates an overprediction by AP8 between $L = 1.3$ and $L = 1.6$.

REFERENCES

- [1] A. Mohammadzadeh *et al.*, "The ESA Standard Radiation Environment Monitor program first results from PROBA-I and INTEGRAL," vol. 50, no. 6, pp. 2272–2277, Dec. 2003.
- [2] H. Evans, P. Buehler, W. Hajdas, and E. Daly, "Results from the ESA SREM monitors and comparison," *J. Adv. Space Res.*, 2008.
- [3] G. Santin, V. Ivanchenko, H. Evans, P. Nieminen, and E. Daly, "GRAS: a general-purpose 3-D Modular Simulation tool for space environment effects analysis," vol. 52, no. 6, pp. 2294–2299, Dec. 2005.
- [4] S. Agostinelli *et al.*, "Geant4 - a simulation toolkit," *Nuclear Instruments and Methods in Physics Research Section A: Accelerators, Spectrometers, Detectors and Associated Equipment*, vol. 506, no. 3, pp. 250 – 303, 2003. [Online]. Available: <http://www.sciencedirect.com/science/article/B6TJM-48TJFY8-5/2/23ea98096ce11c1be446850c04cfa498>
- [5] J. Allison *et al.*, "Geant4 developments and applications," *Nuclear Science, IEEE Transactions on*, vol. 53, no. 1, pp. 270–278, Feb. 2006.
- [6] J. VETTE, "The NASA/National Space Science Data Center trapped radiation environment model program, 1964–1991," N-93-11003, National Aeronautics and Space Administration, Greenbelt, MD (United States). Goddard Space Flight Center, Tech. Rep. 1991.
- [7] G. D. Badhwar and A. Konradi, "Conversion of omnidirectional proton fluxes into a pitch angle distribution," *J. Spacecraft Rockets*, vol. 27, 1990.
- [8] A. Lenck and S. Singer, "Effects of the finite gyroradii of geomagnetically trapped protons," *J. Geophys. Res.*, vol. 67, p. 4073, 1962.
- [9] H. Heckman and G. Nakano, "East-West Asymmetry in the Flux of Mirroring Geomagnetically Trapped Protons," *Journal of Geophysical Research*, vol. 68, pp. 2117–2120.

References

- [1] S. Agostinelli et al. Geant4 - a simulation toolkit. *Nuclear Instruments and Methods in Physics Research Section A: Accelerators, Spectrometers, Detectors and Associated Equipment*, 506(3):250 – 303, 2003. ISSN 0168-9002. doi: 10.1016/S0168-9002(03)01368-8. Available from: <http://www.sciencedirect.com/science/article/B6TJM-48TJFY8-5/2/23ea98096ce11c1be446850c04cfa498>. [Retrieved: 23 March 2009].
- [2] J. Allison et al. Geant4 developments and applications. *Nuclear Science, IEEE Transactions on*, 53(1):270–278, Feb. 2006. ISSN 0018-9499. doi: 10.1109/TNS.2006.869826.
- [3] G.D. Badhwar and A. Konradi. Conversion of omnidirectional proton fluxes into a pitch angle distribution. *J. Spacecraft Rockets*, 27, 1990.
- [4] Belgian Insititute for Space Aeronomy. SPENVIS - Space Environment, Effects, and Education System. Webpage. Available from: <http://www.spenvis.oma.be/>. [Retrieved: 19 March 2009].
- [5] M.J. Berger. ESTAR, PSTAR, and ASTAR: Computer programs for calculating stopping-power and range tables for electrons, protons, and helium ions. 1992.
- [6] D. Boscher, S. Bourdarie, P. O'Brien, and T. Guild. ONERA-DESP library V4.2, 2004-2008. Available from: http://craterre.onecert.fr/support/user_guide.html. [Retrieved: 13 June 2009].
- [7] P. Bühler. Methods for automated conversion of SREM countrates to particle fluxes. Technical report, 2007.
- [8] P. Bühler, W. Hajdas, and A. Zehnder. Technical note on WP 81. Technical report, Paul Scherrer Institute, 1998.
- [9] J.C. Cain. GSFC (12/66) model coefficients (1967). doi: 10.1016/0032-0633(92)90214-9.
- [10] CERN. *GDML User Manual*. Available from: <http://gdml.web.cern.ch/GDML/doc/GDMLmanual.pdf>. [Retrieved: 26 March, 2009]. Version 2.0.
- [11] CERN. Physics reference manual, 12 2008. Available from: <http://geant4.web.cern.ch/geant4/UserDocumentation/UsersGuides/PhysicsReferenceManual/fo/PhysicsReferenceManual.pdf>. [Retrieved: March 10, 2009].

References

- [12] R. Chytracek, J. McCormick, W. Pokorski, and G. Santin. Geometry Description Markup Language for Physics Simulation and Analysis Applications. 53(5):2892–2896, Oct. 2006. doi: 10.1109/TNS.2006.881062.
- [13] T. Ersmark et al. Geant4 Monte Carlo Simulations of the Belt Proton Radiation Environment On Board the International Space Station/Columbus. 54(4):1444–1453, Aug. 2007. doi: 10.1109/TNS.2007.896344.
- [14] European Cooperation for Space Standardization. ECSS-E-ST-10-04C: Space Engineering - Space Environment, 11 2008.
- [15] European Space Agency. ESA - Proba - Facts and figures. Webpage. Available from: http://www.esa.int/SPECIALS/Proba_web_site/ESA6AKTHN6D_0.html. [Retrieved: 25 April 2009].
- [16] H.D.R. Evans, P. Bühler, W. Hajdas, and E.J. Daly. Results from the ESA SREM monitors and comparison. *J. Adv. Space Res.*, 2008.
- [17] M. Hajek. Dosimetric Quantities. *Lecture notes on Space dosimetry*.
- [18] D. Hastings and H. Garrett. *Spacecraft-Environment Interactions (Cambridge Atmospheric and Space Science Series)*. Cambridge University Press, 8 2004. ISBN 9780521607568.
- [19] H. Heckman and G.H. Nakano. East-West Asymmetry in the Flux of Mirroring Geomagnetically Trapped Protons. *Journal of Geophysical Research*, 68:2117–2120.
- [20] W. Hess. *The Radiation Belt and Magnetosphere*. Blaisdell, 1968.
- [21] ITT Visual Information Solutions. IDL - Data Visualization Solutions. Webpage. Available from: <http://www.ittvis.com/ProductServices/IDL.aspx>. [Retrieved: 19 March 2009].
- [22] D.C. Jensen and J.C. Cain. An interim geomagnetic field. *J. Geophys. Res.*, 67(9):3568, 1962.
- [23] A.S. Johnson, M.J. Golightly, M.D. Weyland, T. Lin, and E.N. Zapp. Minimizing space radiation exposure during extra-vehicular activity. *Advances in Space Research*, 36(12):2524–2529, 2005.
- [24] G.F. Knoll. *Radiation Detection and Measurement*. Wiley, 3rd edition, 1 2000. ISBN 9780471073383.
- [25] M. Kruglanski and D. Heynderickx. Trend Technical Note 6. Technical report, 1998.
- [26] A.M. Lenchek and S.F. Singer. Effects of the finite gyroradii of geomagnetically trapped protons. *J. Geophys. Res.*, 67:4073, 1962.
- [27] R. McCuire. CDF Home Page, 06 2009. Available from: <http://cdf.gsfc.nasa.gov/>. [Retrieved: 19 June 2009].

References

- [28] A. Mohammadzadeh et al. The ESA Standard Radiation Environment Monitor program first results from PROBA-I and INTEGRAL. 50(6):2272–2277, Dec. 2003. doi: 10.1109/TNS.2003.821796.
- [29] NIST - National Institute of Standards and Technology. Stopping-Power and Range Tables for Electrons, Protons, and Helium Ions. Webpage. Available from: <http://physics.nist.gov/PhysRefData/Star/Text/contents.html>. [Retrieved: 13 May 2009].
- [30] W.P. Olson and K.A. Pfitzer. Magnetospheric magnetic field modeling, Annual Scientific Report, AFOSR Contract No. Technical report, F44620-75-C-0033, 1977.
- [31] J. Perl. HepRApp Users Home Page. Webpage. Available from: <http://www.slac.stanford.edu/BFR00T/www/Computing/Graphics/Wired/>. [Retrieved: 31 August 2009].
- [32] G. Santin, V. Ivanchenko, H. Evans, P. Nieminen, and E. Daly. GRAS: a general-purpose 3-D Modular Simulation tool for space environment effects analysis. 52(6): 2294–2299, Dec. 2005. doi: 10.1109/TNS.2005.860749.
- [33] S.M. Stone. *Investigation of the Magnetosphere of Ganymede with Galileo's Energetic Particle Detector*. PhD thesis. Available from: <http://galileo.ftecs.com/stone-diss/abstract.html>. [Retrieved: 8 March, 2009].
- [34] The ROOT Team. ROOT | A Data Analysis Framework. Webpage. Available from: <http://root.cern.ch/drupal/>. [Retrieved: 19 March 2009].
- [35] J. Vette. The NASA/National Space Science Data Center trapped radiation environment model program, 1964- 1991. Technical report, N-93-11003, National Aeronautics and Space Administration, Greenbelt, MD (United States). Goddard Space Flight Center, 1991.
- [36] P. Vuilleumeir. Standard Radiation Environment Monitor (SREM), Requirements Specification. *ESA/ESTEC internal report, SREM/RS/002*, 1997.